Search for the Single Production of Doubly-Charged Higgs Bosons at OPAL

Diplomarbeit
von
Marius Groll
aus
Hamburg

Institut für Experimentalphysik
Universität Hamburg
September 2003

Abstract

A search for the single production of doubly-charged Higgs bosons $H^{\pm\pm}$ decaying into two like-signed leptons is performed using 600.7 pb^{-1} of e^+e^- collision data collected by the OPAL experiment at LEP at centre-of-mass energies between 189 GeV and 209 GeV. Doubly-charged Higgs bosons arise in Higgs triplet models, which implement extensions in the Standard Model (SM) Higgs sector. Under certain circumstances the $H^{\pm\pm}$ could be also the lightest Higgs boson and it should be accessible for LEP energies. No evidence for the existence of $H^{\pm\pm}$ is observed. Upper limits are derived on h_{ee}, the Yukawa coupling of the $H^{\pm\pm}$ to like-signed electron pairs. A 95% confidence level upper limit of $h_{ee} < 0.071$ is inferred for $M(H^{\pm\pm}) < 160$ GeV assuming that the sum of the branching fractions of the $H^{\pm\pm}$ to all lepton flavour combinations is 100%.

Zusammenfassung

In dieser Arbeit werden Ergebnisse der Suche nach doppelt geladenen Higgs Bosonen $H^{\pm\pm}$ am OPAL Experiment am LEP Speicherring vorgestellt. Es wurden 600.7 pb^{-1} von e^+e^- Kollisionen bei Schwerpunktsenergien zwischen 189 GeV und 209 GeV ausgewertet. Erweiterungen des Standardmodells (SM) mit Higgs Triplets sagen doppelt geladene Higgs Bosonen $H^{\pm\pm}$ voraus. Das $H^{\pm\pm}$ zerfällt in zwei gleich geladene Leptonen und hat damit eine eindeutige experimentelle Zerfallssignatur. Unter bestimmten Voraussetzungen könnte das doppelt geladene Higgs Boson, das leichteste Higgs Boson sein, und könnte bei LEP Energien produziert werden. Es wurden keine Hinweise für die Existenz des $H^{\pm\pm}$ beobachtet. Obere Grenzen für die Yukawa Kopplung, h_{ee}, des $H^{\pm\pm}$ an gleich geladene Elektronpaare wurden abgeleitet. Eine obere Grenze $h_{ee} < 0.071$ wurde für Massen $M(H^{\pm\pm}) < 160$ GeV bei 95% Vertrauensniveau abgeleitet, unter der Annahme, daß das $H^{\pm\pm}$ ausschließlich in Leptonpaare zerfällt.

Contents

1 Introduction **4**

2 The Standard Model and Beyond **6**
2.1 The Status of the Standard Model 6
2.2 Higgs Mechanism 9
2.3 Problems of the SM 11
2.4 Higgs Triplet Models 11
2.4.1 Left-handed Higgs triplet Model 13
2.4.2 Left-Right Symmetric Models 14
2.5 Characteristics of doubly-charged Higgs Bosons 18
2.5.1 The Equivalent Photon Approximation 20
2.5.2 Decay of doubly-charged Higgs Bosons 20
2.6 Experimental Constraints 21
2.6.1 Indirect Search for the doubly-charged Higgs Boson 22

3 LEP and OPAL Detector **23**
3.1 The LEP Accelerator 23
3.2 The OPAL Detector 23
3.2.1 Central Tracking Detector 26
3.2.2 The Time-Of-Flight Detector 28
3.2.3 Electromagnetic Calorimeter 28
3.2.4 Hadronic Calorimeter 29
3.2.5 Muon Chambers 29
3.2.6 Forward Detector and Silicon-Tungsten Calorimeter 30

4 Signal and SM event Simulation **31**
4.1 The Signal Simulation 31
4.2 Comparison between COMPHEP and PYTHIA 32
4.3 Simulation of SM Processes 34
4.3.1 Physics Processes at LEP 34
4.3.2 Two-Photon Processes 35
4.3.3 Four-Fermion Processes 35
4.3.4 Two-Fermion Processes 36
4.3.5 Two-photon Production 37
4.4 The Detector Simulation 37

5 The Selection **42**
5.1 The Analysed Data Sample 42
5.2 The Generated Signal Samples 43
5.3 The Selection Criteria 44
5.3.1 The Pre-Selection 44
5.3.2 Main Selection 45
5.4 Systematic Uncertainties 53
5.4.1 Uncertainties due to the Modeling of Cut Variables 53
5.4.2 Uncertainties due to the Modeling of multi-peripheral "two-photon" Processes 54

6 Interpretation of Results **55**
6.1 Limit Calculation 55
6.1.1 Limit Calculation for a counting experiment 58
6.1.2 Combining Search Channels and Test Statistic 59
6.1.3 Exclusion Limit 61
6.1.4 Influence of Systematic Uncertainties 61
6.2 Exclusion Limits for the Yukawa Coupling h_{ee} 61

7 Summary **66**

A Angular and Energy Distribution Comparison between PYTHIA and COMPHEP **67**

B PYTHIA Comparison between Reconstruction with and without FSR **69**

Chapter 1

Introduction

Since the development of quantum physics at the beginning of the last century, the aim of particle physics was to describe the smallest constituents and their interactions of the world surrounding us. The best consistent theory up to now is the Standard Model (SM). The SM is a description of elementary particles and their interactions. These interactions are the strong, the weak and the electromagnetic force. The fourth interaction, gravitation, is, although it is the dominant force in our everyday life, neglected, because the masses of the constituents are too small.

A major part of the activities in high energy particle physics today concerns the question how the particles gain mass. Therefore, the investigations are concentrated on the signatures of the Higgs boson, which is responsible for electroweak symmetry breaking in the Glashow-Salam-Weinberg model [1], which is part of the Standard Model (SM). It is the only predicted Higgs boson in the SM and is still not observed. There is, however, a parallel stream of activities, going on to find out whether there is some new physics beyond the Standard Model. One aspect of this type of effort is to see the phenomenological implications of a larger scalar sector. This includes the possibility of models with two or more Higgs doublets. Also, scenarios with higher scalar representations of SU(2) are possible. Some of these representations predict the existence of Higgs triplets, including doubly-charged Higgs bosons, $H^{\pm\pm}$, in the physical particle content. These models are for example Higgs Triplet models [2] and Left-Right Symmetric models [3]. The advantage of triplet models is that triplet scalars can give a natural explanation of light left-handed Majorana masses for neutrinos via the see-saw mechanism [4]. The measurements in the solar and atmospheric neutrino fluxes seem to require that neutrinos indeed have a mass, manifested in these phenomena through flavour oscillations [5]. In the framework of the SM neutrinos have to be Dirac particles. However, it is also possible that neutrinos have Majorana character. As long as neutrinos are massless, it is not possible to distinguish between this two options. But if neutrinos have mass, then there exist differences between both possibilities. Therefore, it is reasonable to investigate extensions of the SM, in which neutrinos have in contrast to the SM Majorana character.

Besides the described advantage in the neutrino sector, another motivation for this analysis are some unexplained events, which have been seen by the H1 detector at HERA [6]. The observation consists of a few multi-electron events with a large di-electron mass, in a region, where the SM expectation is small.

A further motivation for this analysis is the fact, that in certain situations the doubly-charged Higgs bosons, $H^{\pm\pm}$, of Higgs triplets could be the lightest scalar in the Higgs sector

and under certain circumstances, they could be accessible for the LEP experiments. A search for the single production of doubly-charged Higgs bosons is therefore performed using e^+e^- collision data collected by the OPAL experiments at centre-of-mass energies between 189 GeV and 209 GeV.

After this short introduction the status of the SM is described in chapter two. Hence the theoretical motivation and scenarios, in which Higgs triplets occur are introduced. Finally the characteristics of the doubly-charged Higgs boson and how these non-standard signals could be observed are described.

In chapter three the experimental apparatus, which includes the LEP accelerator and the OPAL detector, are described.

In chapter four the simulation of possible doubly-charged Higgs processes and SM processes, which are important for this analysis, are described. This description includes also a comparison between two Monte Carlo generators (PYTHIA and COMPHEP) to check the expected theoretical cross-section for the investigated process.

The search for the single production of doubly-charged Higgs bosons is then described in chapter five. This chapter includes the description of the used cuts to separate events originating from doubly-charged Higgs production from SM events, the results and a discussion about the systematic uncertainties.

The interpretation of the results and the limit calculation for the Yukawa coupling h_{ee}, which is responsible for the doubly-charged Higgs boson production, is accomplished in chapter six.

A short summary is finally given in chapter seven.

Chapter 2

The Standard Model and Beyond

2.1 The Status of the Standard Model

The Standard Model (SM) is a description of elementary particles and their interactions. There are two different types of particles included. Fermions with spin 1/2 and gauge bosons with spin 1. The interactions between fermions are arranged by the gauge bosons (see table 2.1). Fermions are divided into two elementary categories: leptons and quarks. Quarks participate both in strong and electroweak interactions, whereas leptons are only subjected to electroweak interactions. The entire collection of the fermions is divided into generations. The first generation contains the up- and down-quark (u,d), electron (e) and electron-neutrino (ν_e). The second generation contains the charm- and the strange-quark (c,s), muon (μ) and the muon-neutrino (ν_μ). Finally the third generation consists of the bottom- and top-quark (b,t), tau (τ) and tau-neutrino (ν_τ). Every fermion has an anti-particle. Quarks and charged leptons of the second and third family are unstable and decay weakly into fermions of lower families.

Today the following interactions are known: the electromagnetic, weak, strong and gravitation. For the first three, gauge theories exist, but not for gravitation. However, gravitation is irrelevant for considerations at atomic level, due to the small treated particle masses and tiny coupling constant strength. Gravitation is therefore not a part of the SM. The SM arose from the Glashow-Weinberg-Salam model (GSW) [1] of the electroweak interaction. The SM is a gauge theory, which is based on the $\mathrm{SU(3)_C}\times\mathrm{SU(2)_L}\times\mathrm{U(1)_Y}$ symmetry. The $\mathrm{U(1)_Q}$ group of electromagnetism appears in the SM as a subgroup of $\mathrm{SU(2)_L}\times\mathrm{U(1)_Y}$. This subgroup represents the unification of the electromagnetic and the weak interaction. All charged particles are subjected to the Quantum Electrodynamics (QED). The gauge boson is the massless γ. The weak interaction affects, in constrast to the other interactions, all particles. The gauge bosons are the $W^\pm$ and Z^0. Its development is strongly associated with the discovery of the beta-decay. Strong interactions are described by a theory called Quantum Chromodynamics (QCD), which is invariant under the $\mathrm{SU(3)_C}$ gauge group. The strong interaction is responsible for the interaction of the quarks in hadrons. The particles carry the quantum numbers colour and the gauge bosons are eight gluons. The interactions are described in gauge theories, because gauge theories are in general renormalisable and therefore always lead to finite and physical results.

In the following the electroweak interaction including the Higgs mechanism is sum-

interaction	strength	boson	charge (e)	mass (GeV/c^2)
electromagnetic	1/137	γ	0	0
weak	10^{-5}	$W^{\pm}$	$\pm$ 1	80.2
		Z^0	0	91.2
strong	$\simeq 1$	8 gluons	0	0

Table 2.1: *Interactions between fermions with their strength and their gauge bosons.*

	Family					
	1	2	3	t_3	Y	Q
Leptons	$\begin{pmatrix} \nu_e \\ e \end{pmatrix}_L$	$\begin{pmatrix} \nu_\mu \\ \mu \end{pmatrix}_L$	$\begin{pmatrix} \nu_\tau \\ \tau \end{pmatrix}_L$	$1/2$	$-1/2$	0
				$-1/2$	$-1/2$	-1
	e_R	μ_R	τ_R	0	-1	-1
Quarks	$\begin{pmatrix} u \\ d' \end{pmatrix}_L$	$\begin{pmatrix} c \\ s' \end{pmatrix}_L$	$\begin{pmatrix} t \\ b' \end{pmatrix}_L$	$1/2$	$1/6$	$2/3$
				$-1/2$	$1/6$	$-1/3$
	u_R	c_R	t_R	0	$2/3$	$2/3$
	d'_R	s'_R	b'_R	0	$-1/3$	$-1/3$

Table 2.2: *Multiplet and quantum number assignments for the fermions in the Standard Model. The prime indicates that the weak eigenstates of the quarks are not their mass eigenstates. The quark mixing is described by the Cabibbo-Kobayashi-Maskawa (CKM) matrix. The indices L(R) denote left(right)-handed fermions.*

marised. The fundamental fermions are described as left-handed [1] doublets and as right-handed singlets in respect of the weak isopin $\vec{t}$. A list of all fermions and their properties are given in table 2.2. The isopin classification is introduced to describe parity violation in weak interactions. The parity operator P changes the moving direction of particles but not their spin. Therefore, it transforms left-handed particles into right-handed particles and vice versa. This is in agreement with all experimental results, which indicate that neutrinos are always left-handed, whereas anti-neutrinos are always right-handed. It is interesting to note that also the product of charge conjugation C and parity P is not conserved. Besides the isospin, the weak hypercharge Y is also defined:

$$Q = \frac{Y}{2} + t_3, \tag{2.1}$$

where t_3 is the third component of the isospin and Q is the electromagnetic charge.

Each fermion family consists of five different representations of the SM gauge group. There are left-handed charged leptons l^i_L and neutrinos ν^i_L, which are combined to isospin doublets for the i-th family. In the right-handed sector are only charged leptons l^i_R without neutrino partner. Therefore, in the right-handed sector exist only singlets and no doublets. The quarks are organised identically to the leptons. For example the left-handed up- and down-type quarks form a doublet of the $\mathrm{SU(2)_L}$ group with hypercharge +1/6. However, in comparison to the lepton-sector the quarks are also combined to a triplet under the $\mathrm{SU(3)_C}$ group of strong interactions, because quarks are in contrast to leptons also subjected to the strong interactions. The right-handed up- and down-type quarks and the right-handed

[1] For a massless left-handed fermion, the moving direction and the spin are antiparallel to each other. If the adjustment is parallel, then it is called right-handed.

charged leptons are singlets under the $SU(2)_L$ group. However, the right-handed up- and down-type quarks are also triplets under the $SU(3)_C$ group of strong interactions.

Note that the eigenstates of the down-type quarks in weak interaction d', s', b' are not identical to the mass eigenstates of d, s, b. These different eigenstates can be transformed into one another by the Kobayashi-Maskawa-Matrix V_{CKM}:

$$\begin{pmatrix} d' \\ s' \\ b' \end{pmatrix} = V_{CKM} \begin{pmatrix} d \\ s \\ b \end{pmatrix} = \begin{pmatrix} V_{ud} & V_{us} & V_{ub} \\ V_{cd} & V_{cs} & V_{cb} \\ V_{td} & V_{ts} & V_{tb} \end{pmatrix} \begin{pmatrix} d \\ s \\ b \end{pmatrix}. \tag{2.2}$$

The electromagnetic and the weak interactions are combined to one theory. The electroweak sector of the SM is based on the $SU(2)_L \times U(1)_Y$ gauge group generated by the hypercharge Y and the weak isospin $\vec{t}$. The Dirac equation has the following form:

$$(i\gamma_\mu \partial^\mu - m)\Psi = 0. \tag{2.3}$$

Here Ψ is a representation of the isopin-doublets and singlets, respectively. It should be invariant under local SU(2) transformations of the weak isospin. For leptons a transformation of this type can be written as:

$$\begin{pmatrix} \nu_e \\ e^- \end{pmatrix}'_L = \exp\left(i\frac{g}{2}\vec{\tau}\cdot\vec{\beta}(x)\right) \begin{pmatrix} \nu_e \\ e^- \end{pmatrix}_L. \tag{2.4}$$

The Dirac equation should be also invariant under U(1) transformation of the hypercharge Y. For leptons a transformation of this type has the following form:

$$\begin{pmatrix} \nu_e \\ e^- \end{pmatrix}'_L = \exp\left(i\Big(\frac{g'}{2}Y_L\Big)\chi(x)\right) \begin{pmatrix} \nu_e \\ e^- \end{pmatrix}_L, \tag{2.5}$$

$$e'_R = \exp\left(i\Big(\frac{g'}{2}Y_R\Big)\chi(x)\right) e_R. \tag{2.6}$$

To achieve invariance of these transformations, it is necessary that the particles are massless (m = 0) and the derivative ∂^μ has to be replaced with

$$\partial^\mu \rightarrow D^\mu = \partial^\mu + i\frac{g}{2}\vec{\tau}\cdot\vec{W}^\mu + i\frac{g'}{2}YB^\mu. \tag{2.7}$$

Hence there are four gauge fields $W^\mu_{1,2,3}$ and B^μ required. These fields couple with g respectively g' to fermions.

The weak interaction is mediated by the $W^\pm$ and Z^0 bosons. Charged currents are a result of $W^\pm$ bosons exchange. The Z^0 bosons are responsible for weak neutral current exchanges.

The Pauli matrices τ_i (i=1,2,3) are three linear independent generators of the SU(2) gauge group.

$$\tau_1 = \begin{pmatrix} 0 & 1 \\ 1 & 0 \end{pmatrix}, \qquad \tau_2 = \begin{pmatrix} 0 & -i \\ i & 0 \end{pmatrix}, \qquad \tau_3 = \begin{pmatrix} 1 & 0 \\ 0 & -1 \end{pmatrix}. \tag{2.8}$$

Two other operators are introduced to describe the fields of the $W^\pm$ bosons: τ^+ and τ^-.

$$\tau_+ = \frac{1}{2}(\tau_1 + i\tau_2) = \begin{pmatrix} 0 & 1 \\ 0 & 0 \end{pmatrix}, \qquad \tau_- = \frac{1}{2}(\tau_1 - i\tau_2) = \begin{pmatrix} 0 & 0 \\ 1 & 0 \end{pmatrix}. \tag{2.9}$$

Then it is possible to define a $\vec{\tau}$:

$$\vec{\tau} = (\sqrt{2}\ \tau^+, \tau_3, \sqrt{2}\ \tau^-). \tag{2.10}$$

The coupling of the W fields to left-handed leptons can then be written as:

$$\vec{\tau} \cdot W^\mu = \sqrt{2}\ (\tau_+ W^{(-)\mu} + \tau_- W^{(+)\mu}) + \tau_3 W_3^\mu. \tag{2.11}$$

Therefore, the fields of the $W^\pm$ bosons are:

$$W^{(\pm)\mu} = \frac{1}{\sqrt{2}}(W_1^\mu \pm i W_2^\mu). \tag{2.12}$$

Also the Z^0 and the photon field A can be written as composition of the two gauge fields:

$$Z^\mu = -B^\mu \sin\theta_W + W_3^\mu \cos\theta_W, \tag{2.13}$$
$$A^\mu = B^\mu \cos\theta_W + W_3^\mu \sin\theta_W, \tag{2.14}$$

where θ_W is the electroweak mixing angle.

2.2 Higgs Mechanism

The presence of fermion and boson mass terms in the SM Lagrangian would break the $\mathrm{SU(3)_C \times SU(2)_L \times U(1)_Y}$ symmetry. Thus, to preserve the gauge symmetry, one has to assume that all fermions and bosons are massless. But from experiment it is known, that only gluons, photons and in the SM also the neutrinos are massless. All other particles are massive. In the SM, the Higgs mechanism is used to describe the observation of massive particles. A spontaneous breaking in the $\mathrm{SU(2)_L \times U(1)_Y}$ symmetry is forced by introducing one complex scalar field with two components: one charged field ϕ^+ and one neutral field ϕ^0

$$\Phi = \frac{1}{\sqrt{2}} \begin{pmatrix} \phi_1^+ + i\phi_2^+ \\ \phi_1^0 + i\phi_2^0 \end{pmatrix}. \tag{2.15}$$

The Lagrangian of the Higgs field can divided into:

$$\mathcal{L} = T - V = (\partial_\mu \Phi)^\dagger (\partial^\mu \Phi) - V(\Phi^\dagger, \Phi), \tag{2.16}$$

where V is the potential:

$$V(\Phi^\dagger, \Phi) = -\frac{1}{2}\mu^2 \Phi^\dagger \Phi + \frac{1}{4}\lambda^2 (\Phi^\dagger \Phi)^2. \tag{2.17}$$

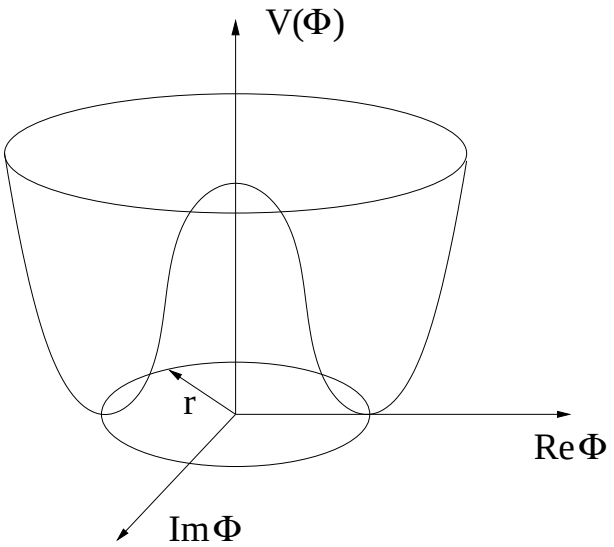

Figure 2.1: *The Higgs potential in the case of single complex scalar field (SM).*

For $\mu^2 > 0$ the potential looks like a mexican hat, which means that there is a continuous minimum (see figure 2.1). The minimum is described by a circle with radius r, which can be parametrised as $\Phi_0 = r \cdot \exp(i\alpha)$. The vacuum corresponds to a certain choice within this minimum, for example: $\alpha = 0$. The U(1) symmetry of the Higgs potential is not preserved for the chosen vacuum state. In other words, the vacuum state has a lower symmetry than the potential itself. This phenomenon is known in physics under the name of "Spontaneous Symmetry Breaking". The chosen vacuum expectation value of the Higgs field looks like:

$$< \Phi_0 >= \frac{1}{\sqrt{2}} \begin{pmatrix} 0 \\ v \end{pmatrix}, \qquad v = \frac{\mu}{\sqrt{\lambda}}. \tag{2.18}$$

This means that the ϕ^+ component of the Higgs field is zero, which is dictated by the necessity to ensure the conservation of the electromagnetic charge.

The Higgs particle is interpreted as a space-time dependent "radial" fluctuation h(x) of field Φ near the vacuum configuration:

$$\Phi = \frac{1}{\sqrt{2}} \begin{pmatrix} 0 \\ v + h(x) \end{pmatrix}. \tag{2.19}$$

The Lagrangian expressed in terms of the vacuum expectation value v and the physical state h,

$$\mathcal{L} = \frac{1}{2}\partial_\mu h \partial^\mu h - \lambda v^2 h^2 - \lambda v h^3 - \frac{\lambda}{4} h^4 \tag{2.20}$$

effectively describes the scalar particle with mass proportional to v:

$$m_h = \sqrt{2\lambda} v. \tag{2.21}$$

The scalar particle described by Lagrangian (see equation 2.20) is referred to the SM Higgs boson. The Higgs boson is the only ultimately remaining neutral physical state,

while the others manifest themselves as the longitudinally polarised components of the weak vector bosons. The Higgs boson decays primarily into either a pair of vector bosons or into a fermion-antifermion pair, depending on its mass. It is the only physical Higgs and the only particle not discovered so far in the SM. The Higgs boson is neutral and couples to fermions, proportional to their masses and to the massive gauge bosons. The terms proportional to h^3 and h^4 describe self-interaction of the field.

2.3 Problems of the SM

The overwhelming success of the SM with respect to the almost perfect agreement between predictions and measurements was proven many times. However, it is generally not believed that the SM is the ultimate theory. Although there are no questions, which are incorrectly answered within the SM concept so far, there are quite a few questions, which are not answered by the SM at all. Why are there three generations of leptons and quarks? Do leptons and quarks consist of smaller constituents? Why are the absolute values of the electron charge and the proton charge identical? Are the three interactions described by the SM three different appearances of a single one? How is it possible to include the gravity into the model?

Another interesting question is resulted from the measurements of the solar and atmospheric neutrino fluxes. These measurements seem to require that neutrinos indeed have a mass, justified in flavour oscillations [5]. In the framework of SM, however, it is possible to give neutrinos mass, but they have to remain Dirac particles. As long as neutrinos are massless, it is not possible to distinguish, whether they have Dirac or Majorana character. Dirac particles consist of four states (particle with spin up ν_L, particle with spin down ν_R, antiparticle with spin up $\bar{\nu}_L$ and antiparticle with spin down $\bar{\nu}_R$) with identical mass. In the framework of SM there are only left-handed neutrinos ν_L and right-handed anti-neutrinos $\bar{\nu}_R$ visible. However, neutrinos do not stand out among leptons and quarks only because of their extremely small masses, but also because of their charge neutrality. In the case of neutrinos the possibility exists that the neutrino is its own antiparticle since it is neutral. Such particles are called Majorana particles [2]. It is clear that Majorana particles only have two distinct states ν_R and ν_L. If neutrinos are Majorana particles then the lepton number is violated. If it is necessary to have a model, in which neutrinos gain mass and have Majorana character, extensions in the Higgs sector will be needed.

In this analysis, extensions of the SM are investigated, which introduce Higgs triplets. The advantage is that triplet scalars can give a natural explanation of light left-handed Majorana masses for neutrinos via the see-saw mechanism [4]. Within these extensions doubly-charged Higgs bosons are predicted. Therefore, the discovery of this particle would be a definite signal of physics beyond the Standard Model (SM). In the following sections these types of models are briefly described.

2.4 Higgs Triplet Models

The discovery of a doubly-charged Higgs boson would be a definite signal of physics beyond the Standard Model. Doubly-charged Higgs bosons arise in many extensions of

[2] Majorana proposed in 1937 [7] that a neutral fermion could have this property.

the SM. The SM describes the Higgs sector with a single $SU(2)_L$ doublet. A simple extension, which arises naturally in Supersymmetry, is to include two Higgs doublets. Beyond this, there are theories, which predict the existence of Higgs triplets, which have partly a doubly-charged Higgs boson included. In the context of the SM exists no specific motivation for the introduction of a Higgs triplet. But several models require a Higgs triplet for symmetry breaking. It is particularly interesting that, while all the charged fermions must get their masses via Yukawa couplings to Higgs doublets, the vacuum expectation values (vev) of triplets can give masses to neutrinos. Since the existence of non-zero neutrino masses is established, it might be useful to consider this possibility of a different origin of neutrino masses, which might help to understand why they are so small compared to those of the other fermions. The Lagrangian, which describes the triplet Yukawa coupling to lepton doublets is given by:

$$\mathcal{L}_Y = \sum_{K}^{N_{triplet}} \mathrm{h}_{K,ij} \Psi_{iK}^T C \tau_2 \Delta_K \Psi_{jK} + h.c., \tag{2.22}$$

where $N_{triplet}$ is the number of Higgs triplets included, i, j are flavour indices, C is the charge conjugation matrix, τ_2 is the second Pauli matrix, and Ψ_i denotes the left-handed lepton doublet with flavour i.

A problem, which arises with the introduction of Higgs triplet, is, that the vev of the neutral member of the triplet produces additional contributions to the parameter:

$$\rho = \frac{m_W^2}{m_Z^2 \cos^2 \theta_W}, \tag{2.23}$$

where θ_W is the Weinberg angle. The ρ parameter measures the effective strength of charged and neutral current couplings in $\nu(\bar{\nu})$ reactions. It is necessary to assign a very small vev to the neutral member of the left-handed triplet or to introduce a configuration, in which the contribution vanishes in order to avoid unacceptable corrections to the W-Z mass ratio. Since the present experimental value of ρ is $(1.0012 + 0.0023 - 0.0014)$ [8] and the value for the SM Higgs doublet excluding radiative corrections is close to unity, any scenario with scalar triplets has to be constrained accordingly. For a set of Higgs bosons with weak isospin t_i and whose neutral member is t_3 with vacuum expectation value λ_i, the ρ parameter looks like:

$$\rho = \frac{2 \sum_i t_{3_i}^2 |\lambda_i|^2}{\sum_i [t_i(t_i+1) - t_{3_i}^2] |\lambda_i|^2}. \tag{2.24}$$

If it is demanded that ρ is equal to one (apart from radiative corrections), the possible Higgs representations are restricted. This means that the values of t and t_3 have to obtain $\rho = 1$ independently of the value of λ_i. This leads to solving the following equation

$$3\ t_3^2 = t(t+1). \tag{2.25}$$

Obviously the usual solution is $(t,t_3) = (\frac{1}{2}, \pm\frac{1}{2})$. However, there are a lot of other solutions, e.g. (3,±2). This would lead to a 7-plet representation, which contains doubly and even higher charged Higgs bosons. It is interesting to note that the existence of all possible solutions of equation 2.25, even the 7-plet would all contain exotic Higgs bosons while not interfering the ρ parameter.

Obviously it is also possible to include the contribution of a Higgs triplet to the ρ parameter (see equation 2.24), additionally. As mentioned above, this scenario would have the advantage of producing Majorana masses naturally. However, there are a lot of possible scenarios for Higgs triplets. In the next sections just two examples are introduced: the Left-handed Higgs triplet model (LHTM) of Gelmini and Roncadelli [2] and the Left-Right Symmetric model (LRM) [3].

The Left-handed Higgs triplet model (LHTM) is the simplest extension. It is the known SM plus one Higgs triplet beside the normal Higgs doublet. The ρ parameter constraint is built in to postulate that the vev of the neutral member of the triplet is small enough so that its contribution to ρ is within the experimental limits. Another option is to make the assumption, first suggested by Georgi and Machacek [9] and by Chanowitz and Golden [10], that there is in fact more than one triplet in addition to the Y=1 complex doublet of the minimal Standard Model, arranged in such a manner, that their contributions to the ρ parameter cancel each other. One of the most attractive theories with such realisation of the Higgs sector is presented in the Left-Right Symmetric model (LRM) [3].

In the following sections the interesting aspects for this search of the Left-handed Higgs triplet model and of the Left-Right Symmetric model are briefly summarised.

2.4.1 Left-handed Higgs triplet Model

The Left-handed Higgs Triplet model (LHTM) contains at least one complex Higgs triplet with weak hypercharge $Y = 2$, which has lepton number violating couplings to leptons, but does not couple to quarks. This triplet Higgs field was first introduced by Gelmini and Roncadelli [2] in order to give rise to Majorana masses for left-handed neutrinos ν_L while preserving SU(2) gauge symmetry (ν_R is still absent). The LHTM contains a Higgs triplet field in addition to all SM matter particles and the usual Higgs doublet. The minimal Higgs multiplet content of the model is thus [11] [12]

$$\vec{\Delta} = \begin{pmatrix} \Delta^{++} \\ \Delta^{+} \\ \Delta^{0} \end{pmatrix}, \qquad \vec{\phi} = \begin{pmatrix} \phi^{+} \\ \phi^{0} \end{pmatrix}. \tag{2.26}$$

To get a 2×2 representation for the triplet, it is useful to apply the vector $\vec{\tau}$ (see equation 2.10) on the triplet (i.e. $\Delta \equiv \vec{\tau} \cdot \vec{\Delta}$):

$$\vec{\tau} \cdot \vec{\Delta} = \sqrt{2}\,(\tau_{+}\Delta^{++} + \tau_{-}\Delta^{0}) + \tau_{3}\Delta^{+}, \tag{2.27}$$

$$\Delta = \begin{pmatrix} \Delta^{+} & \sqrt{2}\,\Delta^{++} \\ \sqrt{2}\,\Delta^{0} & -\Delta^{+} \end{pmatrix}. \tag{2.28}$$

In this model the triplet has the weak isospin (1,±1) and contribute by the equation 2.24 to the ρ parameter. In this case ρ is not unity, but depends on the ratio of the triplet to doublet vacuum expectation values. Taking the vacuum expectation values to be $< \phi^0 >= v$ and $< \Delta^0 >= w$ the ρ parameter in this model is

$$\rho = \frac{1 + \frac{2w^2}{v^2}}{1 + \frac{4w^2}{v^2}}, \tag{2.29}$$

which is less than unity in the LHTM. As a result, the vev w of the triplet Higgs is constrained to be small compared with the vev v of the doublet. The current experimental constraints at 99% confidence level is:

$$\frac{w}{v} \leq 0.066. \tag{2.30}$$

It seems to be reasonable to set w to zero because of its smallness.

The physical scalar particle content of the model is composed of doubly-charged Higgs $\mathrm{H}^{\pm\pm}$, singly-charged Higgs $\mathrm{H}^{\pm}$, which are a mixture of the triplet and doublet components, and three neutral particles (two scalars H^0, h^0 and one pseudoscalar A^0).

The Higgs potential yields for $w \to 0$ the following approximate relation between the scalar masses:

$$M^2_{\mathrm{H}^{\pm\pm}} + M^2_A = 2 \cdot M^2_{H^{\pm}}, \tag{2.31}$$

where M_A is the pseudoscalar neutral mass. This relation implies, that masses of doubly and singly charged Higgs particles should not differ too much. This has implications regarding the decay modes of the $\mathrm{H}^{\pm\pm}$, which will be discussed in section 2.5.

The triplets Yukawa coupling to lepton doublets is given by

$$\mathcal{L}_Y = \mathrm{h}_{ij} \Psi_i^T C \tau_2 \Delta \Psi_j + h.c., \tag{2.32}$$

where i, j are flavour indices, C is the charge conjugation matrix and Ψ_i denotes the left-handed lepton doublet with flavour i. This interaction described by the Lagrangian of equation 2.32 provides Majorana masses for neutrinos:

$$m_{\nu_i} = \sqrt{2}\mathrm{h}_{ij} w. \tag{2.33}$$

Another solution is to add two triplet fields $\Delta_{L,R}$ (Y=2), which are described in Left-Right Symmetric models in the next section.

2.4.2 Left-Right Symmetric Models

The motivation to introduce Left-Right Symmetric models (LRM) is to suppose that observed parity nonconservation in weak interactions is only a low-energy phenomenon, which ought to disappear at high energies. This idea has been implemented in unified gauge theories of electroweak interactions based on the gauge group $\mathrm{SU(2)_L} \times \mathrm{SU(2)_R} \times \mathrm{U(1)_{B-L}}$, where parity nonconservation arises from the spontaneous breaking of the gauge symmetry of the LRM to the SM symmetry $\mathrm{SU(2)_L} \times \mathrm{U(1)_Y}$. The gauge group of LRM is therefore, more or less the SM gauge group plus its "reflection". Therefore, the gauge fields change and due to this, also heavier gauge bosons in the right-handed sector, besides the known $W^{\pm}$ and Z^0, are arised. These large masses of the right-handed gauge bosons lead to the suppression of the right-handed weak currents in this model. However, due to this symmetry breaking and the involved suppression of the right-handed weak interactions in Left-Right Symmetric models, the left-handed neutrinos are light Majorana particles [13], whereas the right-handed neutrinos are very heavy Majorana particles.

The basic structure of the gauge group $\mathrm{SU(2)_L} \times \mathrm{SU(2)_R} \times \mathrm{U(1)_{B-L}}$ is described in the following. Quarks and leptons are assigned to the doublets of the gauge groups $\mathrm{SU(2)_L}$ and $\mathrm{SU(2)_R}$ according to their chirality. The quantum numbers are (t_L,t_R,$B-L$), where

t_L is the left- and t_R the right-handed weak isospin and $B-L$ the difference between the numbers of baryons and leptons.

$$\psi_L = \begin{pmatrix} \nu_e \\ e^- \end{pmatrix}_L = (\frac{1}{2}, 0, -1), \qquad \psi_R = \begin{pmatrix} \nu_e \\ e^- \end{pmatrix}_R = (0, \frac{1}{2}, -1), \tag{2.34}$$

$$Q_L = \begin{pmatrix} u \\ d \end{pmatrix}_L = (\frac{1}{2}, 0, \frac{1}{3}), \qquad Q_R = \begin{pmatrix} u \\ d \end{pmatrix}_R = (0, \frac{1}{2}, \frac{1}{3}), \tag{2.35}$$

and similarly for the other families. There are two free gauge couplings in this model: $g_L \equiv g$ and g_R for the SU(2) groups and g' for the $\mathrm{U}(1)_{B-L}$ group. The electric charge formula for the model is

$$Q = t_{3L} + t_{3R} + \frac{B-L}{2}. \tag{2.36}$$

Left-Right Symmetric models contain two triplets $\Delta_{L,R}$ with hypercharge $Y = 2$ in addition to the $Y = 1$ complex doublet. This is one more triplet compared to the Left-handed Triplet model:

$$\Delta_{L,R} = \begin{pmatrix} \Delta^{++} \\ \Delta^{+} \\ \Delta^{0} \end{pmatrix}_{L,R}. \tag{2.37}$$

The fields exist in a left- and in a right-handed version and can be represented by:

$$\phi = \begin{pmatrix} \phi_1^0 & \phi_1^+ \\ \phi_2^- & \phi_2^0 \end{pmatrix} = \Big(\frac{1}{2}, \frac{1}{2}, 0\Big),$$

$$\Delta_L = \begin{pmatrix} \Delta_L^+ & \sqrt{2}\,\Delta_L^{++} \\ \sqrt{2}\,\Delta_L^0 & -\Delta_L^+ \end{pmatrix} = (1, 0, 2),$$

$$\Delta_R = \begin{pmatrix} \Delta_R^+ & \sqrt{2}\,\Delta_R^{++} \\ \sqrt{2}\,\Delta_R^0 & -\Delta_R^+ \end{pmatrix} = (0, 1, 2). \tag{2.38}$$

The numbers in the parenthesis refer again to left and right handed weak isospin respectively and to the value of $B-L$. The triplets are again written in a 2×2 representation (see equation 2.10).

All charged fermions obtain their masses through coupling to the doublet ϕ and its conjugate $\tilde{\phi}$. However, the neutrinos obtain their masses from coupling in a Majorana manner to Δ_L and Δ_R. The vacuum expectation values of the bidoublet Φ is given by

$$< \Phi_0 >= \frac{1}{\sqrt{2}} \begin{pmatrix} v_1 & 0 \\ 0 & v_2 \end{pmatrix}. \tag{2.39}$$

This breaks the SM symmetry $\mathrm{SU(2)_L} \times \mathrm{U(1)_Y}$. The vacuum expectation values of the scalar triplets are

$$< \Delta_{L,R} >= \frac{1}{\sqrt{2}} \begin{pmatrix} 0 & 0 \\ w_{L,R} & 0 \end{pmatrix}. \tag{2.40}$$

The right-triplet Δ_R breaks the $\mathrm{SU(2)_L} \times \mathrm{U(1)_{B-L}}$ symmetry to $\mathrm{U(1)_Y}$ and at the same time the discrete LR symmetry. It yields a Majorana mass to the right-handed neutrinos, as discussed before. Therefore, the following symmetry breaking pattern exits:

$$SU(2)_L \times SU(2)_R \times U(1) \rightarrow SU(2)_L \times U(1)_Y \rightarrow U(1)_{EM}. \tag{2.41}$$

It was also mentioned that the vacuum expectation value v_L of the left-handed triplet is quite tightly bound by the ρ parameter:

$$\rho = \frac{m_{W_1}^2}{m_{Z_1}^2 \cos^2\theta_W} \simeq \frac{1 + 2\frac{w_L^2}{v^2}}{1 + 4\frac{w_L^2}{v^2}}, \qquad v^2 = v_1^2 + v_2^2. \tag{2.42}$$

The experimental result implies $w_L \lesssim 9$ GeV, a small value compared with $v \simeq 246$ GeV. It was argued in [14] that in phenomenologically consistent models either w_L is exactly zero or a certain combination of the potential parameters should vanish. The discussion about w_L is similiar to the discussion about this parameter in section 2.4.1. It is, therefore, assumed that vev of Δ_L is negligible. This leads to the fact that the doubly-charged Higgs triplet components remain practically unmixed [15]. At the same time this assumption leads again to the relationship described in equation 2.31.

This left-right (LR) symmetry has to be also implemented on the Yukawa term

$$\mathcal{L}_Y = \mathrm{h}_{R,ij}\Psi_{iR}^T C\tau_2 \Delta_R \Psi_{jR} + \mathrm{h}_{L,ij}\Psi_{iL}^T C\tau_2 \Delta_L \Psi_{jL} + h.c., \qquad \Psi_i = \begin{pmatrix} \nu_{iR,L} \\ l_{iR,L} \end{pmatrix}, \tag{2.43}$$

where i, j are flavour indices, C is the charge conjugation matrix and Ψ_i denotes the left- and right-handed lepton doublet with flavour i. It is important to note that the $\mathrm{U(1)_{B-L}}$ symmetry prevents quarks from coupling to Δ_R and Δ_L. In the processes that involve hadrons the triplet Higgses appear, therefore, only through higher order corrections. This Yukawa Lagrangian leads to large Majorana mass terms of the form $\mathrm{h}_{R,ij}\langle\Delta_R^0\rangle\nu_{iR}\nu_{jR}$ for the right-handed neutrinos due to the symmetry breaking. This gives rise to the see-saw mechanism [16], which provides the simplest explanation to the lightness of ordinary left-handed neutrinos, if neutrinos have a mass. Along with the bidoublets Yukawa interactions, this leads to the usual quark 3×3 mass matrix and charged lepton masses, while for the neutrino, one obtains a see-saw mass matrix. Of most relevance is the constraint that left-handed neutrinos should have very small masses compared to other lepton masses. This restricts also the vev w_L of the neutral member of the Higgs triplet Δ_L to be small.

Altogether there exist 20 real degrees of freedom in the Higgs field (see equation 2.38). Of these, 6 unphysical Goldstone fields are absorbed in giving masses to the $W_1^\pm$, $W_2^\pm$, Z_1, Z_2. In terms of the vevs and the gauge couplings, the masses of the gauge bosons are given by

$$m^2_{W_1} \simeq \frac{1}{2}g^2(v_1^2+v_2^2+2w_L^2), \tag{2.44}$$

$$m^2_{W_2} \simeq \frac{1}{2}g^2(v_1^2+v_2^2+2w_R^2), \tag{2.45}$$

$$m^2_{Z_1} \simeq \frac{g^2}{2\cos^2\theta_W}(v_1^2+v_2^2+4w_L^2), \tag{2.46}$$

$$m^2_{Z_2} \simeq 2(g^2+g'^2)v_R^2, \tag{2.47}$$

where θ_W is the conventional Weinberg angle, and is related to the gauge couplings in a manner different than in the SM

$$\tan\theta_W = \frac{g'}{\sqrt{g^2+g'^2}}. \tag{2.48}$$

The bosons W_1 and W_2 are mixtures of W_L and W_R, which couple purely to left-handed and right-handed currents, respectively. The W_1 is the already discovered W and the W_2 must be heavier than the W_1. These theories also predict two neutral gauge bosons, Z_1 and Z_2, the lighter one is the familiar 91.2 GeV particle. The fermion sector contains the usual quarks and charged leptons, three light neutrino mass eigenstates, ν (i = 1,2,3), and three heavy neutrino mass eigenstates, N_i (i = 1,2,3). The former couple predominantly to W_1 while the latter couple mainly to W_2.

In the scalar Higgs sector are 4 doubly-charged, 4 singly-charged, and 6 neutral physical Higgs bosons left. They correspond to the quanta of the field

$$\begin{array}{l}
H_1^0 = \sqrt{2}\,(\ \ \cos\theta^0\ Re\phi_1^0 + \sin\theta^0\ Re\Delta_R^0) \\
H_2^0 = \sqrt{2}\,(-\sin\theta^0\ Re\phi_1^0 + \cos\theta^0\ Re\Delta_R^0) \\
h_1^0 = \sqrt{2}\ Re\Delta_L^0 \\
A_1^0 = \sqrt{2}\ Im\Delta_L^0 \\
h_2^0 = \sqrt{2}\ Re\phi_2^0 \\
A_2^0 = \sqrt{2}\ Im\phi_2^0
\end{array}
\qquad
\begin{array}{ll}
H_1^\pm = \phi_1^\pm + \frac{\kappa}{\sqrt{2}v_R}\Delta_R^\pm & H_R^{\pm\pm} = \Delta_R^{\pm\pm} \\
H_2^\pm = \Delta_L^\pm & H_L^{\pm\pm} = \Delta_L^{\pm\pm}.
\end{array}$$

The mixing angle θ^0 is given by linear combinations of the scalar bosons self-couplings of the Higgs potential.

The masses of the Higgs bosons depend both upon the symmetry breaking scales v and w_R and on the scalar self-couplings. The latter are rather arbitrary and, therefore, in general a prediction of the masses of the physical Higgs bosons are not possible.

In the last sections it was shown that the existence of both left and right handed Majorana neutrinos in the Left-Right Symmetric model demands the existence of at least two doubly-charged Higgs bosons. The Majorana coupling structure of the fermion to these Higgs naturally leads to lepton number violating processes. Apart from the question of neutrino mass, the LRM is more satisfactory than the SM, because it gives a better understanding of parity violation and it maintains the lepton-quark symmetry in weak interactions. So far there has been no direct evidence of left-right symmetry in weak interactions. This sets a lower boundary to the energy scale of the breaking of that symmetry. According to the direct searches of the CDF and D0 experiments at Tevatron, the intermediate bosons of the right-handed interactions have the mass limit $M_{W_R} \gtrsim 610\,\text{GeV}$ [17]. The mass limit for the new neutral intermediate boson is $M_{Z_R} \gtrsim 690\,\text{GeV}$ [18]. Although

there are some assumptions behind these boundaries concerning e.g. the strength g_R of the right-handed gauge interactions in comparison with the strength g_L of the left-handed interactions and the form of the CKM matrix of the right-handed interactions, which may degrade the boundaries considerably [19], it is reasonable to assume that below the scale of 0.5 TeV the left-right symmetry is broken. The phenomenological signatures of the LRM in 0.5 – 2 TeV linear collider have been under intensive study [20]. Particularly the signatures of the doubly-charged Higgs boson at e^+e^- linear collider are discussed in [21]. The production of a single doubly-charged Higgs in *ep* collisions at HERA was studied in [22]. It also turns out that under certain circumstances e.g. the doubly-charged Higgs boson is the lightest Higgs of the Higgs scalar sector, and so it would be accessible for LEP II [23]. This discussion is described in the next section.

2.5 Characteristics of doubly-charged Higgs Bosons

The interesting processes for this analysis have their origin in the Yukawa Lagrangian described in equation 2.32 or 2.43, which contain interactions between doubly-charged Higgs bosons and leptons. The strength of the interaction is scaled by the unknown Yukawa coupling constant h_{ij}, which, in general, is not flavour diagonal allowing for lepton number violating interactions. Due to left-right symmetry breaking the, LRM predicts two kinds of doubly-charged Higgs bosons with different interactions. Therefore, the two doubly-charged Higgs bosons $H^{\pm\pm}_{L,R}$ have different chiral couplings to leptons. Their masses are expected to be comparable with each other, because they are derived both from similar terms of the scalar potential. Since their production processes are the same, only the production of $H^{\pm\pm}_R$ is considered, in this search.

Doubly-charged Higgs bosons can be produced in e^+e^- collisions. Two alternatives are possible: The pair-production and the single-production of doubly-charged Higgs bosons. In the pair-production the final states resulting from $e^+e^- \to H^{++}H^{--}$ processes followed for example by $H^{\pm\pm} \to l^{\pm}l^{\pm}$ decays consist of four leptons. Due to the fact that doubly-charged Higgs bosons do not conserve baryon and lepton numbers, all lepton flavour decay modes are possible. This production channel is not part of this analysis. The pair production of doubly-charged Higgs bosons has been considered in a OPAL publication [24], where masses less than 98.5 GeV are excluded for doubly-charged Higgs bosons in Left-Right Symmetric models. The pair-production channel is obviously only sensitive to doubly-charged Higgs boson masses up to $\approx \frac{1}{2}\sqrt{s}$. In this analysis the single-production of doubly-charged Higgs bosons is investigated, which is sensitive up to $\approx \sqrt{s}$. The single-production of doubly-charged Higgs bosons in lepton colliders has been studied by several authors [21, 25, 26]. It has been noted that doubly-charged Higgs bosons may be singly produced in $e\gamma$ collisions.

$$e^-\gamma \to e^+H^{--} \tag{2.49}$$

The corresponding Feynman diagrams are shown in figure 2.2 including the decay of the $H^{\pm\pm}$ into like-signed lepton pairs.
The photon γ in e^+e^- collisions can be obtained from radiation from the other beam particle [20, 23].

$$e^+e^- \to e^+e^-\gamma \to e^+e^+H^{--} \tag{2.50}$$

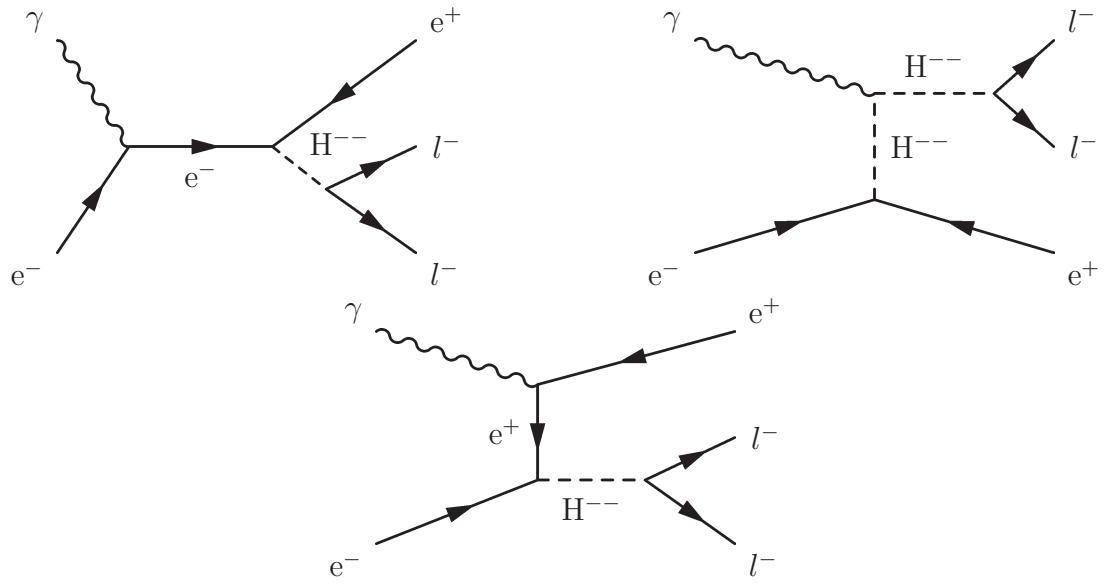

Figure 2.2: *Feynman diagrams contributing to the single production of* H^{--} *bosons in* $e\gamma$ *collisions. The three additional diagrams with "crossed"* e^+ *lines are not shown.*

The Feynman diagrams for the direct production are shown in figure 2.3.

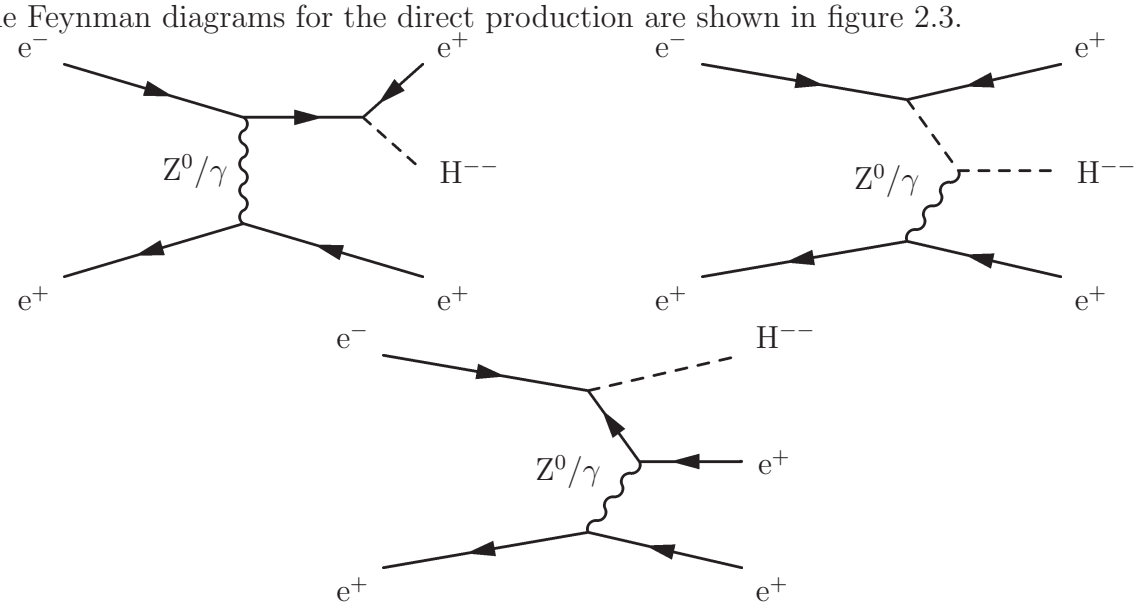

Figure 2.3: *Feynman diagrams contributing to the single production of* H^{--} *bosons in* e^+e^- *collisions. The three additional diagrams with "crossed"* e^+ *lines are not shown.*

Note that there are also crossed diagrams, if both of the final state leptons are electrons. In [20, 23] it was checked, that diagrams including neutral Higgs bosons are strongly suppressed due to the negligible couplings of Higgses to electrons and the large Higgs boson masses. It was also checked, that at LEP energies the diagrams mediated by Z bosons are suppressed compared with the graphs including photons and, therefore, can be neglected. Therefore, the process described in equation 2.49 can be regarded as the subprocess of the reaction described in equation 2.50.

A good estimation for the process described in equation 2.50 is to use the equivalent particle approximation (EPA) [27], which fairly reduces the complexity of the calculation. The calculation of the total cross section of the process described in equation 2.49 was

done in [28]. The interpretation for LEP and for the process described in equation 2.50 was done in [23].

2.5.1 The Equivalent Photon Approximation

The idea of the equivalent photon approximation (EPA) belongs to Fermi [29], who paid attention to the fact, that the field of a fast charged particle is similar to an electromagnetic radiation. This radiation may be interpreted as a flux of photons distributed with some density $n(\omega)$ on a frequency spectrum. Therefore, the electromagnetic interaction of this particle with another particle is reduced to the interaction of such photons with the other particle. Weizsäcker and Williams [27] followed Fermis idea and noted that the electromagnetic field of an electron in uniform relativistic motion are predominantly transverse, with $\vec{E} \approx \vec{B}$. When radiation occurs, the observed frequency spectrum will closely follow the virtual photon spectrum.

In e^+e^- collisions the lepton beams are intense sources of virtual photons. The spectrum of these photons is described by the EPA:

$$f_{\gamma/e}(x, Q^2) = \frac{\alpha}{2\pi Q^2}\Big[\frac{1+(1-x)^2}{x} - \frac{2m_e^2 x}{Q^2}\Big], \tag{2.51}$$

where x denotes the fraction of the electron energy carried by the photon and Q^2 is the negative squared four-momentum transfer, which is a quantity to describe the photon virtuality. To calculate the cross-section for the process $e^+e^- \to H^{\pm\pm}e^{\mp}e^{\mp}$, it is necessary to convolute the photon spectrum, $f_{\gamma/e}(x, Q^2)$, with the subprocess cross-section $\hat{\sigma}(e^{\pm}\gamma \to e^{\mp}H^{\pm\pm})$.

$$\sigma(e^+e^- \to H^{\pm\pm}e^{\mp}e^{\mp}) = \int\int dx\ dQ^2\ f_{\gamma/e}(x, Q^2)\ \hat{\sigma}(e^{\pm}\gamma \to e^{\mp}H^{\pm\pm}). \tag{2.52}$$

This calculation is described in detail in [28].

2.5.2 Decay of doubly-charged Higgs Bosons

In order to discover doubly-charged Higgs bosons at LEP, one has to detect its decay products. The decays of doubly-charged Higgs bosons have been studied in detail [30]. Doubly-charged Higgs bosons would decay into like-signed lepton pairs, vector boson pairs, into a W boson and a singly-charged Higgs boson or into a pair of singly-charged Higgs bosons. In this analysis, it is assumed, that the doubly-charged Higgs boson is the lightest Higgs boson. Accordingly, the decays into singly-charged Higgs bosons are negligible. For masses less than twice the W boson mass, they would decay predominantly into like-signed leptons. Furthermore, in most models the WW branching fraction is negligible even for larger masses [23], therefore, the dominant decay mode, even for masses larger than twice the W boson mass, is the decay to like-signed leptons. Since the $H^{\pm\pm}$ naturally violates lepton number conservation, it can have mixed lepton flavour decay modes. Additionally, the Yukawa coupling of the $H^{\pm\pm}$ to the charged leptons h_{ij} is model dependent. Generally it is not determined directly by the lepton mass, therefore, decays to all lepton flavour combinations need to be considered. It should be particularly noted that mixed lepton flavour decays are severely constrained by rare decay searches such as $\mu^+ \to e^+e^+e^-$ and $\mu \to e\gamma$ (see next section 2.6).

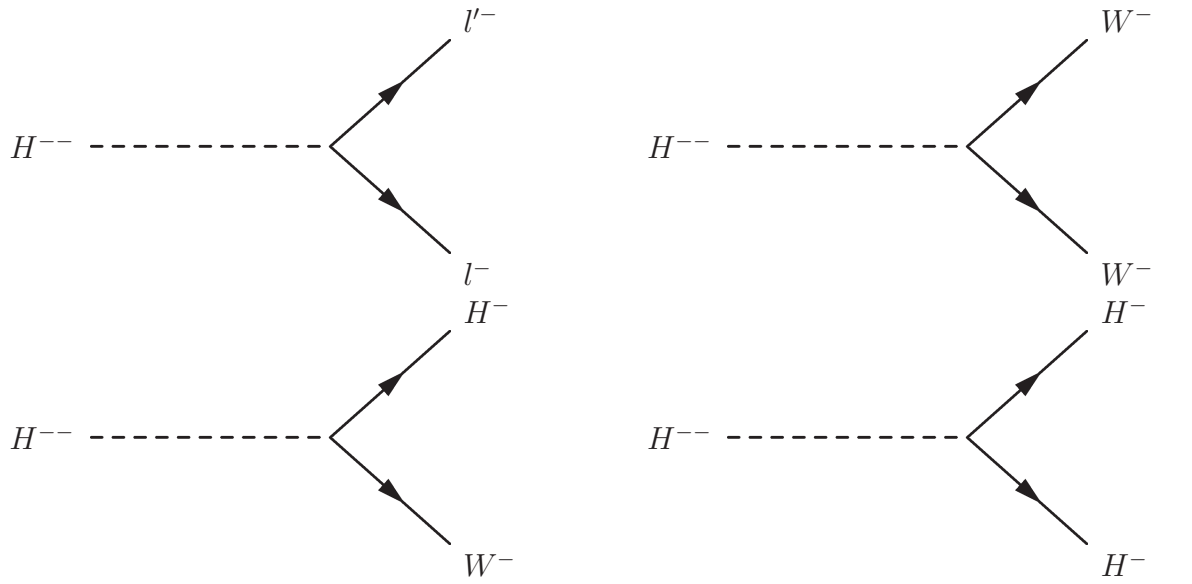

Figure 2.4: *Feynman diagrams for the possible decays of* H^{--} *bosons.*

2.6 Experimental Constraints

In the literature several experimental tests of lepton number violating interactions mediated by virtual doubly-charged bosons have been reported. There are two unknown parameters, on which the obtained constraints depend: the mass of the scalar $\mathrm{H}^{\pm\pm}$ and a coupling constant h_{ij}, where $i, j = \mathrm{e}, \mu$ (no constraints are available for the τ leptons). Assuming that the rest energy of the scalar is large compared with the interaction energy, the constraints one can derive from present measurements are upper limits of quantities of the type $\mathrm{h}_{ij}\mathrm{h}_{i'j'}/M^2_{\mathrm{H}^{\pm\pm}}$. The present experimental constraints are the following and are described in detail in [28, 31]. The most stringent constraint comes from the upper limit for the flavour changing decay $\mu \to \bar{\mathrm{e}}\mathrm{ee}$:

$$\mathrm{h}_{\mathrm{e}\mu}\mathrm{h}_{\mathrm{ee}} < 3.2 \cdot 10^{-11}\ \mathrm{GeV}^{-2} \cdot M^2_{\mathrm{H}^{--}}. \tag{2.53}$$

From non-observation of the decay $\mu \to \mathrm{e}\gamma$ follows the constraint

$$\mathrm{h}_{\mathrm{e}\mu}\mathrm{h}_{\mu\mu} \leq 2 \cdot 10^{-10}\ \mathrm{GeV}^{-2} \cdot M^2_{\mathrm{H}^{--}}. \tag{2.54}$$

From the Bhabha scattering cross-section at SLAC and DESY the following boundary on the h_{ee} coupling was established:

$$\mathrm{h}_{\mathrm{ee}}{}^2 \approx 9.7 \cdot 10^{-6}\ \mathrm{GeV}^{-2} \cdot M^2_{\mathrm{H}^{--}}. \tag{2.55}$$

For the coupling $\mathrm{h}_{\mu\mu}$ the extra contribution to $(\mathrm{g}\text{-}2)_\mu$ yields the limit

$$\mathrm{h}_{\mu\mu} \approx 2.5 \cdot 10^{-5}\ \mathrm{GeV}^{-2} \cdot M^2_{\mathrm{H}^{--}} \tag{2.56}$$

and the muonium transformation to antimuonium converts into a limit

$$\mathrm{h}_{\mathrm{ee}}\mathrm{h}_{\mu\mu} \approx 2 \cdot 10^{-7}\ \mathrm{GeV}^{-2} \cdot M^2_{\mathrm{H}^{--}}. \tag{2.57}$$

The pair production of doubly-charged Higgs bosons has been considered in a previous OPAL publication [24], where masses less than 98.5 GeV are excluded for doubly-charged

Higgs bosons in Left-Right Symmetric models. DELPHI has obtained a limit of 97.3 GeV, independent of the lifetime of the $H^{\pm\pm}$ [32].

2.6.1 Indirect Search for the doubly-charged Higgs Boson

A doubly-charged Higgs boson would also affect the Bhabha scattering cross-section via the t-channel exchange diagram shown in figure 2.5, causing a change in rate and in the observed angular distribution of the outgoing electron. Constraints have been derived for this process using data from lower energy colliders [31] and also from LEP [33].

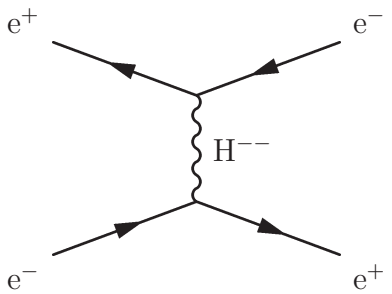

Figure 2.5: *Feynman diagram contributing to the process $e^+e^- \to e^+e^-$ due to doubly-charged Higgs boson t-channel exchange.*

In the OPAL analysis, indirect constraints on h_{ee}, the Yukawa coupling of $H^{\pm\pm}$ to electrons, using the differential cross-section of wide-angle Bhabha scattering measured by OPAL in 688.4 pb^{-1} of data collected at $\sqrt{s} = 183$–209 GeV are derived. The results together with the results of this direct search are shown in figure 6.6.

Chapter 3

LEP and OPAL Detector

3.1 The LEP Accelerator

The Large Electron Positron (LEP) Accelerator was built at the CERN laboratory close to Geneva, Switzerland. It was located in a tunnel at a depth of about 100 m and had a circumference of 26.7 km. Figure 3.1 shows a drawing of the accelerator arrangement. The accelerator and the four experiments ALEPH, DELPHI, L3 and OPAL were designed and built to study the electroweak interaction at energies up to 200 GeV. The first stage of LEP running (LEP I) started in 1989 with a centre-of-mass energy around 90 GeV to find and to investigate the Z-resonance. During the LEP II phase from 1996 to 2000 the centre-of-mass energy was continuously increased to a maximum of 209 GeV to investigate the properties of the W boson and to search for new phenomena. LEP was operated until 2000. The general principle of the LEP accelerator is described in the next paragraph following the order of figure 3.1.

Electrons produced by thermionic emission are accelerated to 200 MeV in the LEP Injector Linac (LIL) and directed onto a tungsten target to produce the positrons, the remaining electrons, along with the positrons, are then accelerated further to 600 MeV and passed into the Electron Positron Accumulator (EPA), where they are stored and accumulated before injection into the 200 m diameter Proton Synchrotron (PS). Here the particles are accelerated to a few GeV, before transfered into the 2.2 km circumference Super Proton Synchrotron (SPS), which accelerates the particles to 22 GeV. Finally, the particles are injected into the LEP accelerator in eight bunches (four electron and four positron), each of which contains about 10^{11} particles, and accelerated to a collision energy of up to about 209 GeV in the centre-of-mass frame. The energy and number of particles in a bunch is limited by the synchrotron radiation, causing an upper limit on both current and energy. The ring is designed with the maximum radius of curvature to minimise the energy loss through synchrotron radiation. The main loss of particles is through beam-gas interactions, so a high vacuum has to be maintained in the tunnel. This analysis uses data collected by the OPAL detector between 1998 and 2000.

3.2 The OPAL Detector

The OPAL (Omni Purpose Apparatus for LEP) detector was build to detect and identify all particles, except of neutrinos, produced in an electron-positron collision. It is a sym-

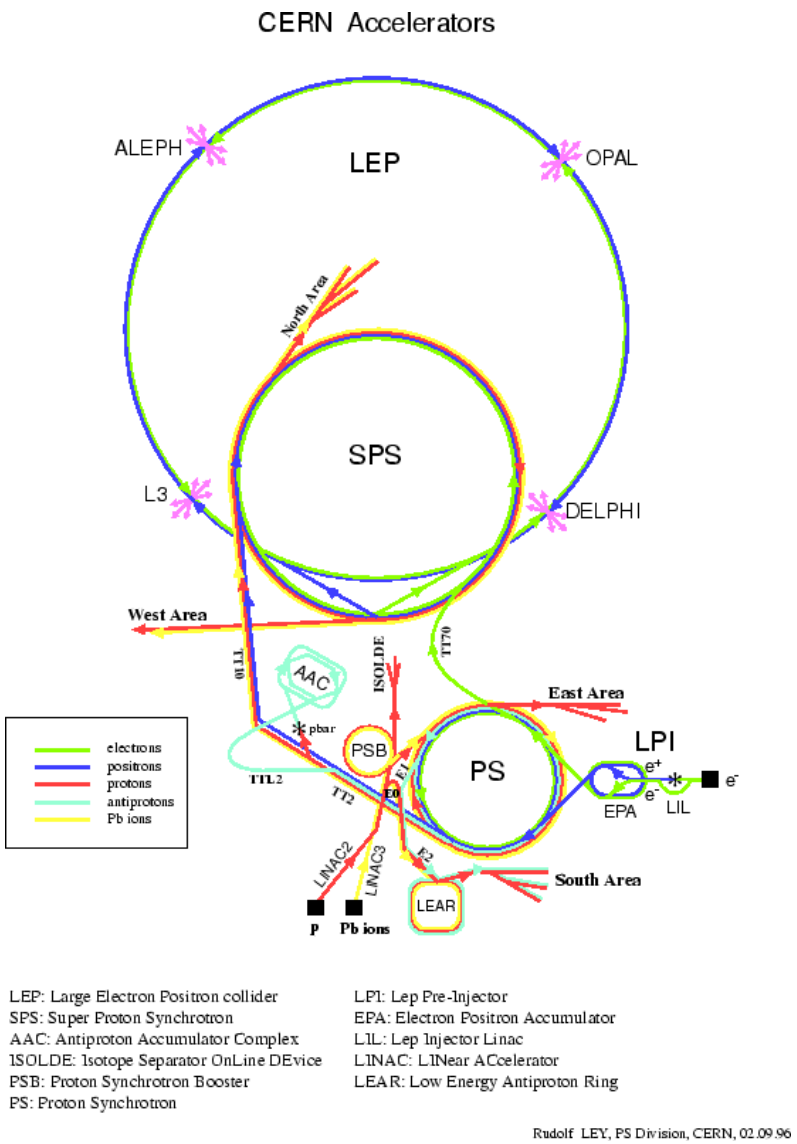

Figure 3.1: *The LEP collider layout and the four LEP experiments ALEPH, DELPHI, L3 and OPAL at CERN.*

metric barrel, multipurpose apparatus with almost complete solid angle coverage. It was designed to give good measurement of both particle momenta and energy and in some cases even particle species. The OPAL detector is 12 m long and has a diameter of 10 m. Its total weight is about 3000 t.

To describe positions within the OPAL detector the following coordinate system is used. The $+z$ component is determined by the direction of the electron beam, the origin is placed at the nominal interaction point. The $+x$ axis points to the centre of the circular LEP storage ring and the azimuthal angle ϕ is defined with respect to this axis. The polar angle θ is defined with respect to the $+z$ direction. The main features of the OPAL detector are shown in figures 3.2 and 3.3 and they can be described as follows:

- A central detector consists of vertex and tracking subdetectors, which are surrounded by a solenoid. The central detector provides measurements of the particles

direction and momentum and their identification by dE/dx as well as reconstruction of primary and secondary vertices at and near the interaction region. The solenoid causes bending of the charged particles in the tracking chamber.

- An electromagnetic calorimeter to provide identification of photons and electrons and to measure their energy.

- A hadronic calorimeter to measure hadronic energy. This is implemented by measuring the total absorption using instrumentation, which incorporates the magnetic yoke.

- A muon detector to identify muons by measurement of their position and direction within and behind the hadron calorimeter.

- A forward detector, situated in the very forward direction, and used to measure the received LEP luminosity at OPAL using Bhabha scattering events.

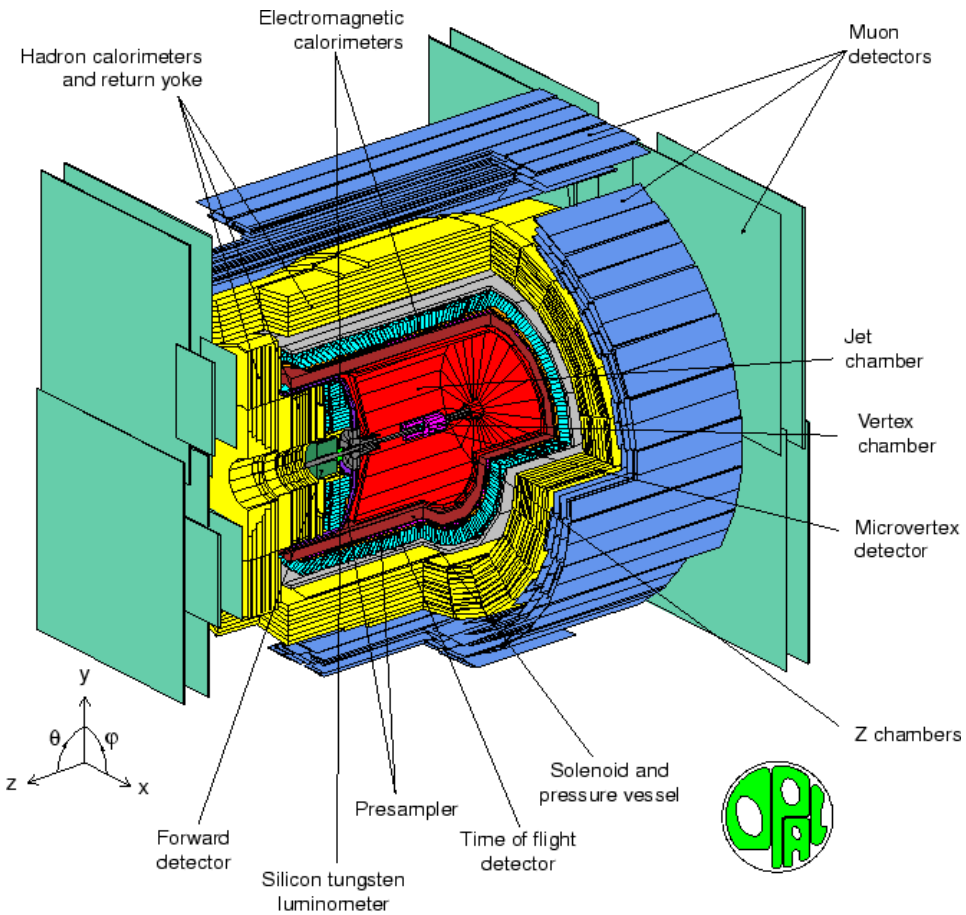

Figure 3.2: *A cut away diagram of the OPAL detector.*

In the following sections the detector parts are briefly described. The OPAL detector is described in more detail in [34].

3.2.1 Central Tracking Detector

The central detectors of OPAL are designed for tracking charged particles. The tracking system consists of two vertex detectors: the silicon microvertex detector (SI) and the central vertex detector (CV) and three tracking drift chambers: the vertex chamber (CV), the jet chamber (CJ) and the Z-chamber (CZ) in order of increasing radius. The latter three components are situated inside a pressure vessel holding a pressure of 4 bar. The whole central detector is surrounded by a solenoid, to cause charged particles to move in a helical path. The OPAL magnet consists of a water cooled solenoid and an iron yoke to provide flux return. The solenoid provides a field of 0.435 T within the central tracking region and is uniform to within 0.5 %. The configuration of the mentioned subdetectors is nicely noticeable in figure 3.3.

The tracks of charged particles in uniform magnetic fields are helices. At OPAL the following five track parameters are used for description:

- $|\kappa| = \frac{1}{2\rho}$: ρ is the curvature of the track projected in the r-ϕ plane.
- ϕ_0 : azimuthal angle of the track tangent at the point of closest approach (p.c.a.) to the origin in the r-ϕ plane.
- d_0 : the impact parameter is defined as the distance between p.c.a. and the origin.
- z_0 : the z coordinate at the p.c.a.
- $\cot\theta$: cotangent of the track polar angle.

Silicon Microvertex Subdetector

The SI is designed to give accurate measurement on the primary vertices of interaction between the electron and positron particles in the beam. It is also able to measure the positions of any secondary vertices resulting from the decays of particles that could have been produced in the primary interaction, such as τ-leptons and heavy flavour hadrons.

The SI consists of two cylinders of silicon ladders. The inner cylinder has a radius of 61 mm, consisting of 11 ladders and the outer has a radius of 75 mm, consisting of 14 ladders. Its polar angle coverage for tracks with hits is $|\cos\theta| < 0.89$. The azimuthal angle coverage for tracks with hits in each layer is 97 %. The impact parameter (d_0) resolution is measured to be 18 μm in the r-ϕ plane and 24 μm in the z direction.

Central Vertex Chamber

The CV is situated inside the central jet chamber and is a 1 m long and cylindrical high resolution drift chamber, which consists of two layers of 36 sectors each. It is designed to measure the vertex positions of decay particles and to improve the momentum resolution for charged particles.

The CV chamber, like all the central tracking drift chambers, is filled with 88.2 % argon, 9.8 % methane and 2.0 % isobutane at a pressure of 4 bar. When a charged particle passes through this chamber, it ionises the gas, which is then detected in the sense wires. The inner axial cells provide measurements in the $r-\phi$ plane with resolution of 50 μm. Combining information from the inner and outer cells gives a resolution of about 700 μm on the position in the z plane.

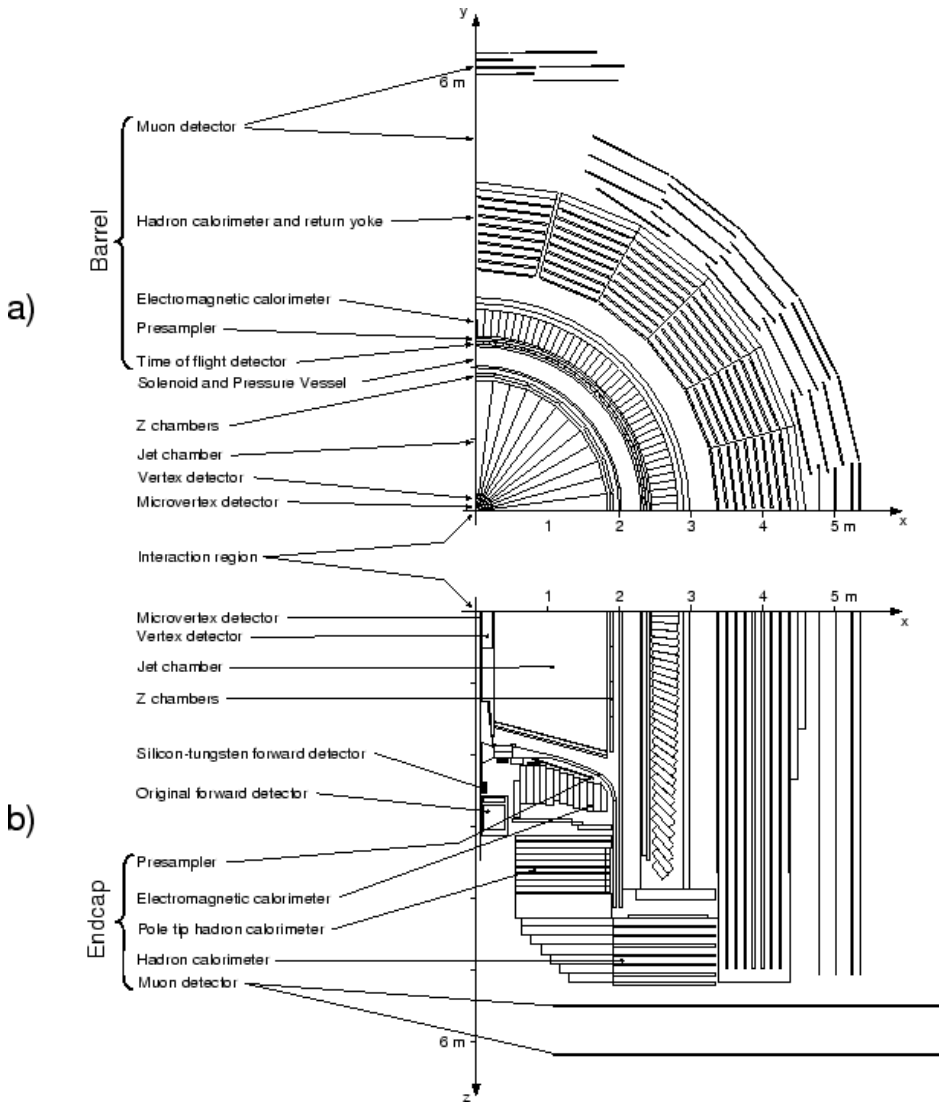

Figure 3.3: *A detailed schematic of the OPAL cross-section. On the upper part a) the detector is cutted away along the x-y plane and on the lower part b) the detector is cutted away along the x-z plane. In both cases it is just one quadrant shown, because of the detector symmetry.*

Central Jet Chamber

The CJ is designed to improve the measurement of the trajectory of the charged particles. It also has an important role in particle identification by measuring the specific energy loss, dE/dx. The first task is possible because tracks of charged particles are bent due to the magnetic field. The transversal momentum of a charged particle can be determined by measuring the curvature of its track.

The chamber is 4 m long, with an inner radius of 0.245 m and an outer radius of 1.85 m. The chamber contains anode sense wires to measure the tracks. In the polar angle range of $|cos\theta| < 0.73$, 159 points on the track are measured. For 98 % of the 4π solid angle at least 20 points are measured on every track.

Central Z Chamber

The CZ surrounds the CJ and makes precise measurements of the z position of a particle track as it leaves the CJ.

The CZ is divided into chambers and uses also sense wires for measurements. The CZ covers a polar angle range of $|\cos\theta| < 0.72$. Its resolution is 300 μm in z direction and 1.5 cm in the $r - \phi$ plane.

3.2.2 The Time-Of-Flight Detector

The time-of-flight detector (TOF) measures the transit time of particles traveling from the interaction region, which helps in charged particle identification. Its main task, however, is to aid in the rejection of cosmic ray events and generate trigger signals.

It is divided into two parts, the time-of-flight barrel (TB) and the tile endcaps (TE). The TB is situated at a radius of 2.36 m, surrounding the solenoid. It is made up of 160 scintillation counters, which cover solid angle range of $|\cos\theta| < 0.82$. The time resolution of TB is approximately 300 ps and the difference in time between the signal arriving at each end of the counter is used to make a z position measurement. The TE perform the same function in the endcap region as TB does in the barrel region. TE consists of 10 mm thick scintillating plastic tiles. It has a timing precision of about 3 ns and covers the region close to the beam pipe.

3.2.3 Electromagnetic Calorimeter

The electromagnetic calorimeter (ECAL) is designed to give the most precise and important measurement of particles energies. It can measure energies between a few tens of MeV up to 100 GeV. It measures the energies and positions of electrons, positrons and photons, and helps to discriminate between electrons and hadrons.

The ECAL is divided into a barrel region and two endcap regions and gives a coverage of 98 % of the solid angle. Each region consists of a presampler in front of a lead-glass calorimeter.

Electromagnetic Presamplers

Most electromagnetic showers are initiated before reaching ECAL as there are approximately two radiation lengths between the interaction region and the calorimeter. This is the reason to incorporate a presampler into the ECAL. The presamplers are used to measure the charged multiplicity of clusters before they enter the electromagnetic calorimeter and, therefore, they help in energy resolution of the shower and discrimination between particles.

The barrel presampler (PB) is a 6.623 m long cylinder of radius 2.388 m situated between the time-of-flight barrel and the barrel electromagnetic calorimeter. The barrel presampler covers a polar angle range of $|\cos\theta| < 0.81$. The two endcap presamplers (PE) are situated between the time-of-flight endcap (TE) and the endcap electromagnetic calorimeters, and gives full azimuthal angle coverage and a polar angle coverage of $0.86 < |\cos\theta| < 0.95$.

Electromagnetic Calorimeters

The electromagnetic calorimeter is separated into three sections, a barrel section (EB) and two endcap regions (EE). The EB is a cylindrical array of 9440 lead-glass blocks. Each block is 37 cm deep, which is 24.6 radiation lengths, has an approximate surface area of 10 × 10 cm, and are situated at a radius of 2.455 m from the interaction point.

The subdetector works on the principle that relativistic particles traveling through the blocks will emit Čerenkov radiation, which can be collected by photomultiplyer tubes at the end of the blocks. The thickness of the lead-glass blocks ensures that electrons, positrons and photons deposit almost all of their energy in the electromagnetic calorimeter. The light output is proportional to the deposited energy. The EB covers a polar angle range of $|\cos\theta| < 0.82$ and has a spatial resolution for a particle of 6 GeV, of approximately 11 mm. The EEs cover a polar angle range of $0.83 < |\cos\theta| < 0.95$. Each of the two EEs consists of 1132 lead-glass scintillator blocks. Particles traversing the blocks are presented with a minimum of 20.5 radiation lengths. The energy resolution is approximately 1 % in the energy region 3-50 GeV.

3.2.4 Hadronic Calorimeter

The hadronic calorimeter (HCAL), like the electromagnetic calorimeter, has a barrel region (HB) and two endcap regions (HE) covering roughly the same regions as the ECAL, however, HCAL also has a hadron poletip calorimeter, which covers regions were the momentum resolution of the central detectors is poor. HCAL uses the iron return yoke of the OPAL magnet as passive absorbing material. Layers of the iron are sandwiched by planes of detectors. Due to the large amount of material between HCAL and the interaction point, most hadronic showers are likely to have initiated long before reaching HCAL, this means, that the hadronic energy measurement is made by adding the energy deposited in HCAL with that deposited in ECAL. Together with the electromagnetic calorimeter provides a thickness of more than seven hadronic radiation length. Therefore, almost all hadronic energy of an event is deposited in the calorimeter. The detectors consist of limited streamer mode tubes with wires parallel to the beam axis. The tubes are filled with 75 % isobutane and 25 % argon. The energy resolution is approximately $120\%/\sqrt{\frac{E}{GeV}}$.

3.2.5 Muon Chambers

The muon chambers are also split into a barrel region and an endcap region. They give coverage of 93% of the solid angle, and are designed to detect muons. Muons are highly penetrating and will pass through the ECAL and HCAL. Hadrons also usually pass through ECAL, but almost never through HCAL to reach the muon chambers. The probability of a pion reaching the muon chambers is less than 0.1 %, so misidentification within the muon chambers is highly unlikely.

The Muon Barrel (MB) consists of 110 drift chambers arranged so that there are 44 chambers on either side of the OPAL detector, twelve chambers below and ten above. The polar angle coverage goes up to $|\cos\theta| < 0.72$. The chambers are filled with 90 % argon and 10 % ethane. They have a z position resolution of 2 mm and a ϕ-position resolution of 1.5 mm.

The Muon Endcaps (ME) are also divided into chambers and cover a polar range of about $0.67 < |\cos\theta| < 0.985$ either side of the detector. The chambers are filled with 75 % argon and 25 % isobutane. The spatial resolution is ~ 2 mm.

3.2.6 Forward Detector and Silicon-Tungsten Calorimeter

It is important to know the precise luminosity to calculate the expected event rates for a certain process. At OPAL the luminosity is measured by the theoretically well understood process of Bhabha scattering under small angles. To detect Bhabha scattering the forward detectors (FD) are designed.

The FD are situated at either end of the detector to measure very low angle particles. The FDs are in fact made up of four separate subdetectors; the main calorimeter (FK), the forward tube chambers (FB), the γ-catcher (FE) and the far forward luminosity monitor (FF).

The silicon-tungsten calorimeters (SW) are situated either side of OPAL at 2.389 m in the z direction from the interaction point. They were installed in 1993 to give an improvement on the luminosity measurement by detecting Bhabha electrons emitted under polar angles between 25 and 59 mrad.

Chapter 4

Signal and SM event Simulation

Physicists use accelerators and detectors to gain experimental data. The interpretation of these data requires a comparison with theoretical predictions. These theoretical inputs are calculated in computer simulations of e^+e^- collisions followed by simulations of the detector components and their response to the generated events. The simulation of the signal process and all possible SM processes (background) are needed for the specification of signal selection criteria. Signal properties are used as filter criteria aiming for both a high signal purity and large signal detection efficiency. The signal detection or a possible discovery is then based on the comparison of the number of expected (simulated) background events and the number of candidates selected in the data sample. Typically, specialised generators are used for a class of background and signal processes. In case of quarks in the final state, these have to be passed through an additional program simulating the fragmentation process. The event generation finishes with a list of four-vectors of all final state particles. The complete event simulation contains two steps, namely the event generation and the detector simulation. In the following sections, the signal and SM background simulations are described.

4.1 The Signal Simulation

Following the discussion in section 2.5 it is assumed that the decay of a doubly-charged Higgs boson into a W boson and a singly-charged Higgs boson is negligible. It is an $H^{\pm\pm}$, which couples to right-handed particles considered. However, the results of this search are also valid for an $H^{\pm\pm}$, which couples only to left-handed particles [23]. All lepton flavour combinations are considered in the $H^{\pm\pm}$ decay (ee, $\mu\mu$, $\tau\tau$, eμ, eτ, $\mu\tau$). The lifetime of the $H^{\pm\pm}$ can be important, and in particular is non-negligible for $h_{ij} < 10^{-7}$, because in this case the decay of the $H^{\pm\pm}$ takes place outside of the detector and so the decay products are not in the detector. However, this search is not sensitive to such small Yukawa couplings.

The process $e^+e^- \rightarrow e^\mp e^\mp H^{\pm\pm}$ is simulated with the PYTHIA6.150 [36] event generator. In the simulation, the Equivalent Photon Approximation (EPA) is used to give an effective flux of photons originating from the electrons or positrons. The upper limit of the virtuality Q^2 of the photon is given by the scale of the hard scattering process [1]. This subprocess $e^\pm\gamma \rightarrow e^\mp H^{\pm\pm}$ is simulated in a Left-Right Symmetric model for an $H^{\pm\pm}$,

[1] Q^2 is the negative squared four-momentum transfer.

which couples to right-handed particles using the calculations from [20]. Due to this calculation the contribution from Z-exchange is negligible for LEP and even higher energies, because of the high mass of the Z boson.

4.2 Comparison between COMPHEP and PYTHIA

The doubly-charged Higgs is obviously not a SM particle. Therefore, there are different approaches to get its production cross-section. This question is investigated by comparison between two different event generators, PYTHIA and COMPHEP. Both event generators perform their calculation on tree-level. The event generator PYTHIA uses calculations for parametrisation of the phase space from [20]. PYTHIA is not able to simulate the complete four fermion process $e^+e^- \rightarrow e^\mp e^\mp H^{\pm\pm} \rightarrow e^\mp e^\mp \ell^\pm \ell'^\pm$, however, it uses the Equivalent Photon Approximation (EPA) to give an effective flux of photons originating from the electrons or positrons. Therefore, PYTHIA simulates this process using the subprocess $e^\pm\gamma \rightarrow e^\mp H^{\pm\pm}$ in a Left-Right Symmetric model for an $H^{\pm\pm}$, which couples to right-handed particles. Furthermore the group of Stephen Godfrey, Pat Kalyniak and Nikolai Romanenko integrate a Left-Right Symmetric model in another event generator called COMPHEP [37]. In COMPHEP it is possible to use the four fermion process $e^+e^- \rightarrow e^\mp e^\mp H^{\pm\pm} \rightarrow e^\mp e^\mp \ell^\pm \ell'^\pm$ as input. But COMPHEP is also not able to simulate this process over the full phase space. COMPHEP does not apply any phase space cut by default and it also have the option to switch the EPA on. Therefore, one possibility is to implement cuts on the angular distribution of the outgoing particles or to use also the EPA. The calculation of [23] uses this approximation.

Due to this difference the cross-section and the simulated four-vectors are checked. It turns out, that the calculated cross-section of PYTHIA is significantly lower than the ones calculated with COMPHEP. This is shown in figure 4.1, where a doubly-charged Higgs boson of 130 GeV in e^+e^- collisions by centre-of-mass energy of 200 GeV is assumed.

In order to obtain the full signal cross-section, a cut, which PYTHIA applies by default at a minimum of 1 GeV on the transverse momentum of the lepton, which radiates the $H^{\pm\pm}$ is explicitly switched off. The cross-section and the angular distribution after this modification are checked and are shown in figures 4.2 and A.1. For comparison the process $e^+e^- \rightarrow e^+e^+H^{--} \rightarrow e^+e^+\mu^-\mu^-$ is simulated using the subprocess $e\gamma \rightarrow e^+H^{--} \rightarrow e^+\mu^-\mu^-$. The results for a doubly-charged Higgs boson of 130 GeV in e^+e^- collisions by centre-of-mass energy of 200 GeV are shown. In figure A.1 the angular distributions between the produced final state particles and the beamline and their energies are shown.

In PYTHIA final state radiation is implemented, therefore, the final state γs have to be considered in the reconstruction of the doubly-charged Higgs boson. The angular and energy distribution of the reconstructed doubly-charged Higgs boson with and without consideration of the final state γs are shown in figure B.1.

The conclusion for the event simulation for this analysis is to use the modified PYTHIA event generator, because it produces the same results in the cross-section calculation and in the angular distribution compared with COMPHEP and it is easier to integrate in the analysis chain.

The comparison between the standard PYTHIA event generator and the modified one for our analysis reveals that the gain in cross-section is mainly due to the increase of

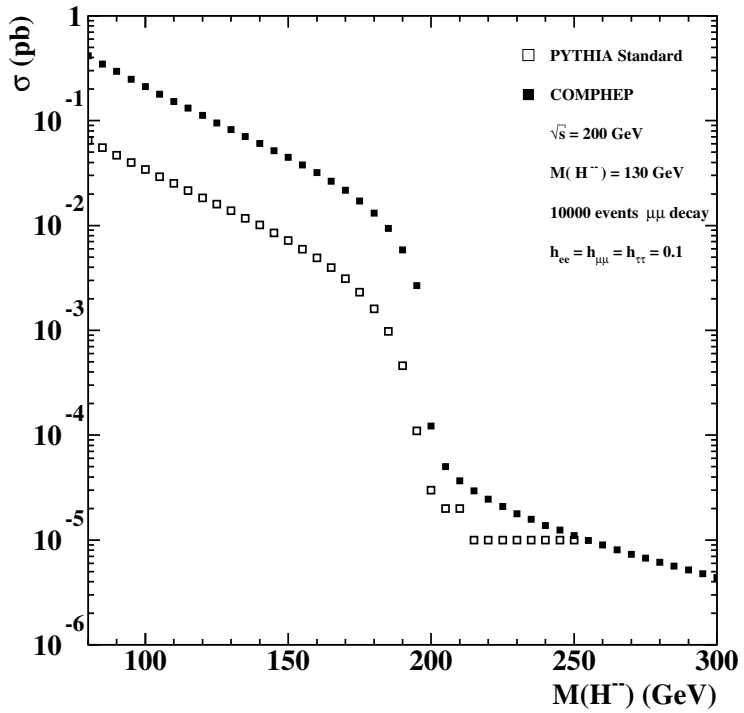

Figure 4.1: *Comparison of the calculated cross-sections of 'standard' PYTHIA and COMPHEP. Note that the linear behaviour of the PYTHIA curve at high masses is due to the lack of accuracy in the cross-section calculation.*

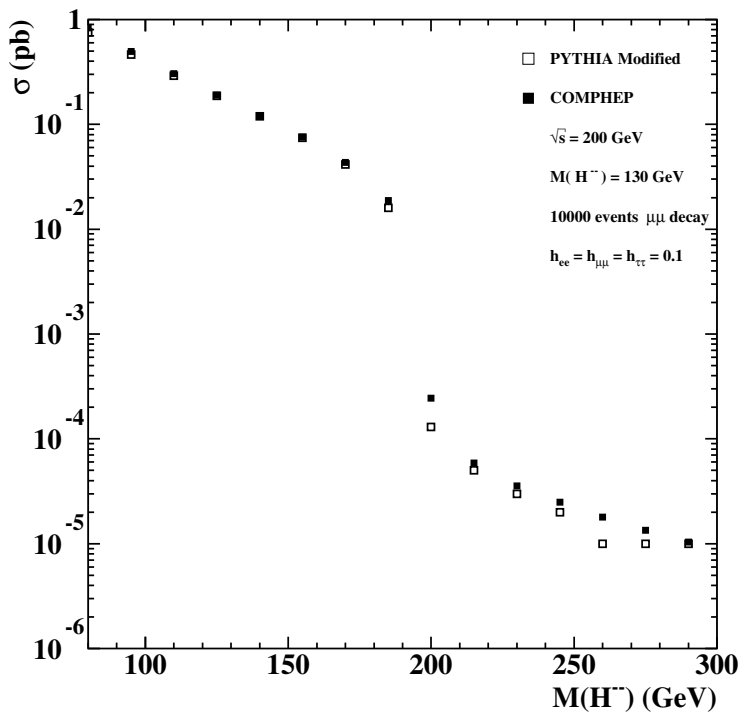

Figure 4.2: *Comparison of the calculated cross-sections of 'modified' PYTHIA and COMPHEP.*

events with only two leptons in the final state (see figure 4.3). These could be the two leptons from the Higgs decay. The third lepton is from the Higgs vertex and the fourth lepton from the EPA photon is normally lost in the beamline. The third lepton has in most of the cases a low transverse momentum P_{xy}. Therefore, the standard PYTHIA removes a large part of the cross-section, due to the standard minimum cut of 1 GeV on this quantity.

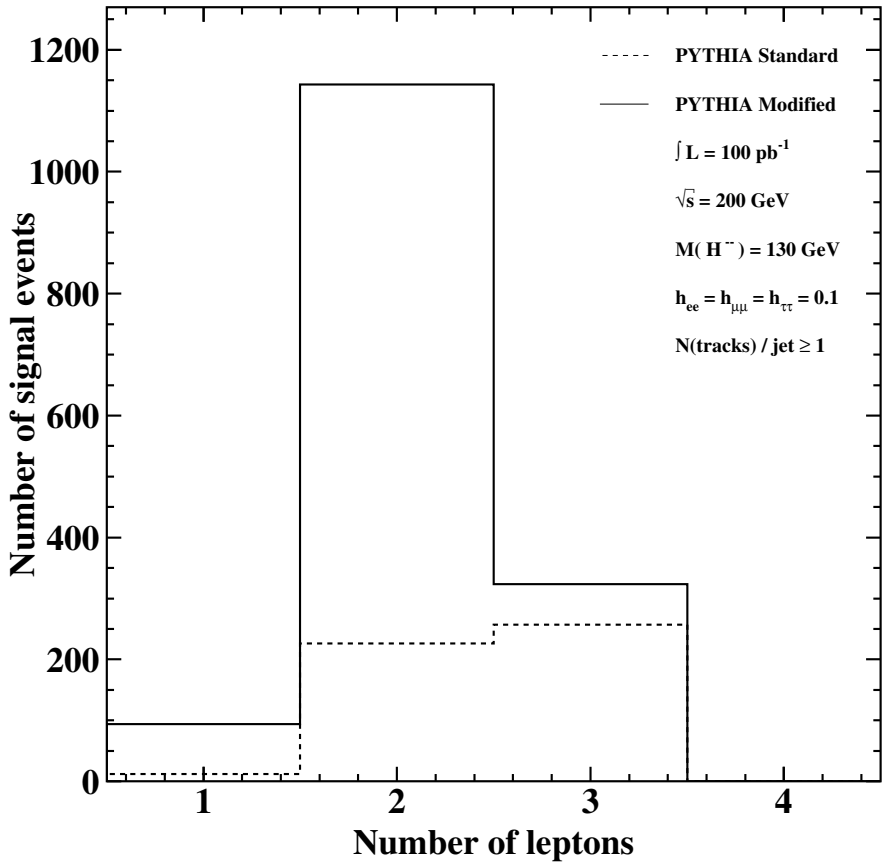

Figure 4.3: *Comparison of the generated number of leptons in PYTHIA.*

4.3 Simulation of SM Processes

4.3.1 Physics Processes at LEP

At centre-of-mass energies well above the Z-resonance the following processes are the most important SM processes in e^+e^- collisions.

4.3.2 Two-Photon Processes

The term two-photon process is used for reactions of type $e^+e^- \to e^+e^- f\bar{f}$, which proceed via the exchange of two photons. The graph in figure 4.4 illustrates this kind of events.

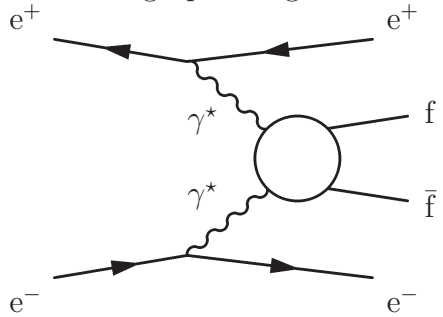

Figure 4.4: A diagram of the reaction $e^+e^- \to e^+e^-f\bar{f}$, proceeding via the exchange of two photons.

The spectrum of two-photon processes is manifold. A first categorisation is based on the photons' virtuality, Q^2, which is defined as the negative squared four-momentum: $Q^2 = -q^2 = -(E^2 - \vec{p}^2)$. The photons are called quasi-real if the Q^2 is small. In this case the corresponding electron transfers only a small transverse momentum to the photon and the electron disappears in the beam pipe. With increasing virtuality the beam electrons carry a larger transverse momentum and eventually will be deflected into the detector. Depending on the number of beam electrons visible in the detector the two-photon events are called un-tagged, single-tagged or double-tagged.

The photons are able to have different appearances in the detector. Besides the direct or bare appearance the photon is allowed due to the Heisenberg Uncertainty Principle to fluctuate into a charged fermion anti-fermion system. The photon is also able to fluctuate into a hadronic state, which interacts subsequently.

The two-photon cross-section is as large as $\mathcal{O}(10\text{ nb})$ at $\sqrt{s} = 200$ GeV in case of un-tagged hadron-like processes. The cross-section rises logarithmically with the centre-of-mass energy. An elaborate review on the nature of the photon can be found in [38].

The Monte Carlo generators PHOJET [39] (for $Q^2 < 4.5$ GeV ^{2}) and HERWIG [40] (for $Q^2 \geq 4.5$ GeV ^{2}) are used to simulate two-photon collisions resulting in hadronic final states. Four-fermion processes $e^+e^- \to \ell^+\ell^-\ell'^+\ell'^-$ include the so-called multi-peripheral diagrams $e^+e^- \to e^+e^-\gamma^{(*)}\gamma^{(*)} \to e^+e^-\ell^+\ell^-$, which are here dedicated to the two-photon processes. The multi-peripheral diagrams are simulated with the dedicated two-photon event generators Vermaseren [41] for $e^+e^- \to e^+e^-\gamma^{(*)}\gamma^{(*)} \to e^+e^-e^+e^-$ and BDK [42] for $e^+e^- \to e^+e^-\gamma^{(*)}\gamma^{(*)} \to e^+e^-\mu^+\mu^-$ and $e^+e^- \to e^+e^-\gamma^{(*)}\gamma^{(*)} \to e^+e^-\tau^+\tau^-$. RADCOR [43] is used to simulate multi-photon events from QED processes.

4.3.3 Four-Fermion Processes

Four-fermion processes include all kind of electroweak processes (excluding the multi-peripheral processes) with four fermions in the final state. The Feynman diagrams of the most important four fermion processes are shown in figure 4.5. Four-fermion final states are produced by W and Z pair-production, single W and single Z production in Compton scattering of quasi-real photons. The cross-sections are of order 50 pb at centre-of-mass energies of $\sqrt{s} = 200$ GeV.

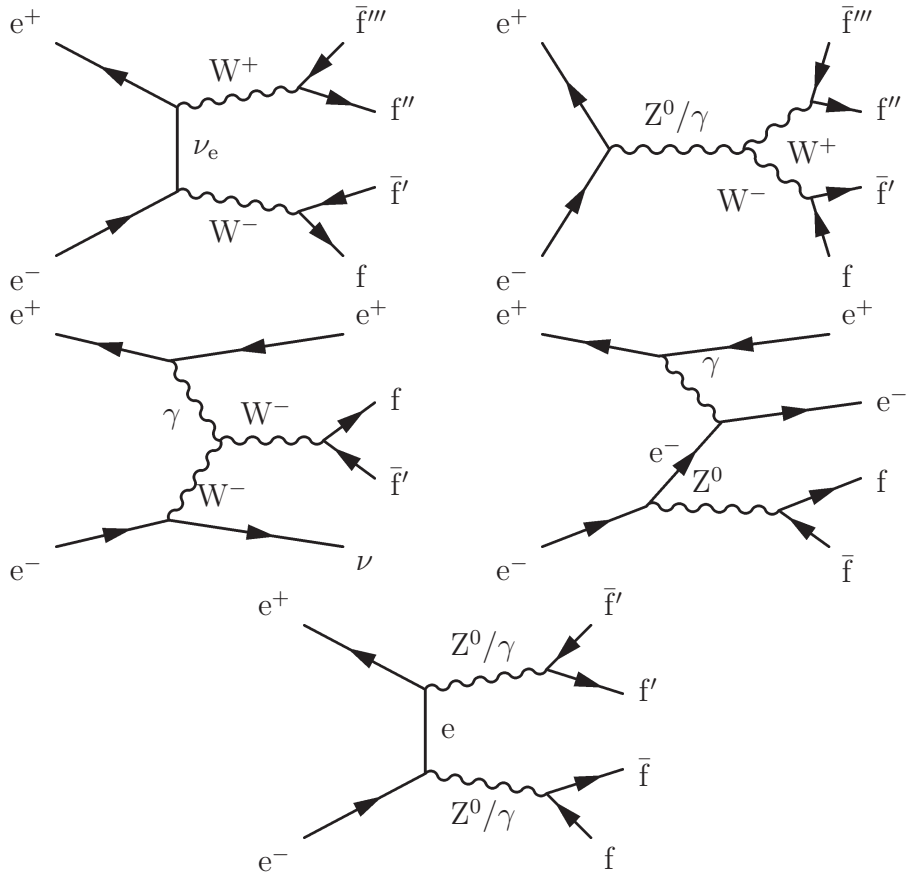

Figure 4.5: Feynman-diagrams of the most important four fermion processes: W pair production, single gauge boson production, pair production of neutral gauge bosons.

Four-fermion processes $e^+e^- \to \ell^+\ell^-\ell'^+\ell'^-$, including events from the so-called multi-peripheral diagrams $e^+e^- \to e^+e^-\gamma^{(*)}\gamma^{(*)} \to e^+e^-\ell^+\ell^-$ (see section 4.3.2 are the dominant SM background in this analysis. Four fermion processes except $e^+e^- \to e^+e^-\ell^+\ell^-$ ($\ell = e, \mu, \tau$) and $e^+e^- \to e^+e^-q\bar{q}$ are simulated with the KORALW [44] event generator. The non-multi-peripheral part of the processes $e^+e^- \to e^+e^-\ell^+\ell^-$ and $e^+e^- \to e^+e^-q\bar{q}$ is simulated with grc4f2.1 [45].

4.3.4 Two-Fermion Processes

Besides the four-fermion processes, also the lepton pairs $e^+e^- \to \ell^+\ell^-$ have a large contribution to the SM background. The annihilation of an e^+e^- pair into a neutral gauge boson (γ or Z) and the subsequent decay of the boson into a fermion-anti-fermion pair is the so-called two-fermion process (see figure 4.6). The production cross-section for these events reaches a maximum at the Z-resonance and drops with increasing centre-of-mass energy as $1/s$ for $\sqrt{s} \gg M_Z$.

Lepton pairs are simulated using the KK2f [46] generator for $\tau^+\tau^-(\gamma)$ and $\mu^+\mu^-(\gamma)$ events and the multi-hadronic final states $q\bar{q}(g\gamma)$. NUNUGPV [47] for $\nu\bar{\nu}\gamma(\gamma)$. Bhabha scattering is simulated with BHWIDE [48] (when both the electron and positron scatter at least 12.5° from the beam axis) and TEEGG [49] (for the remaining phase space). Multihadronic events, $q\bar{q}(\gamma)$, are simulated using KK2f [46].

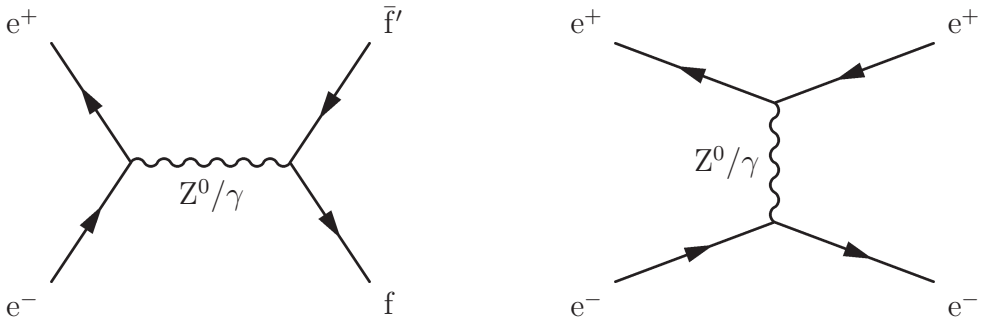

Figure 4.6: Feynman-diagrams of the s- and t-channel two fermion processes.

4.3.5 Two-photon Production

The process $e^+e^- \to \gamma\gamma(\gamma)$, the production of two photons via an e^+e^- annihilation, shall only be mentioned for sake of completeness. The Feynman diagram is shown in figure 4.7.

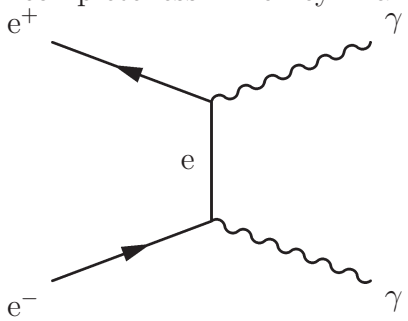

Figure 4.7: Production of two photons via e^+e^- annihilation.

The purely photonic final states make a negligible contribution to the background.

A summary of all considered physics processes, their generators and the size of the generated data samples used for this analysis is given in table 4.1.

4.4 The Detector Simulation

The detector response to the generated events is modelled with detector simulations. In these programs the detector geometry and the properties of all active and passive detector components are implemented. Based on the four-momenta produced with the event generators, the detector simulations calculate the reactions of these particles with the material of the detector components like ionisation loss of charged particles, shower evolution in the detector material and multiple scattering of particles.

In figures 4.8 and 4.10 simulated doubly-charged Higgs bosons events are shown. The process $e^+e^- \to e^\pm e^\pm H^{\mp\mp} \to e^\pm e^\pm \mu^\mp \mu^\mp$ at centre-of-mass energy of 200 GeV for a doubly-charged Higgs boson of 130 GeV is simulated. The former figure represents the kind of events, where only two leptons (in this case: two μs) originating from the doubly-charged Higgs boson decay are visible in the detector, whereas two positrons (or electrons) are close to the beamline and are not detected. The latter figure represents the kind of events, where only the electron or positron, which radiated the photon is not detected in the detector. The figures 4.9 and 4.11 are showing the same events including the jet and missing energy reconstruction.

final state	generator	$\sqrt{s}$=189 GeV σ [pb]	$\sqrt{s}$=189 GeV $\int\mathcal{L}$ dt [pb^{-1}]	$\sqrt{s}$=192 GeV σ [pb]	$\sqrt{s}$=192 GeV $\int\mathcal{L}$ dt [pb^{-1}]	$\sqrt{s}$=196 GeV σ [pb]	$\sqrt{s}$=196 GeV $\int\mathcal{L}$ dt [pb^{-1}]	$\sqrt{s}$=200 GeV σ [pb]	$\sqrt{s}$=200 GeV $\int\mathcal{L}$ dt [pb^{-1}]	$\sqrt{s}$=202 GeV σ [pb]	$\sqrt{s}$=202 GeV $\int\mathcal{L}$ dt [pb^{-1}]	$\sqrt{s}$=206 GeV σ [pb]	$\sqrt{s}$=206 GeV $\int\mathcal{L}$ dt [pb^{-1}]	comment
two-photon processes														
$e^+e^-q\bar{q}$	PHOJET	11 623	94	11 623	94	11 285	89	11 433	88	11 424	88	11 287	85	un-tagged
$e^+e^-q\bar{q}$	HERWIG	302	497	310	1 129	310	500	314	501	321	1 089	326	1 013	single-tagged
$e^+e^-q\bar{q}$	PHOJET	3.4	2 388	3.4	2 388	3.4	2 388	3.5	2 471	3.5	2 471	3.3	3 293	double-tagged
$e^+e^-e^+e^-$	VERMASEREN	805	99	805	99	824	1 002	825	1 000	870	954	878	968	
$e^+e^-\mu^+\mu^-$	BDK	607	1 071	606	1 072	612	1 063	613	1 061	615	1 058	617	1 134	
$e^+e^-\tau^+\tau^-$	BDK	444	1 463	448	1 450	454	1 103	459	1 091	462	1 408	464	1 077	
four-fermion processes														
$\ell\ell\ell'\ell'$	KORALW	3.2	19 997	3.2	5 000	3.3	10 000	3.3	20 001	3.4	9 999	3.4	20 003	$\ell = \mu, \tau$
$\ell\bar{\ell}q\bar{q}$	KORALW	8.8	20 001	9.0	5 000	9.2	10 000	9.3	20 001	9.4	10 000	9.4	20 001	$\ell = \mu, \tau$
$q\bar{q}q'\bar{q}'$	KORALW	8.6	20 000	8.7	5 000	8.9	10 000	9.0	19 999	9.0	10 000	9.1	20 001	
$e^+e^-e^+e^-$	grc4f	18.4	5 000	18.1	5 000	17.7	5 000	17.4	5 000	17.3	5 000	16.9	5 000	
$e^+e^-\mu^+\mu^-$	grc4f	12.7	5 000	12.7	5 000	12.3	5 000	12.1	5 000	11.8	5 000	11.6	5 000	
$e^+e^-\tau^+\tau^-$	grc4f	1.8	5 000	1.8	5 000	1.8	5 000	1.8	5 000	1.8	5 000	1.7	5 000	
$e^+e^-q\bar{q}$	grc4f	25.6	4 989	41.4	5 000	59.5	3 403	39.5	5 000	39.0	5 000	38.2	5 000	
two-fermion processes														
$q\bar{q}(\gamma)$	KK2f	100	2 512	94.8	2 636	90.1	2 775	85.6	3 506	83.4	2 999	79.5	3 146	
$e^+e^-(\gamma)$	BHWIDE	596	1 426	577	751	554	752	532	779	521	384	502	398	s-channel
$e^+e^-(\gamma)$	TEEGG	706	992	693	144	677	296	665	601	657	380	644	388	t-channel
$\mu^+\mu^-(\gamma)$	KK2f	8.5	9 392	8.3	6 044	7.9	6 336	7.5	7 980	7.4	6 787	7.0	11 360	
$\tau^+\tau^-(\gamma)$	KK2f	8.2	9 735	8.0	6 231	7.7	6 511	7.3	8 168	7.2	6 975	6.9	11 626	
$\nu\bar{\nu}(\gamma)$	NUNUGPV	8.8	5 700	8.8	2 275	8.5	11 722	8.3	12 054	8.2	6 130	8.0	1 251	
others														
$\gamma\gamma(\gamma)$	RADCOR	24	4 739	24	1 000	23	1 000	22	4 000	21	1 000	21	4 000	

Table 4.1: *Summary of all SM background Monte Carlo samples used for the analysis.*

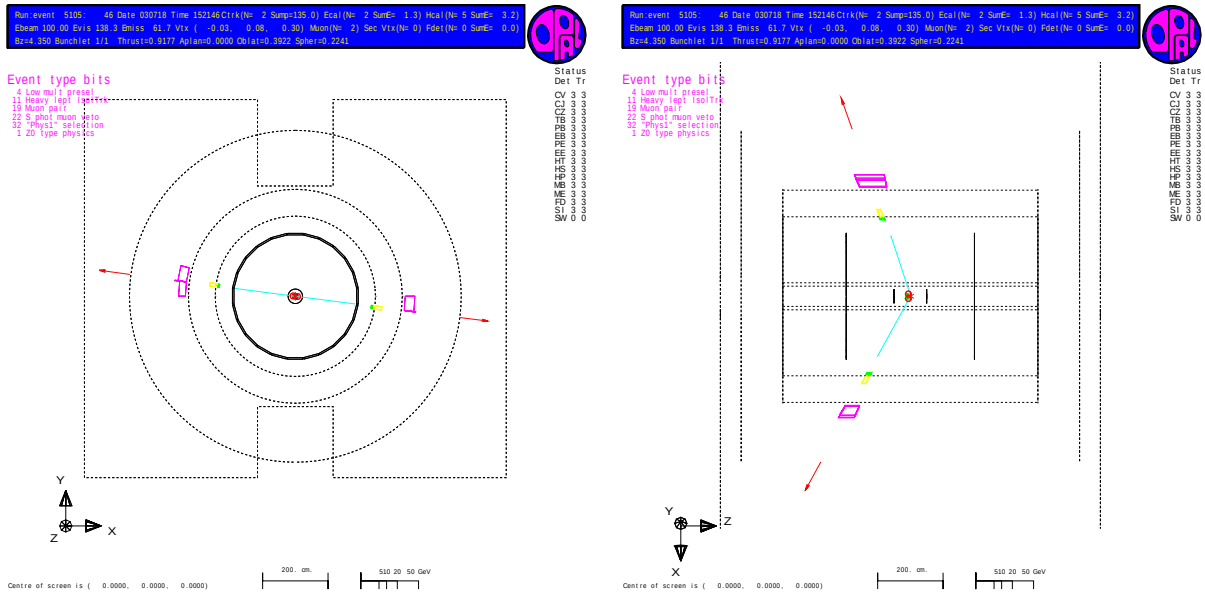

Figure 4.8: *Detector Simulation of a doubly-charged Higgs decay into two μ.*

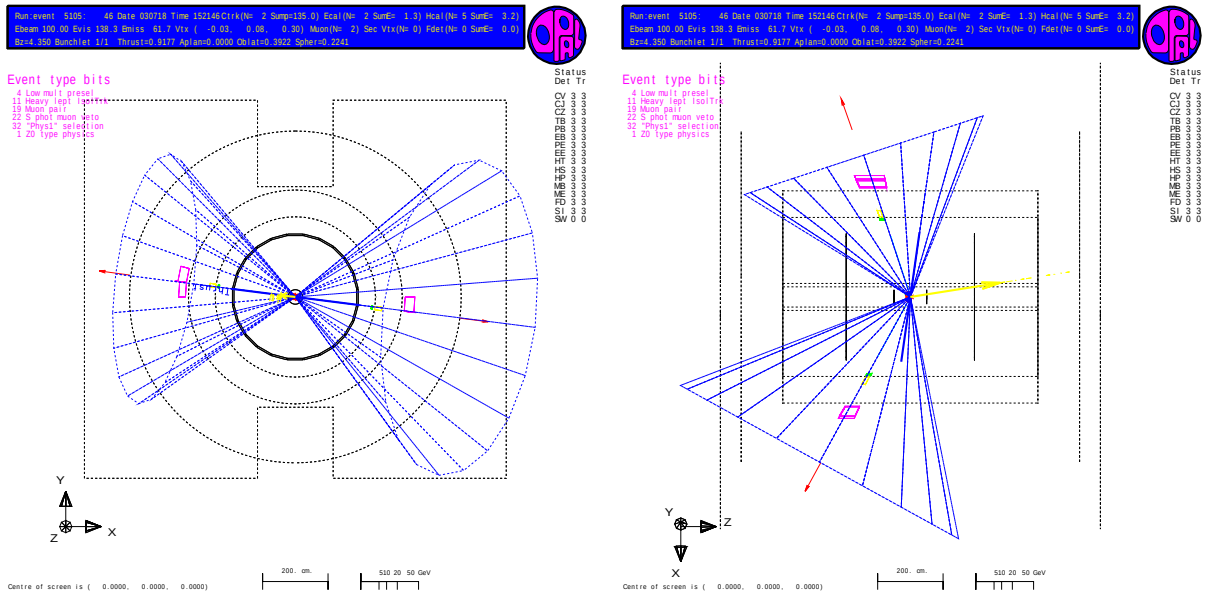

Figure 4.9: *Detector Simulation of a doubly-charged Higgs decay into two μ with jet-reconstruction.*

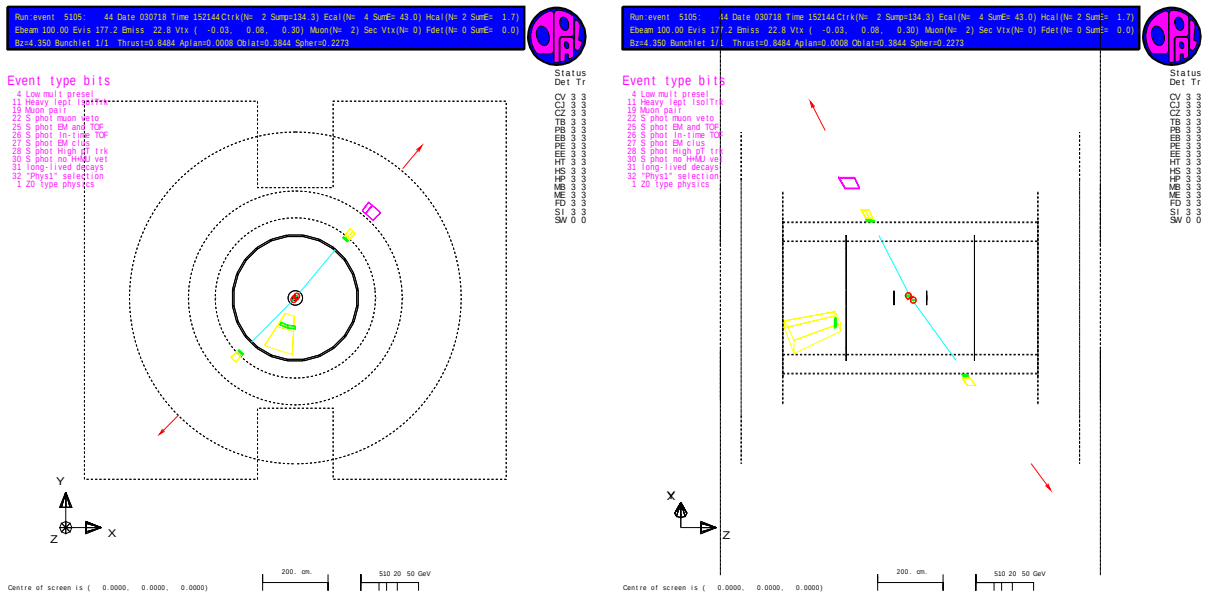

Figure 4.10: *Detector Simulation of a doubly-charged Higgs decay into two μ and one remaining e.*

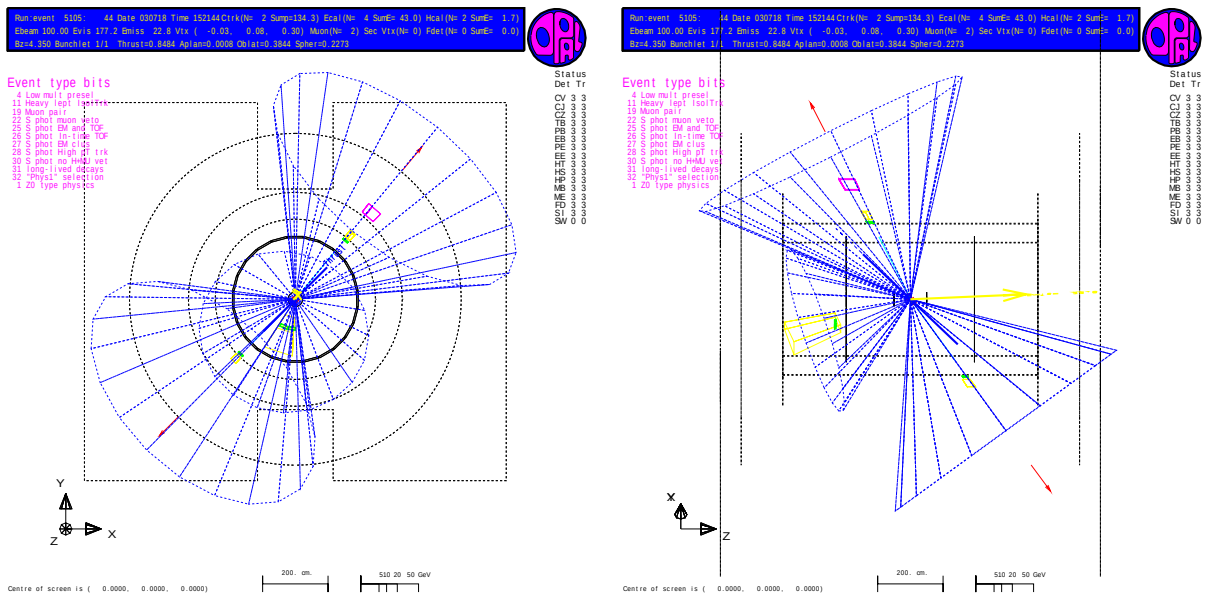

Figure 4.11: *Detector Simulation of a doubly-charged Higgs decay into two μ and one remaining e with jet-reconstruction.*

The OPAL detector was simulated with GOPAL [50], a program based on the GEANT3 [51] package. Both data and Monte Carlo events were reconstructed with the ROPE [35] program. Generated signal and background events are processed through the full simulation of the OPAL detector and the same event analysis chain was applied to the simulated events as to the data.

After the reconstruction of both data and simulated Monte Carlo events, the necessary input for the analysis is complete (compare figure 4.12).

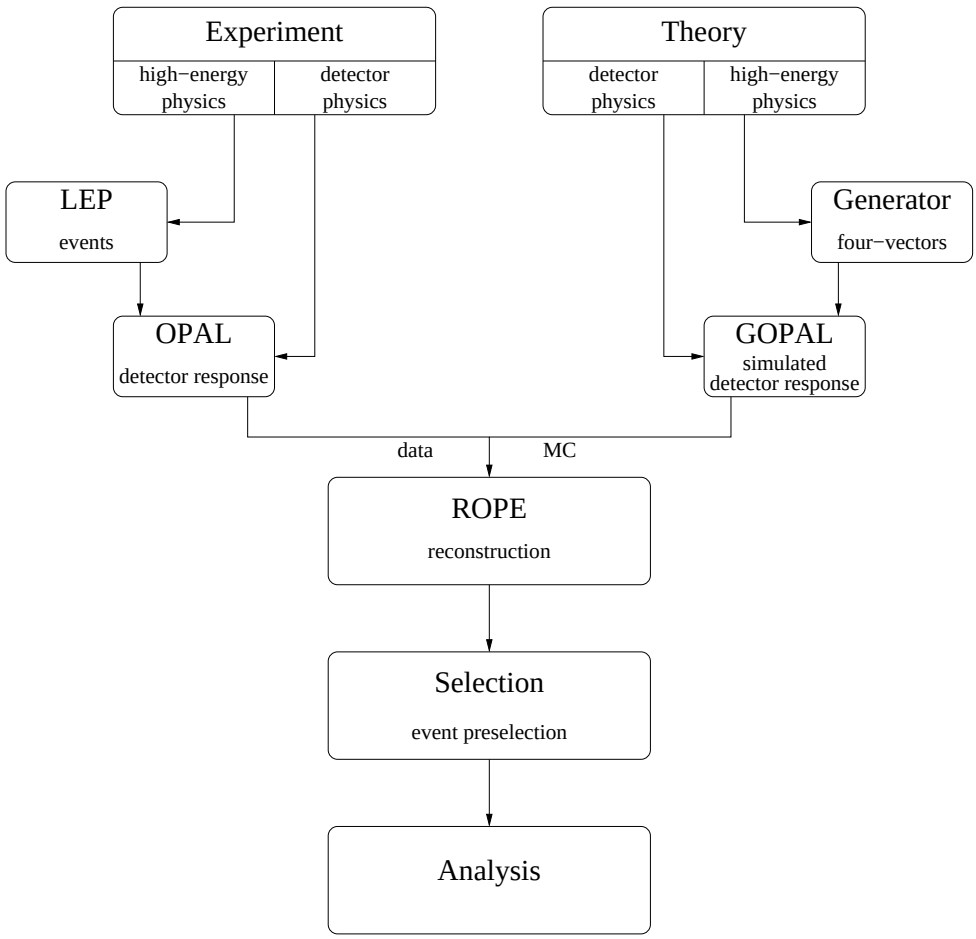

Figure 4.12: *Production and processing of data and Monte Carlo.*

The left branch describes the experimental input, which includes all steps to gain real data from the detector. The right branch describes all steps, which are needed to simulate Monte Carlo events. Both branches are routed to the reconstruction. After the reconstruction, the event selection and finally the analysis, which include the calculation of the interesting parameters and the interpretation of the results, follows. These last steps are described in the following chapters.

Chapter 5

The Selection

In this chapter, the search for the single production of doubly-charged Higgs bosons is described, assuming the decays $H^{\pm\pm} \to \ell^{\pm}\ell'^{\pm}$. Since the production cross-section depends only on h_{ee}, the Yukawa coupling of the $H^{\pm\pm}$ to like-signed electron pairs, this search is sensitive to this quantity.

In the following sections, the analysis including selection and calculation of the interesting parameters is described. A description about the topology of the expected signal in the OPAL detector is given, followed by a list of the used cuts to separate the expected signal from the SM background.

5.1 The Analysed Data Sample

The data, which are analysed were taken in 1998, 1999 and 2000 at centre-of-mass energies, $\sqrt{s}$, between 189 and 209 GeV. The growth of the integrated luminosity during the whole period of data taking is illustrated in figure 5.1. Since this analysis is designed to find a relatively heavy particle, just the data with high centre-of-mass energies are considered. The search is based on a total of 600.7 pb^{-1} of e^+e^- collision data. The luminosity weighted mean centre-of-mass energy and the integrated luminosity of each energy bin is listed in table 5.1. Some detector status cuts are applied. It is required, that the central tracking detectors, the electromagnetic and hadronic calorimeter detectors are calendared as alright.

E_{cm} (GeV)	$\langle E_{\mathrm{cm}} \rangle$ (GeV)	$\int \mathcal{L}$ (pb^{-1})
188 – 190	188.6	175.0
190 – 194	191.6	28.9
194 – 198	195.5	74.8
198 – 201	199.5	78.1
201 – 203	201.7	38.2
203 – 206	205.0	79.4
206 – 209	206.6	126.1
188 – 209	197.7	600.7

Table 5.1: *Data samples used in the analysis.*

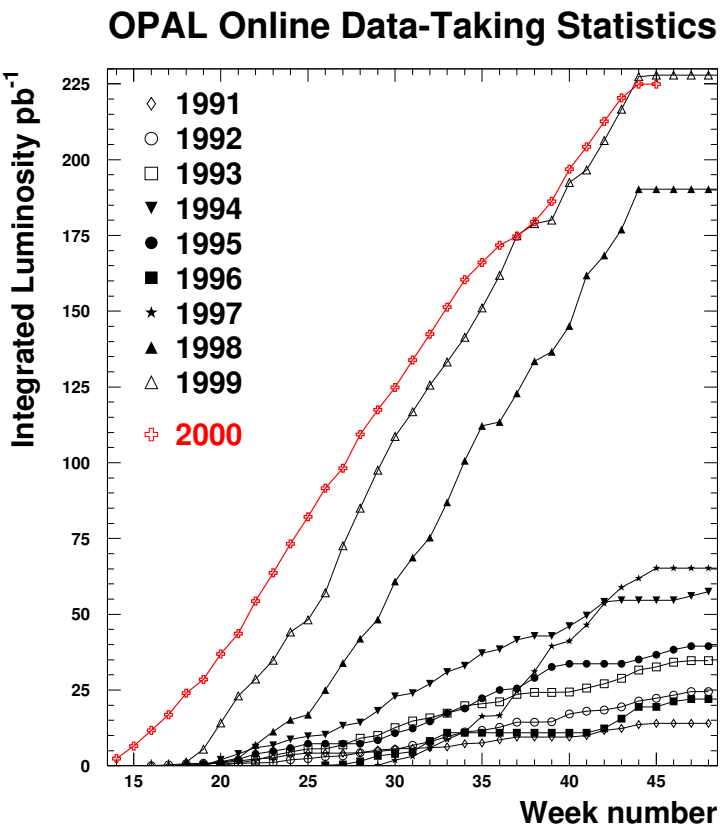

Figure 5.1: *Integrated luminosity collected during the entire data taking period of OPAL running.*

5.2 The Generated Signal Samples

The signal final state consists of four charged leptons. Two like-signed leptons originate from the $H^{\pm\pm}$ decay and are expected to be visible in the detector in most cases. The electron or positron, which originates from the eeγ vertex (see Fig. 2.3), in general escapes through the beampipe. The electron or positron, which originates from the ee$H^{\pm\pm}$ vertex, is also forward peaked; however, it enters the detector in a significant fraction of signal events. The selection and the corresponding analysis is, therefore, divided into a two-lepton and a three-lepton part. The final states in the three-lepton case contain three leptons visible in the detector, two of them have the same sign and could originate from the decay of a doubly-charged Higgs boson. In the two-lepton case, two like-signed leptons are required, as expected in the decay of a doubly-charged Higgs boson.

Separate signal samples are simulated with the 6 different decay modes (ee, $\mu\mu$, $\tau\tau$,eμ, eτ, $\mu\tau$). Samples of 500 events each are generated for each of the average centre-of-mass energies listed in table 5.1 for $H^{\pm\pm}$ masses in 5 GeV steps from 90–200 GeV. For masses larger than twice the W boson mass the decay $H^{\pm\pm} \rightarrow W^{\pm}W^{\pm}$ is kinematically allowed. Its partial width, however, is negligible in most models [23]. In this analysis, the branching fraction BR($H^{\pm\pm} \rightarrow W^{\pm}W^{\pm}$) is assumed to be zero.

Leptons are identified as low multiplicity jets. Jets are reconstructed from charged particle tracks and energy deposits (clusters) in the electromagnetic and hadron calorimeters.

5.3 The Selection Criteria

The selection is a sequence of requirements, which the events have to fulfill. The aim is to separate doubly-charged Higgs events from SM events. The sequence is divided into two main parts: the pre-selection and the main selection.

5.3.1 The Pre-Selection

The pre-selection is also divided into two parts, which are based on the existence of the used standard OPAL analysis routines. The first one is the "Low Multiplicity Criteria" [52] and the second one is the selection criteria of a part from the "Track and Cluster Selection" [53] routines.

The Low Multiplicity Selection

The low multiplicity selection (LOWM) [52] requires that events satisfy **any** of the following conditions

- A track with momentum $P_{xy} > 0.7$ GeV, $|d_0| < 1$ cm, $|z_0| < 50$ cm and at least 20 hits in the central detector (CV+CJ+CZ). P_{xy} is the transverse momentum, d_0 is the distance between the point of closest approach (p.c.a.) of the track and the origin and z_0 is the z coordinate of the p.c.a.

- A track in the Muon Endcap (ME) that, when projected back to the z=0 plane, is within 20 cm of the beam spot. Muon tracks are only considered, if there are at most four tracks reaching the endcaps.

- At least two electromagnetic clusters with total corrected energy > 6 GeV.

- Two electromagnetic clusters that are back to back to within 25 degrees, one of which has total corrected energy > 2 GeV.

In addition a loose high multiplicity veto is applied. Events have to fulfill:

$$N_{track} + N_{cluster} < 18, \tag{5.1}$$

where N_{track} is the number of tracks in the central detector and $N_{cluster}$ is the number of clusters in the electromagnetic calorimeter. Tracks are counted if they have: $P_{xy} > 0.100$ GeV, $|d_0| < 1$ cm, $|z_0| < 20$ cm and at least 20 hits in the central detector (CV+CJ+CZ), the first of which is at a radius of less than 75 cm. Barrel electromagnetic clusters are counted if they have a raw energy $E > 0.1$ GeV. Endcap electromagnetic clusters are counted if they have a raw energy $E > 0.2\,\text{GeV}$, if they contain at least two blocks, and if the fraction of the total energy of the cluster given by the most energetic block is less than 99%.

The Track and Cluster Selection

After the low multiplicity preselection, tracks and clusters have to require some more qualities [53]. The OPAL WW event selection package uses different quality cuts to define tracks and clusters. For example the $W^+W^- \to l^+\nu_l l'^-\bar{\nu_{l'}}$ set of cuts excludes all hadron calorimeter information and allows tracks having relatively high momentum to be selected. Formally, there are four such sets of quality cuts: the default general set, the fully hadronic '$q\bar{q}q\bar{q}$' set, the semi leptonic '$q\bar{q}l^{\pm}\nu_l$' set and the fully leptonic '$l^+\nu_l l'^-\bar{\nu_{l'}}$' set. However, in this selection just the latter '$l^+\nu_l l'^-\bar{\nu_{l'}}$' set of quality cuts is used, because the expected signal topology contains leptons of all flavours with relatively high momentum. In contrast to the low multiplicity preselection, the tracks have at this part to fulfill all requirements, which are listed below.

- Remove poor quality tracks and tracks from conversions.
  The requirements are: $P_{xy} > 0.150$ GeV, $|d_0| < 2$ cm, $|z_0| < 25$ cm and a requirement that there be at least 20 hits on the track.

- In addition a stronger high multiplicity veto is applied. Events have to fulfill:

$$1 \leq N_{track} \leq 8, \tag{5.2}$$

$$N_{track} + N_{cluster} < 16. \tag{5.3}$$

  This means that the events are additionally required to have at least two and less than nine charged tracks and that the sum of charged tracks and clusters in the electromagnetic calorimeter must be less than 16. N_{track} is the number of tracks in the central detector, which fullfil the track requirements, and $N_{cluster}$ is the number of clusters in the electromagnetic calorimeter. Barrel electromagnetic clusters are counted, if they have a raw energy $E > 0.10$ GeV. Endcap electromagnetic clusters are counted, if they have a raw energy $E > 0.25\,\text{GeV}$ and they contain at least two blocks.

The selected events have to satisfy both the LOWM and the track and cluster requirements. Tracks and clusters are defined to be of "good" quality after these requirements.

After the jet reconstruction, double-counting of energy between tracks and calorimeter clusters is corrected by reducing the calorimeter cluster energy by the expected energy deposition from associated charged tracks, including particle identification information.

Tracks and clusters are formed into jets using a cone algorithm [54] with a half-angle of 20 degrees and a minimum jet energy of 2.5 GeV. No explicit electron or muon identification is required, since it is found that the jet-based analysis technique retains high efficiency while reducing the background to an acceptable level.

5.3.2 Main Selection

After the selection of tracks and clusters of "good" quality and forming them into jets using a cone algorithm, the next cuts are applied to separate the expected signal of the doubly-charged Higgs boson $H^{\pm\pm}$ from the remaining background. To achieve this, it is necessary to investigate the distribution of several quantities of the signal and compare them with the distribution of background events. The main selection is divided into the

two-lepton and three-lepton part, because it is necessary to adjust the requirements for each part. Therefore, the cut values of the two-lepton and three-lepton selection differ slightly.

The requirements for the two-lepton selection are:

(2.1) It is required that the jet finder discovers exactly two jets with polar angles satisfying $|\cos\theta| < 0.95$, and which are not precisely back-to-back (within 5°). The sum of the energies of the two jets reconstructed in the event must be greater than 20% of $\sqrt{s}$.

(2.2) Ordering the jet energies by their magnitude ($E_{\text{jet1}} > E_{\text{jet2}}$), the following requirements are made:

a) $E_{\text{jet1}} > 0.1\sqrt{s}$;

b) $E_{\text{jet2}} > 0.05\sqrt{s}$;

c) $E_{\text{jet1}} < 0.995 E_{\text{beam}}$;

d) $E_{\text{jet1}} + E_{\text{jet2}} < 0.95\sqrt{s}$.

These requirements are plotted in figure 5.2(a – d).

(2.3) The invariant mass M_{inv} of the two jets must satisfy $M_{\text{inv}} > 40$ GeV. Typical mass resolutions are about 4 GeV for ee and 10 GeV for $\mu\mu$. No mass reconstruction is possible for $\tau\tau$, due to the undetected neutrinos. The mass distribution is plotted in 5.2(e).

(2.4) Bhabha scattering is rejected by requiring that the acollinearity angle, ϕ_{acol}, satisfies $\phi_{\text{acol}} > 25°$. The angle ϕ_{acol} is defined to be 180° minus the opening angle of the two jets. The ϕ_{acol} distribution is plotted in figure 5.2(f).

(2.5) The polar angle of each jet must satisfy $|\cos\theta| < 0.75$. The $H^{\pm\pm}$ candidate jet polar angles are plotted in figures 5.3(a) and (b) after cuts (2.1)–(2.4).

(2.6) Each jet associated to the $H^{\pm\pm}$ must have either one or three charged tracks. The number of charged tracks is plotted in figure 5.3(c) after cuts (2.1)–(2.5).

(2.7) Defining the sum of the track charges within each jet as the "jet charge", the product of the charges of the two jets must be equal to +1. This value is plotted in figure 5.3(d) after cuts (2.1)–(2.6).

The requirements for the three-lepton selection are:

(3.1) It is required that the jet finder discovers exactly three jets with polar angles satisfying $|\cos\theta| < 0.95$, and which are not precisely back-to-back (within 5°). The two jets, which have the highest reconstructed mass, as described in cut (3.3), have to satisfy $|\cos\theta| < 0.95$ and must not be precisely back-to-back (within 5°). There is no $|\cos\theta|$ requirement for the third jet. The sum of the energies of the three jets reconstructed in the event must be greater than 20% of $\sqrt{s}$.

(3.2) Ordering the measured jet energies by their magnitude ($E_{\text{jet1}} > E_{\text{jet2}} > E_{\text{jet3}}$), the following requirements are made:

a) $E_{\text{jet1}} > 0.1\sqrt{s}$;

b) $E_{\text{jet2}} > 0.05\sqrt{s}$;

c) $E_{\text{jet3}} > 0.025\sqrt{s}$ or it must contain at least one good charged track;

d) $E_{\text{jet1}} < 0.995 E_{\text{beam}}$;

e) $E_{\text{jet1}} + E_{\text{jet2}} + E_{\text{jet3}} < 0.95\sqrt{s}$.

These requirements are plotted in figure 5.4(a – d).

(3.3) The jet energies are determined assuming that the measured jet direction is the same as the initial lepton direction for each of the reconstructed jets and that the missing electron or positron is recoiling along the beam axis. Using energy and momentum conservation to give four constraint equations, the four jet energies can be inferred (the lepton masses are neglected). Using this improved determination of the jet energies, the invariant masses are calculated for the three possible di-jet systems, that can be constructed from the observed jets. The two jets having the largest di-jet mass are considered as the $H^{\pm\pm}$ candidate jets with a "reconstructed Higgs boson mass" M_{rec}. The loss due to this assumption is negligible for $H^{\pm\pm}$ masses above 110 GeV and is taken into account in the signal efficiency calculation. Since this search concentrates on the region above the mass limit from pair creation, it is further required that M_{rec} satisfy $M_{\text{rec}} > 80$ GeV. Typical mass resolutions are about 1 GeV for ee and $\mu\mu$ modes, and about 4 GeV for $\tau\tau$ decays. Note that in the latter case, no mass reconstruction from the jet energies would have been possible without this procedure, due to the undetected neutrinos. The mass distribution is plotted in 5.4(e)

(3.4) Bhabha scattering is rejected by requiring that the acollinearity angle between the two $H^{\pm\pm}$ candidate jets satisfies $\phi_{\text{acol}} > 15°$. The ϕ_{acol} distribution is plotted in figure 5.4(f).

(3.5) The polar angle of each jet associated to the $H^{\pm\pm}$ must satisfy $|\cos\theta| < 0.80$. The $H^{\pm\pm}$ candidate jet polar angles are plotted in figures 5.5(a) and (b) after cuts (3.1)–(3.4).

(3.6) Each jet associated to the $H^{\pm\pm}$ must have either one or three charged tracks. The number of charged tracks is plotted in figure 5.5(c) after cuts (3.1)–(3.5).

(3.7) Defining the sum of the track charges within each jet as the "jet charge", the product of the charges of the two jets associated with the $H^{\pm\pm}$ must be equal to +1. This value is plotted in figure 5.5(d) after cuts (3.1)–(3.6).

The same selection is used to search for all 6 possible lepton flavour combinations, and the results are valid for all leptonic decay modes of the $H^{\pm\pm}$. The results are summarised in table 5.2 for the unmixed decay channels ee, $\mu\mu$ and $\tau\tau$ and also for the mixed decay channels eμ, eτ and $\mu\tau$. The numbers of observed and expected events agree well after each cut in all channels. The final background is dominated by SM processes containing four charged leptons.

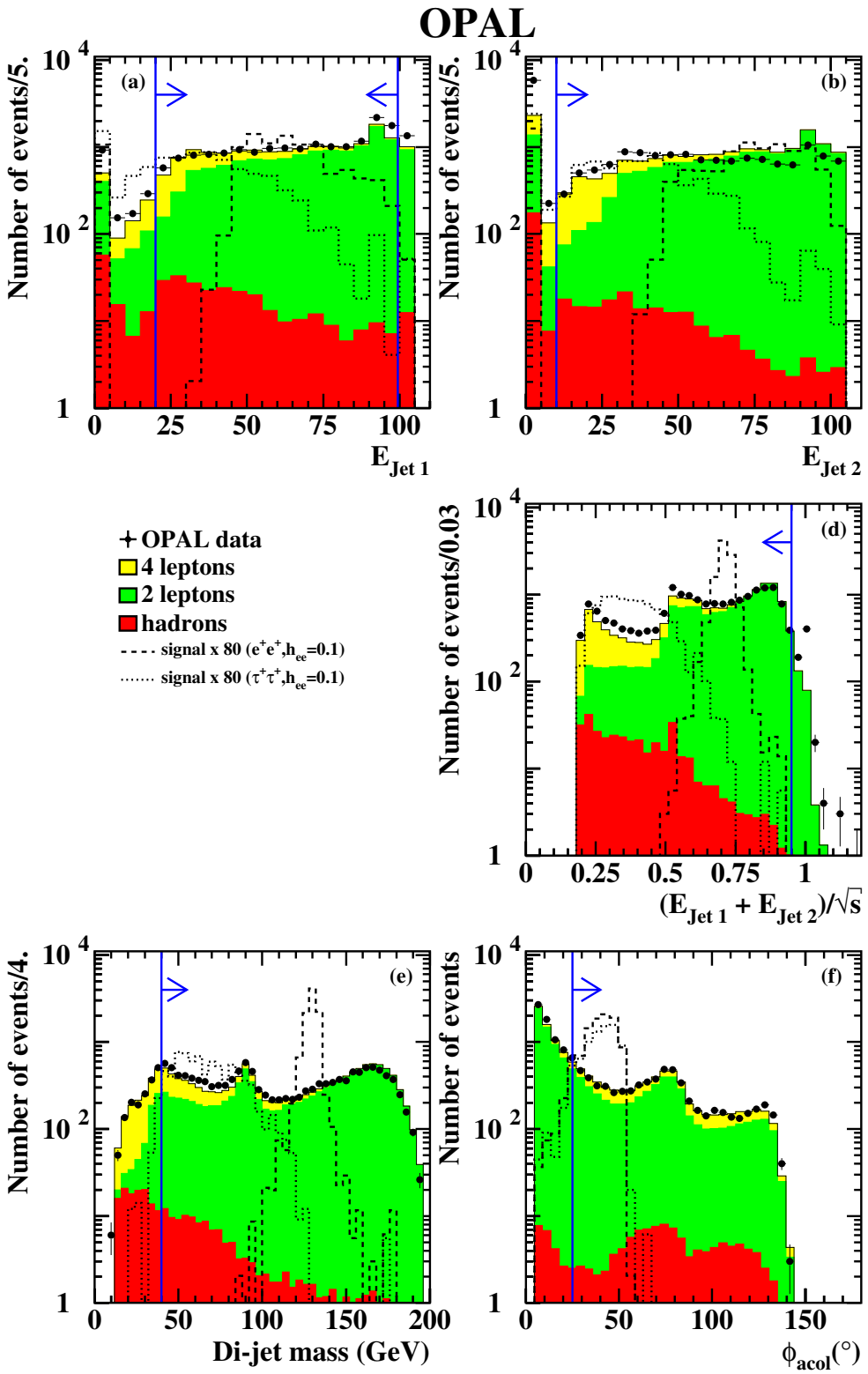

Figure 5.2: *Examples of some of the quantities used in the two-lepton selection shown immediately before the corresponding cut is applied (see Chapter 5). The energies of jet 1 (a) and jet 2 (b), sorted by their energies are shown. The sum of the jet energies is shown in (d). The reconstructed mass of the two* $H^{\pm\pm}$ *candidate jets is shown in (e) and finally the acollinearity angle* ϕ_{acol} *is shown in (f). The legend description is done in the caption of figure 5.3. The cut requirements are indicated by the arrows.*

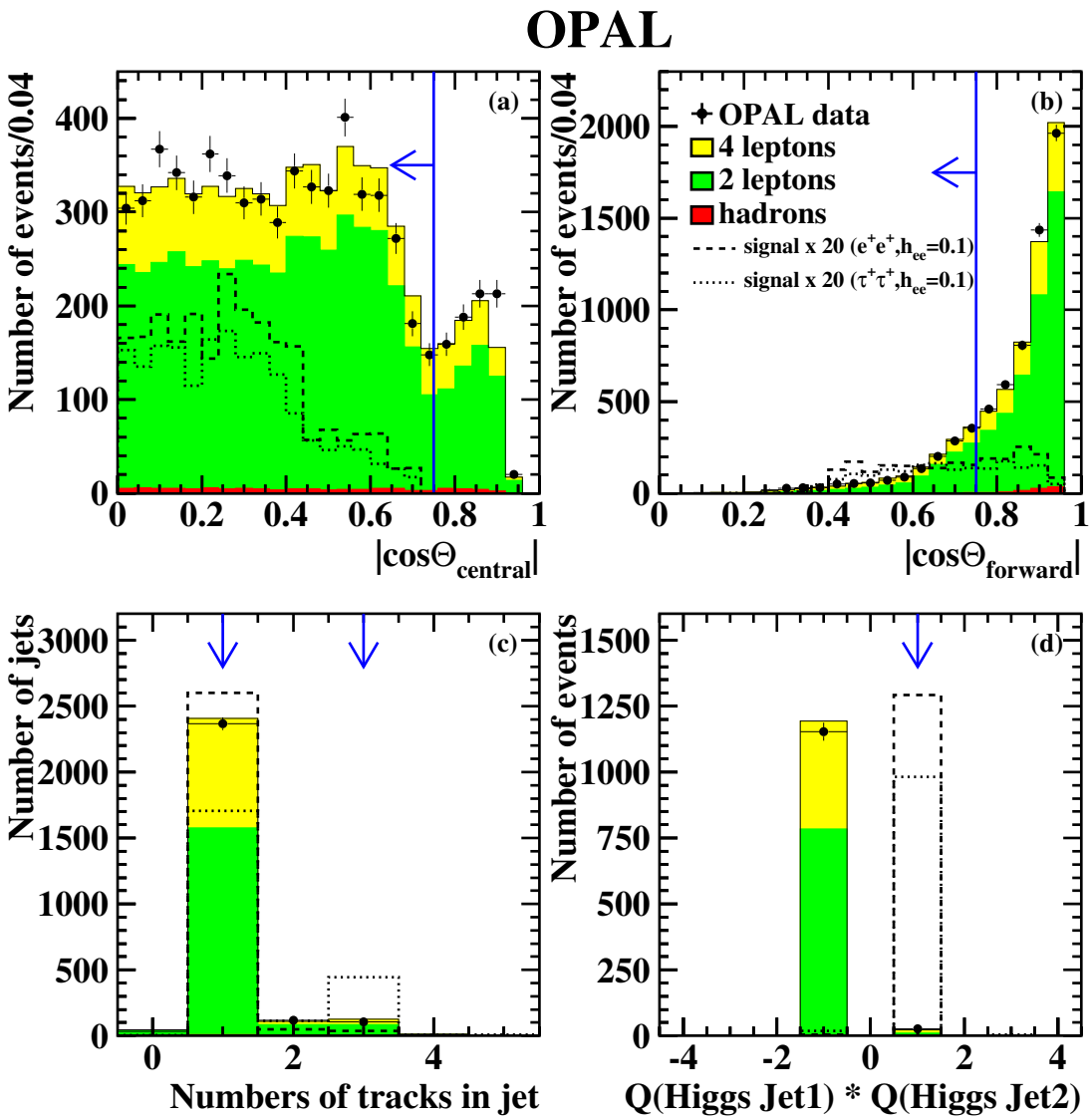

Figure 5.3: *Examples of some of the quantities used in the two-lepton selection shown immediately before the corresponding cut is applied (see Chapter 5). The absolute values of the cosines of the polar angle of the more central and the more forward Higgs boson candidate jets are shown in (a) and (b), the number of charged tracks in each of the two* $H^{\pm\pm}$ *candidate jets in (c), and the product of the reconstructed charges of the two* $H^{\pm\pm}$ *candidate jets in (d). The points with error bars indicate the OPAL data and the shaded regions indicate the background expectation. Note that "hadrons" includes both* $q\bar{q}(\gamma)$ *and hadronic events from all 4-fermion processes. Two example signal expectations for a 130 GeV doubly-charged Higgs boson are also shown normalised to a cross-section corresponding to* $h_{ee} = 0.1$ *scaled by a factor 20, assuming either a 100%* $H^{\pm\pm} \rightarrow ee$ *branching ratio (dashed line) or a 100%* $H^{\pm\pm} \rightarrow \tau\tau$ *branching ratio (dotted line). The cut requirements are indicated by the arrows.*

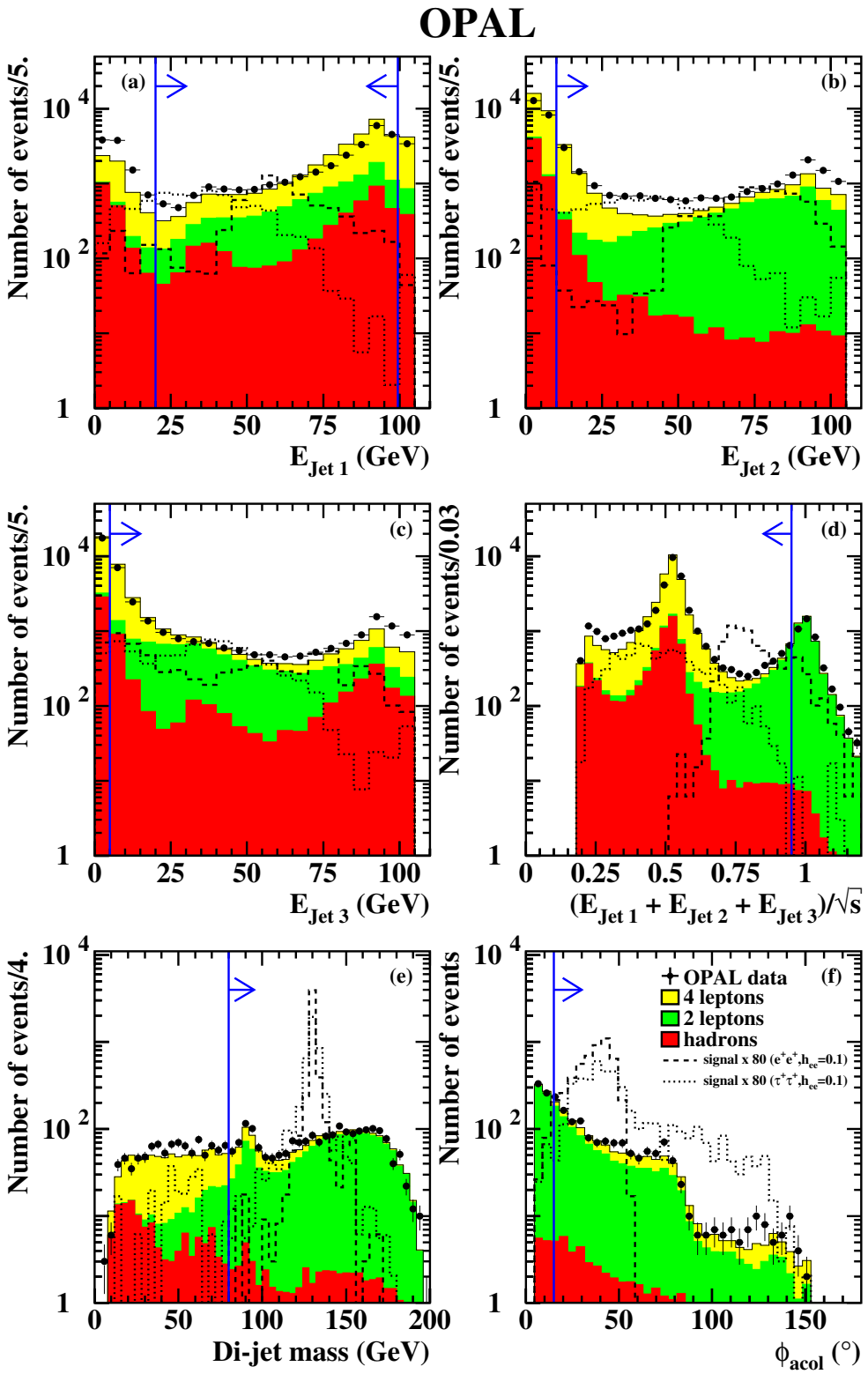

Figure 5.4: *Examples of some of the quantities used in the three-lepton selection shown immediately before the corresponding cut is applied (see Chapter 5). The energies of jet 1 (a), jet 2 (b) and jet 3 (c), sorted by their energies are shown. The sum of the jet energies is shown in (d). The reconstructed mass of the two* $H^{\pm\pm}$ *candidate jets is shown in (e) and finally the acollinearity angle* ϕ_{acol} *is shown in (f). The legend description is done in the caption of figure 5.5. The cut requirements are indicated by the arrows.*

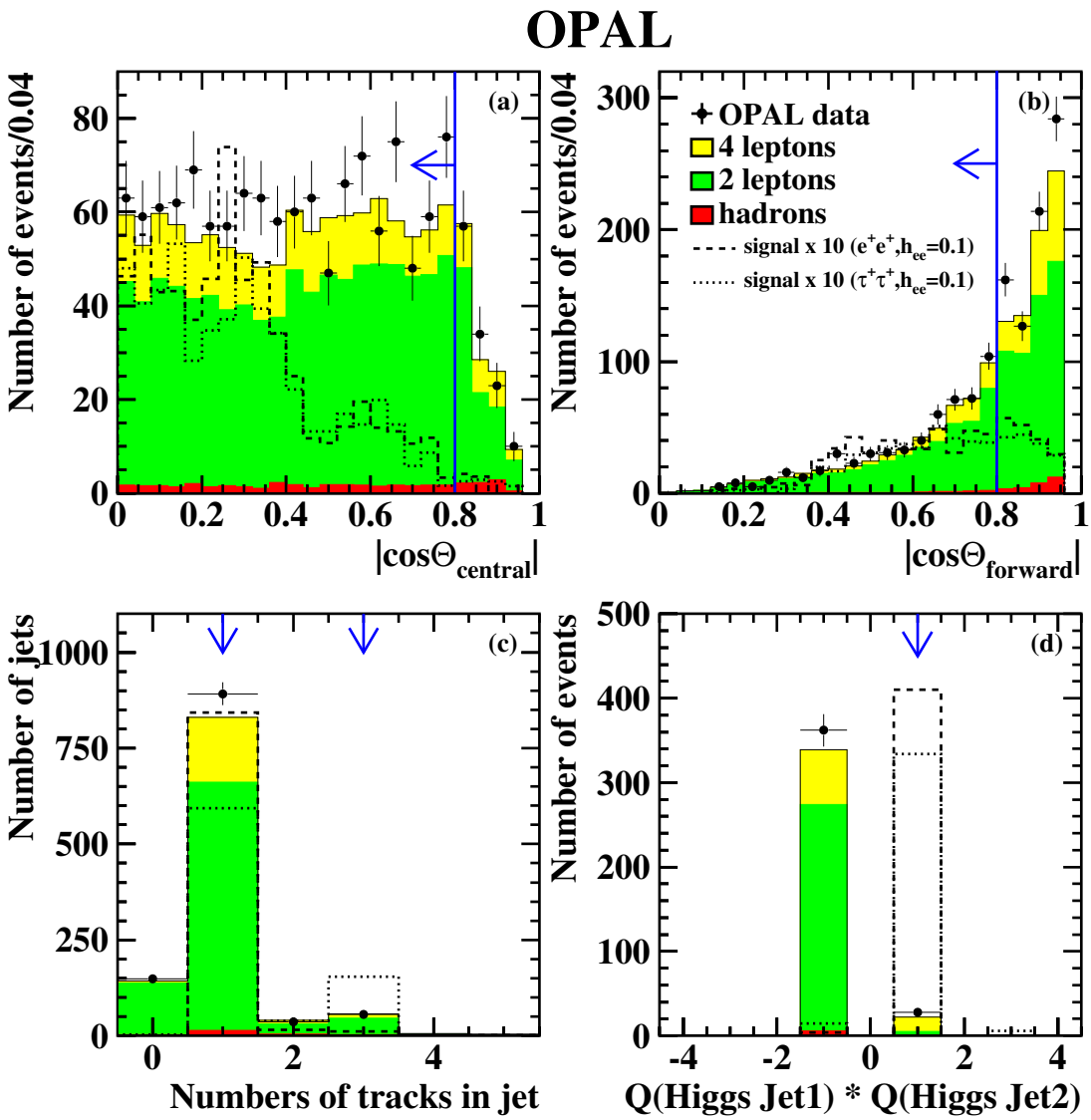

Figure 5.5: *Examples of some of the quantities used in the three-lepton selection shown immediately before the corresponding cut is applied (see Chapter 5). The absolute values of the cosines of the polar angle of the more central and the more forward Higgs boson candidate jets are shown in (a) and (b), the number of charged tracks in each of the two* $H^{\pm\pm}$ *candidate jets in (c), and the product of the reconstructed charges of the two* $H^{\pm\pm}$ *candidate jets in (d). The points with error bars indicate the OPAL data and the shaded regions indicate the background expectation. Note that "hadrons" includes both* $q\bar{q}(\gamma)$ *and hadronic events from all 4-fermion processes. Two example signal expectations for a 130 GeV doubly-charged Higgs boson are also shown normalised to a cross-section corresponding to* $h_{ee} = 0.1$ *scaled by a factor 10, assuming either a 100%* $H^{\pm\pm} \rightarrow ee$ *branching ratio (dashed line) or a 100%* $H^{\pm\pm} \rightarrow \tau\tau$ *branching ratio (dotted line). The cut requirements are indicated by the arrows.*

Two-lepton analysis

Cut	Data	Total Bkg.	$\ell^+\ell^-$	4-ℓ	'$\gamma\gamma$' ee$\ell\ell$	q$\bar{\text{q}}$	'$\gamma\gamma$' eeqq	Efficiency [%]					
								ee	$\mu\mu$	$\tau\tau$	eμ	eτ	$\mu\tau$
(2.1)	19612	17659.3	13776.9	1249.6	2249.7	173.3	209.9	45.7	45.9	41.5	43.1	42.5	43.2
(2.2)	15168	14731.3	11381.3	1118.7	1971.5	158.1	101.8	44.3	39.1	36.4	39.8	37.7	36.2
(2.3)	13455	13002.6	10855.6	988.1	1026.5	120.8	11.6	44.3	39.0	35.0	39.8	37.7	35.9
(2.4)	6681	6685.9	5025.5	774.0	777.5	100.1	8.7	41.0	36.3	32.6	36.9	34.9	33.2
(2.5)	1318	1353.4	890.6	325.9	124.3	12.5	0.1	23.8	24.3	20.3	22.9	20.4	21.1
(2.6)	1181	1216.2	792.6	299.5	121.4	2.7	0.0	23.0	23.9	17.9	22.3	19.2	20.2
(2.7)	27	22.1	10.4	2.7	8.5	0.5	0.0	22.9	23.8	17.5	22.3	19.0	20.0
		$\pm$1.7	$\pm$1.3	$\pm$0.2	$\pm$1.1	$\pm$0.1	$\pm$0.0	$\pm$1.9	$\pm$2.0	$\pm$2.0	$\pm$2.0	$\pm$2.0	$\pm$2.0
								(64.6)	(67.3)	(49.1)	(63.0)	(53.6)	(56.6)

Three-lepton analysis

Cut	Data	Total Bkg.	$\ell^+\ell^-$	4-ℓ	'$\gamma\gamma$' ee$\ell\ell$	q$\bar{\text{q}}$	'$\gamma\gamma$' eeqq	Efficiency [%]					
								ee	$\mu\mu$	$\tau\tau$	eμ	eτ	$\mu\tau$
(3.1)	40948	40899.7	7422.7	467.9	27011.1	260.1	5738.0	34.1	36.2	33.3	36.5	37.4	35.8
(3.2)	3203	2816.0	1685.9	153.3	778.9	63.1	134.8	22.7	24.0	21.1	23.8	25.0	23.8
(3.3)	2031	1912.0	1557.9	100.5	199.4	44.4	9.8	22.7	24.0	20.0	23.7	24.7	23.3
(3.4)	1359	1247.1	939.8	83.2	182.2	32.5	9.3	21.8	23.4	19.5	22.7	23.6	22.5
(3.5)	572	538.3	427.4	41.4	55.5	13.3	0.7	15.5	17.8	14.1	16.2	17.0	16.6
(3.6)	390	361.8	273.4	29.9	52.5	5.8	0.2	14.7	17.3	12.6	14.9	15.7	15.5
(3.7)	28	22.3	4.4	4.0	13.3	0.5	0.1	14.6	17.2	11.9	14.6	15.2	15.2
		$\pm$1.6	$\pm$0.7	$\pm$0.3	$\pm$1.4	$\pm$0.1	$\pm$0.0	$\pm$2.0	$\pm$2.0	$\pm$2.1	$\pm$2.0	$\pm$2.1	$\pm$2.1
								(41.0)	(48.8)	(33.4)	(41.4)	(42.9)	(42.8)

Sum

$\sum$	55	44.4	14.8	6.8	21.8	1.0	0.1	37.5	41.0	29.3	36.9	34.2	35.2
		$\pm$2.0	$\pm$1.3	$\pm$0.3	$\pm$1.5	$\pm$0.1	$\pm$0.0	$\pm$2.8	$\pm$2.8	$\pm$2.9	$\pm$2.8	$\pm$2.9	$\pm$2.9
								(105)	(116)	(82.5)	(104)	(96.5)	(99.4)

Table 5.2: *The number of remaining events in the data after each cut, and the number expected from Standard Model background sources. Also shown are the efficiencies of expected signal events for a 130 GeV doubly-charged Higgs boson assuming unmixed ee, $\mu\mu$, $\tau\tau$ and mixed eμ, eτ, $\mu\tau$ decays. The number of expected signal events for $h_{ee} = 0.1$ is shown in brackets assuming 100% branching ratio for the given decay mode. The errors due to Monte Carlo statistics are also listed for events surviving the full analysis.*

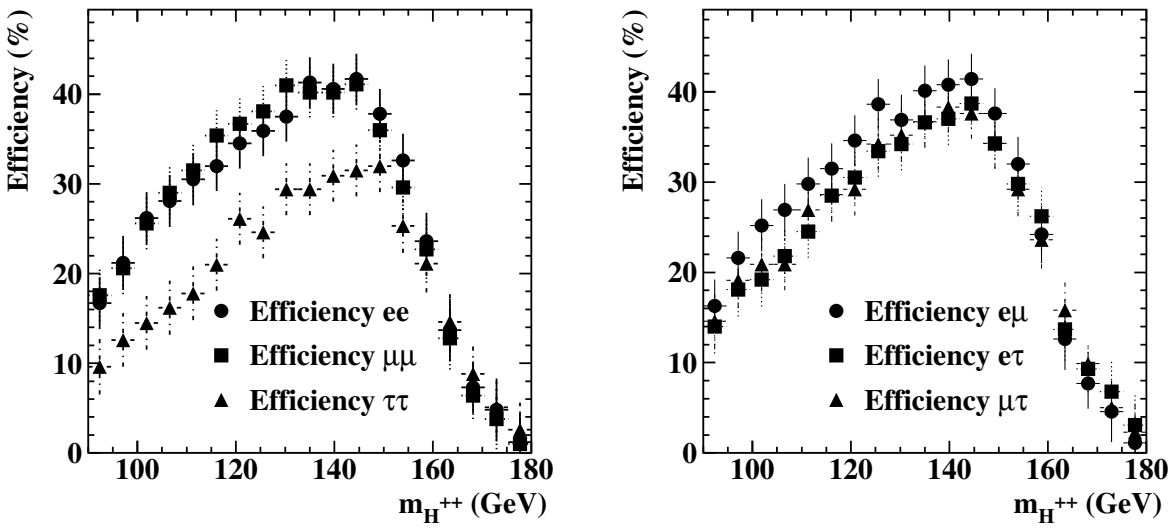

Figure 5.6: *Signal selection efficiencies for the unmixed channels ee, $\mu\mu$ and $\tau\tau$ on the left side and the same plot for the mixed channels eμ, eτ and $\mu\tau$ on the right side for hypothetical doubly-charged Higgs boson masses up to 180 GeV. It is obvious that a linear interpolation between the sample efficiencies is reasonable. It is also evident, that the $\tau\tau$ channel has the lowest selection efficiency.*

5.4 Systematic Uncertainties

In this section the effects on selection efficiencies and background predictions from uncertainties in the modeling of physics processes are discussed. Besides the description of the causes of the uncertainties, it is described how they are estimated. Different sources of uncertainties are examined separately.

5.4.1 Uncertainties due to the Modeling of Cut Variables

Monte Carlo modeling of the variables used in the selection cuts can induce systematic effects. The possible level of mismodeling is assessed by comparing data and background Monte Carlo for each variable after the preselection (cut (2.1) and (3.1), respectively), where the contribution from a signal would be negligible. Differences between the data and background Monte Carlo simulation are used to define a possible shift in each variable, and then the systematic uncertainties are evaluated by varying the cuts by these shifts. Both the final expected background and signal efficiencies are re-calculated with these shifted cuts, and the full differences of the nominal values are assigned as systematic uncertainties. This procedure is done for the $|cos\theta|$ cuts (2.5/3.5), for all cuts, which set requirements on the jet energy (2.2/3.2), for the acollinearity angle, ϕ_{acol}, cut (2.4/3.4) and also for the last cut (2.7/3.7), which require that the product of the jet charge of the two jets associated to the $H^{\pm\pm}$ is equal to +1.

This uncertainty of charge identification to reject a significant fraction of the background, is estimated from a clean sample of Bhabha events selected by changing the cuts as follows. The cuts (2.2)c and (3.2)d are not applied. Cuts (2.2)d and (3.2)e are changed

from $E_{\text{jet1}} + E_{\text{jet2}}(+E_{\text{jet3}}) < 0.95\sqrt{s}$ to $E_{\text{jet1}} + E_{\text{jet2}}(+E_{\text{jet3}}) > 0.95\sqrt{s}$. This sample consists mainly of Bhabha events and has no overlap with the search sample. The fraction of like-signed electron pairs is 2.0% in data and 1.7% in Monte Carlo. The systematic uncertainties on the background and signal efficiencies are evaluated by randomly changing the sign of the charge for 0.15% of the tracks, in order to increase the fraction of fake like-signed events by 0.3%, the observed difference between data and Monte Carlo in Bhabha sample. The full differences between the new background and efficiencies and the nominal ones are taken as systematic uncertainties. The chosen values are shown in table 5.3.

5.4.2 Uncertainties due to the Modeling of multi-peripheral "two-photon" Processes

The largest background in the selection originates from processes with four charged leptons in the final state, particularly from multi-peripheral "two-photon" processes. Of concern is the fact, that in our standard Monte Carlo background samples available at all centre-of-mass energies, the multi-peripheral diagrams are treated with specialised event generators, which neglect interference with non-multi-peripheral diagrams. Special samples of the full set of $e^+e^- \to e^+e^-\ell^+\ell^-$ diagrams, including interference, were prepared using grc4f2.2 [45] at $\sqrt{s} = 206$ GeV to study this effect. The background using the full set of $e^+e^-\ell^+\ell^-$ diagrams including interference is in both analyses about 25% lower than our standard set of Monte Carlo generators. While grc4f2.2 includes interference effects, it has other differences with respect to our standard background simulations and cannot be used as the primary sample. It is therefore, simply assigned a 25% systematic uncertainty on the $e^+e^-\ell^+\ell^-$ background according to this cross-check.

All systematic uncertainties are summarised in table 5.3. Additional systematic uncertainties, such as on the integrated luminosity, are negligible.

Quantity	Variation	2-lepton analysis:		3-lepton analysis:	
		Δ Bkg (%)	Δ Sig (%)	Δ Bkg (%)	Δ Sig (%)
Jet $\cos\theta$	±0.5°	8	1	7	1
Jet Energy	±1%	1	1	2	1
ϕ_{acol}	±0.5°	2	1	1	1
Charge Misidentification	0.15%	14	1	4	1
Background Modeling	(see text)	25	–	25	–
Monte Carlo Statistics	–	8	10	7	14
Quadratic Sum		31	10	27	14

Table 5.3: *Systematic uncertainties on signal and background.*

Chapter 6

Interpretation of Results

Although the selection shows that the number of observed and expected events agree well in all analysis channels, it is interesting to investigate the mass distributions to search for a peak, which could be assigned to the doubly-charged Higgs boson $H^{\pm\pm}$.

In the two-lepton analysis, which uses the events fulfilling the two-lepton selection, the invariant mass of the two jets is calculated using the measured jet energies and directions. It is not possible to use the "angle-based" kinematic reconstruction described in chapter 5 for the two-lepton analysis in contrast to the three-lepton analysis. The mass distributions are shown in figure 6.1 for events passing all cuts except the like-signed charge requirement (a), and also with all cuts applied (b). Signal sample for the unmixed flavour decays ee and $\tau\tau$ are also shown. No excess of events, which could imply the presence of a signal is observed in the data. In figure 6.2 the same distribution are shown, but with sample signals of the mixed lepton flavour decays eμ and $\mu\tau$.

In the three-lepton analysis, which uses the events fulfilling the three-lepton selection, we calculate the $H^{\pm\pm}$ candidate reconstructed masses, M_{rec}, shown in figure 6.1, using the "angle-based" kinematic reconstruction described in item (3.3) in chapter 5. The mass distributions are shown both for events passing all cuts except the like-signed charge requirement (c), and also with all cuts applied (d). Signal sample for the unmixed flavour decays ee and $\tau\tau$ are also shown. Additionally, as a cross-check to ensure that no di-jet mass peak is present after the event reconstruction is reduced by the angle-based method, the largest di-jet mass calculated from only the track and cluster information (see chapter 5) was examined. No excess of events, which could imply the presence of a signal, is observed in the data. In figure 6.2 the same distribution are shown but with sample signals of the mixed lepton flavour decays eμ and $\mu\tau$.

The result is, that no evidence for the existence of a doubly-charged Higgs boson $H^{\pm\pm}$ is observed. Therefore, it is just possible to reduce the theoretical phasespace by calculating exclusion limits for the Yukawa coupling h_{ee}, because this analysis is sensitive to this quantity.

In the following sections, the method to calculate exclusion limits is described and the calculated limits for the Yukawa coupling h_{ee} are presented.

6.1 Limit Calculation

In this section the basic ideas to get an exclusion limit at a desired confidence level (C.L.) are described. First the confidence level for a simple counting experiment is defined. The

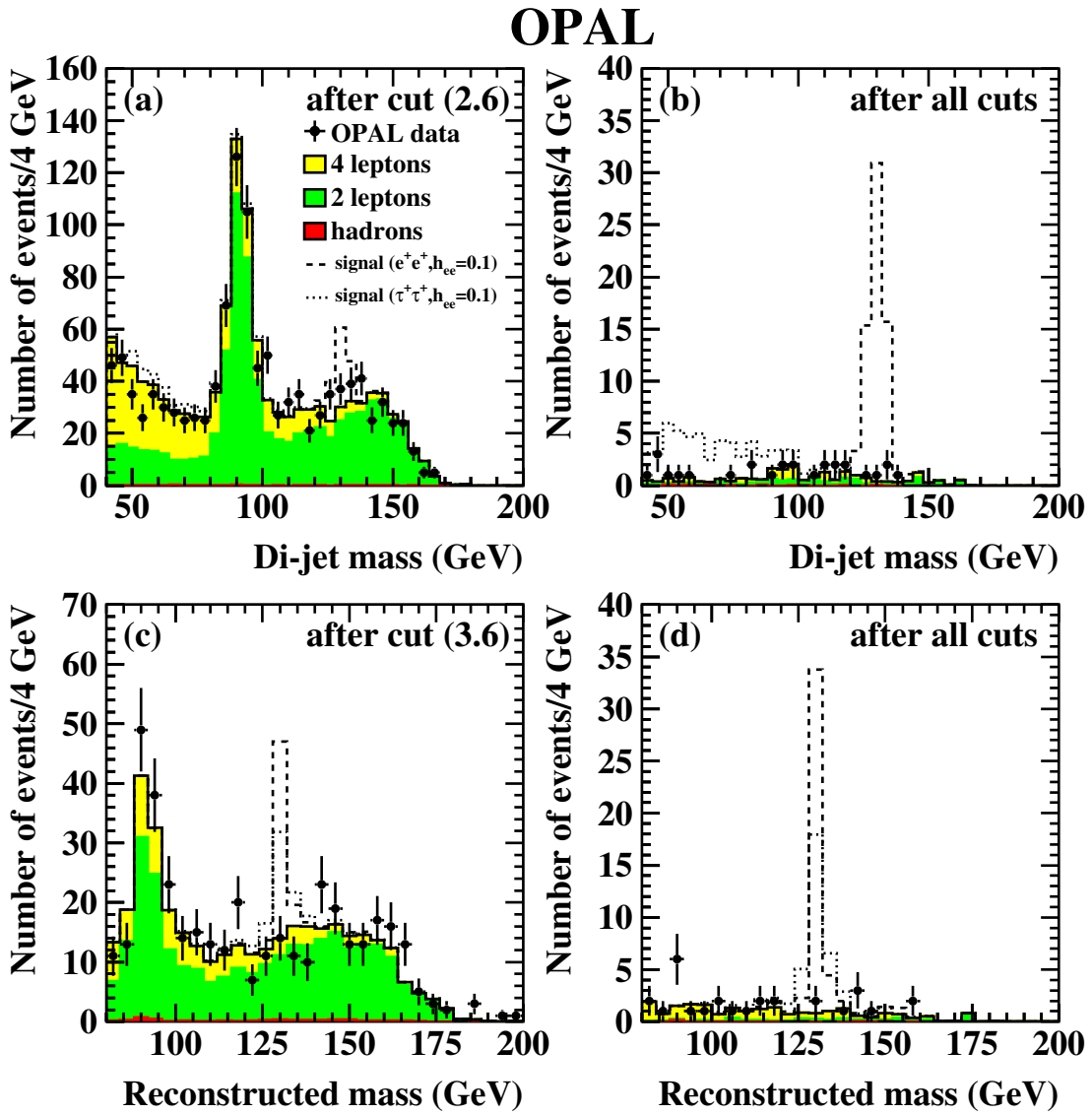

Figure 6.1: *The reconstructed* $H^{\pm\pm}$ *candidate mass distributions including unmixed lepton flavour signal samples of ee and* $\tau\tau$ *decays. The invariant di-jet mass is shown for the 2-lepton analysis both before and after the like-signed jet requirement (cut (2.7)) in (a) and (b), respectively. For the 3-lepton analysis, the reconstructed* $H^{\pm\pm}$ *mass using the jet angles as discussed in the text, is shown before and after cut (3.7) in (c) and (d), respectively. The points with error bars indicate the OPAL data and the shaded regions indicate the background expectation. Note that "hadrons" includes both* $q\bar{q}(\gamma)$ *and hadronic events from all 4-fermion processes. Two example signal expectations for a 130 GeV doubly-charged Higgs boson are also shown normalised to a cross-section corresponding to* $h_{ee} = 0.1$*, assuming either a 100%* $H^{\pm\pm} \rightarrow$ ee *branching ratio (dashed line) or a 100%* $H^{\pm\pm} \rightarrow \tau\tau$ *branching ratio (dotted line). Note that due to the undetected neutrinos from the tau-lepton decay there is no peak in the* $H^{\pm\pm} \rightarrow \tau\tau$ *signal sample of the 2-lepton analysis ((a) and (b)).*

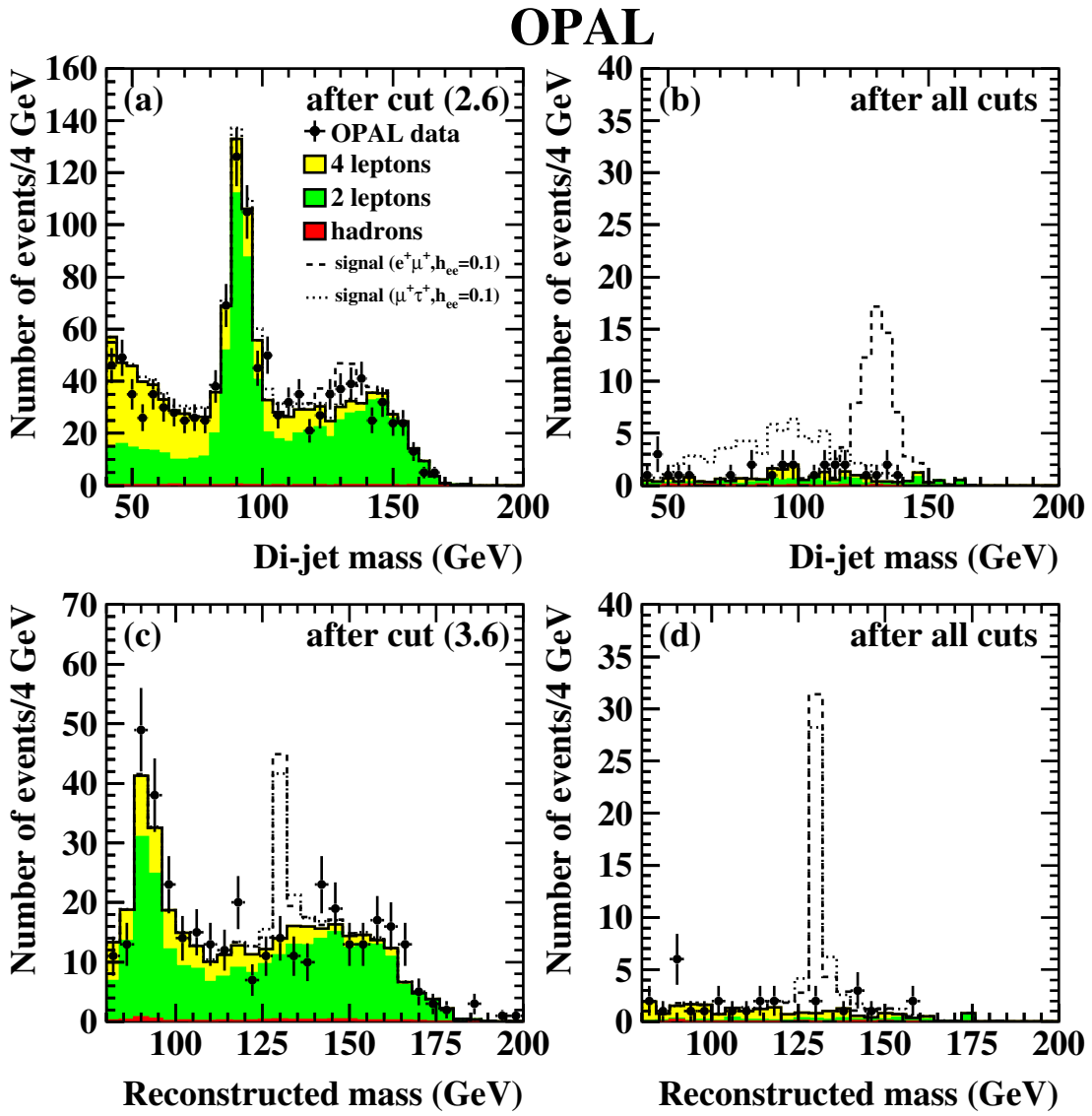

Figure 6.2: *The reconstructed* $H^{\pm\pm}$ *candidate mass distributions including mixed lepton flavour signal samples of* $e\mu$ *and* $\mu\tau$ *decays. The invariant di-jet mass is shown for the 2-lepton analysis both before and after the like-signed jet requirement (cut (2.7)) in (a) and (b), respectively. For the 3-lepton analysis, the reconstructed* $H^{\pm\pm}$ *mass using the jet angles as discussed in the text, is shown before and after cut (3.7) in (c) and (d), respectively. The points with error bars indicate the OPAL data and the shaded regions indicate the background expectation. Note that "hadrons" includes both* $q\bar{q}(\gamma)$ *and hadronic events from all 4-fermion processes. Two example signal expectations for a 130 GeV doubly-charged Higgs boson are also shown normalised to a cross-section corresponding to* $h_{ee} = 0.1$*, assuming either a 100%* $H^{\pm\pm} \to e\mu$ *branching ratio (dashed line) or a 100%* $H^{\pm\pm} \to \mu\tau$ *branching ratio (dotted line). Note that due to the undetected neutrinos from the tau-lepton decay the peak is much wider in the* $H^{\pm\pm} \to \mu\tau$ *signal sample of the 2-lepton analysis ((a) and (b)).*

advantage of introducing a test statistic when combining several counting experiments is clarified. Also the influence on the observed exclusion limit of systematic uncertainties on the background- and signal expectation are described in the last part of this section.

6.1.1 Limit Calculation for a counting experiment

The output of a simple counting experiment consists of three numbers:

- b: the predicted number of background events.
- $s+b$: the predicted number of events, which would be observed if a signal is present in addition to the expected background.
- d: the observed number of events.

The interpretation of these numbers has to distinguish between two hypotheses: the presence of a signal (the signal-plus-background hypothesis, $s+b$) or the background-only hypothesis. In this analysis the $s+b$ hypothesis is equal to the production of doubly-charged Higgs bosons and the SM background processes. The b hypothesis is equal only to the presence of SM background. If the background-only hypothesis is favoured, like in this analysis, the confidence level at which the signal hypothesis can be excluded is of interest. However, in our theoretical framework the existence of the signal depends on the Yukawa coupling h_{ee}, which is responsible for the production of $H^{\pm\pm}$ in e^+e^- collisions. Furthermore the value of h_{ee} is not restricted by theoretical reasons, therefore, it makes more sense to give a limit for h_{ee}.

Under the assumption of no signal present in the data, the outcomes n of many (N $\rightarrow \infty$) counting experiments are distributed according to the Poisson statistic with a mean expected number of observed events b:

$$P_{Poisson}(n,b) = \frac{e^{-b}b^n}{n!}. \tag{6.1}$$

For the other case, where a signal is present, n would be distributed according to a Poisson distribution with a mean expected number of observed events $s+b$:

$$P_{Poisson}(n,s+b) = \frac{e^{-(s+b)}(s+b)^n}{n!}. \tag{6.2}$$

For example there are two distribution shown in figure 6.3, where $b=3$ and $s+b=15$ are assumed.

The next step is to determine the confidence level at which the signal-plus-background ($s+b$) hypothesis can be excluded. For the following consideration it is assumed, that six events are measured in a certain counting experiment ($d^{obs}=6$). Two quantities, $\mathrm{C.L._b}$ and $\mathrm{C.L._{s+b}}$, are defined:

$$\mathrm{C.L._b} = \sum_{n=0}^{d^{obs}} P_{Poisson}(n,b), \tag{6.3}$$

$$\mathrm{C.L._{s+b}} = \sum_{n=0}^{d^{obs}} P_{Poisson}(n,s+b). \tag{6.4}$$

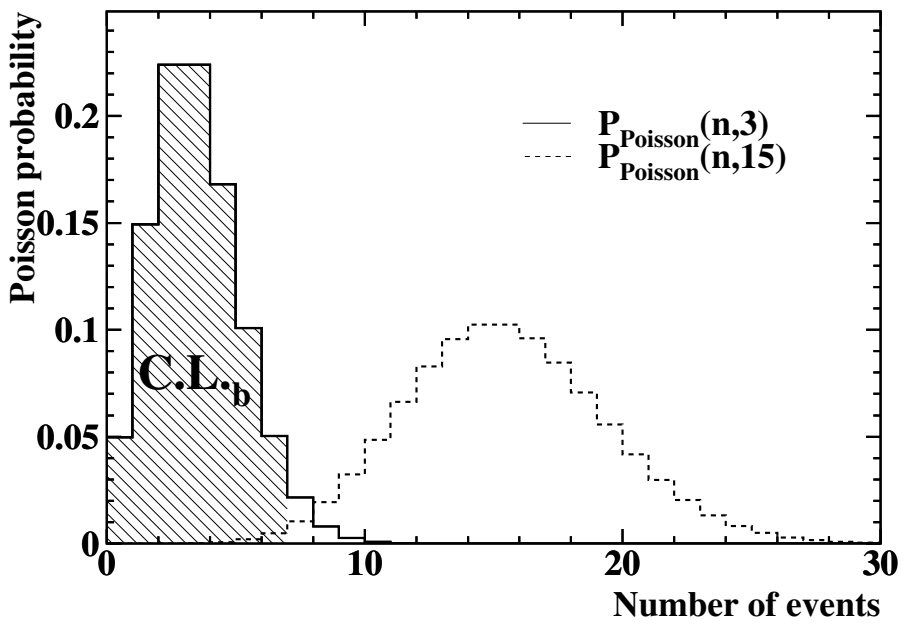

Figure 6.3: *The Poisson distributions for the expected number of observed events for the signal-plus background hypothesis ($P_{Poisson}$(n,15)) and the background-only hypothesis ($P_{Poisson}$(n,3)). The shaded area corresponds to* C.L.$_{\rm b}$.

C.L.$_{\rm b}$ is the fraction of experiments, which would result in the same or fewer events observed than d^{obs}, when the background-only hypothesis is true. In the same manner C.L.$_{\rm s+b}$ represents the fraction of experiments, which would result in the same or fewer observed events than d^{obs}, when the signal-plus-background hypothesis is true [55, 56].

$$\text{C.L.}_b = P_b(n \leq d^{obs}), \tag{6.5}$$

$$\text{C.L.}_{s+b} = P_{s+b}(n \leq d^{obs}). \tag{6.6}$$

To quantify the confidence at which a signal can be excluded, the number C.L.$_{\rm s}$ is defined:

$$\text{C.L.}_{\rm s} = \frac{\text{C.L.}_{\rm s+b}}{\text{C.L.}_{\rm b}}. \tag{6.7}$$

A signal is then said to be excluded with a confidence of 1 - C.L.$_{\rm s}$. If the mean expected number of events for the $s + b$ hypothesis depends on one or more parameters (such as cross-sections, branching ratios, etc.) usually the exclusion limit for these parameters is quoted at the 95 % C.L., i.e. the set of parameters is quoted for which 1 - C.L.$_{\rm s}$ = 95 %.

6.1.2 Combining Search Channels and Test Statistic

If it is required to calculate the C.L. for parameters in dependence of another parameter, it will be necessary to accomplish a separate counting experiment for each setting of this parameter. In this analysis the signal-plus-background hypothesis for doubly-charged

Higgs bosons at different masses can be distinguished by the position of the peak in the simulated signal mass distribution. To utilise this information a ±10 GeV "sliding mass window" around the hypothetical doubly-charged Higgs boson mass is used. Events within this window are counted in data and Monte Carlo simulation. The hypothetical Higgs boson mass is varied in 1 GeV steps. The width of the mass window is chosen such that it contains most of the expected signal events. A small efficiency correction, typically around 5% for ee, eμ and $\mu\mu$ and 10% for eτ, $\mu\tau$ and $\tau\tau$, due to this window is applied. In the two-lepton analysis for any channel containing τ leptons no mass window cut is applied, because in this channel it is not possible to reconstruct the correct mass of the doubly-charged Higgs boson due to the undetected neutrinos. The combination of the channels is accomplished with the help of a test statistic as suggested in [55].

A test statistic Q is a quantity, which discriminates signal-like outcomes from background-like ones. An optimal choice for the test statistic is the likelihood ratio defined as:

$$Q(n) = \frac{P_{Poisson}(n, s+b)}{P_{Poisson}(n, b)} = \frac{e^{-s}(s+b)^n}{b^n}, \tag{6.8}$$

where b and s are the best estimates for the expected number of background and signal events respectively. The test statistic is an observable of an experiment. Once b and s are determined by Monte Carlo techniques, Q depends only on the number of observed events n.

The benefit of introducing the likelihood ratio as a test statistic becomes clear when several search channels are combined. It has the property that the joint test statistic for the outcome of many channels is the product of the test statistics of each channel separately:

$$Q^{tot} = \prod_{i=1}^{N_{chan}} Q_i. \tag{6.9}$$

Here N_{chan} is the total number of channels and Q_i is defined according to 6.8

$$Q_i(n_i) = \frac{e^{-s_i}(s_i + b_i)_i^n}{b_i^{n_i}}. \tag{6.10}$$

When calculating the logarithm of equation 6.9 one obtains:

$$\ln\left(Q^{tot}\right) = -s_{tot} + \sum_{i=1}^{N_{chan}} n_i \ \ln\left(1 + \frac{s_i}{b_i}\right), \tag{6.11}$$

i.e. the observed number of events in each channel is weighted with the signal over background ratio in this channel. When interpreting each bin in the reconstructed mass distribution as an individual counting experiment the bins under the mass peak expected from a signal gain a higher weight compared to bins far from the region of interest. Hence the sensitivity of the combined test statistic is adjusted to the considered doubly-charged Higgs boson mass hypothesis.

6.1.3 Exclusion Limit

The expected exclusion limit states how many signal events can be expected to be excluded at the 95 % confidence level (C.L.) assuming that no signal is present in the data. The background and signal expectations are calculated in this analysis by a Monte Carlo approach. Each time the assumed number of "observed" events in each channel $n_i, i = 1, ...N_{chan}$ is taken from an ensemble of hypothetical outcomes $n_j, j = 1, ...N_{MC}$, where n_j are distributed according to a Poisson distribution with a mean expected number of b_i events ($P_{Poisson}(n_i, b_i)$). The median of the distribution Q_b is then assumed to be the test statistic corresponding to the number of events, which would be observed if no signal is present in the data. The observed exclusion limit states accordingly the same, but under the assumption that signal is present in the data (Q_{s+b}). C.L.$_s$ and C.L.$_{s+b}$ are calculated according to equations 6.5 and 6.6.

In the two search channels (2l- and 3l-analysis) considered in this analysis, the expected total number of signal events depends on the branching ratios and on the production cross-section, which is also dependent on the $H^{\pm\pm}$ Yukawa coupling h_{ee}. Therefore, limits are set on the $H^{\pm\pm}$ Yukawa coupling h_{ee}, assuming that the sum of the branching fractions of the $H^{\pm\pm}$ to all lepton flavour combinations is 100 %.

6.1.4 Influence of Systematic Uncertainties

The influence of uncertainties in the expected number of signal and background events is implemented in the calculation of the exclusion limits [55]. The reason is that the distributions of the test statistics under the assumptions of the background-only and signal-plus-background hypothesis are affected, because the mean expected number of events is not precisely known due to the systematic uncertainties. Therefore, the mean expected values are varied within the systematic errors assuming a Gaussian distribution. A description of the uncertainties was presented in section 5.4.

6.2 Exclusion Limits for the Yukawa Coupling h_{ee}

In the theoretical framework, which is assumed in this search, the existence of the signal depends on the Yukawa coupling h_{ee}, which is responsible for the production of $H^{\pm\pm}$ in e^+e^- collisions. Furthermore, the value of h_{ee} is not restricted by theoretical reasons, therefore, it is reasonable to calculate a limit for h_{ee}. The limits on h_{ee} are calculated using the efficiencies determined from the PYTHIA Monte Carlo samples and the production cross-sections are determined in a consistent manner using PYTHIA (see discussion in section 5.1). The efficiency for an arbitrary Higgs boson mass is determined by linear interpolation (see figure 5.6) between the simulated signal Monte Carlo samples. The number of observed events, together with the number of expected signal and background events from both the two-lepton and three-lepton analyses are combined. No systematic uncertainty is assigned for theoretical uncertainties.

The 95 % confidence level limits on h_{ee} from combining both analyses are shown in figure 6.4(a)–(c) assuming a branching fraction of the doubly-charged Higgs boson into ee, $\mu\mu$, $\tau\tau$ of 100 %, respectively. In figure 6.5(a)–(c) the same is shown, but for the mixed flavour decays of the doubly-charged Higgs boson into eμ, eτ, and $\mu\tau$. Strictly, due to the production mechanism involving non-zero h_{ee}, exactly 100 % eμ, eτ, $\mu\mu$, $\mu\tau$ or

$\tau\tau$ decays are not possible, therefore, the latter limits should be considered for the case $h_{e\mu,e\tau,\mu\mu,\mu\tau,\tau\tau} \gg h_{ee}$. In all plots the observed and the expected limits are shown. The expected limits assuming only Standard Model processes (background hypothesis) are shown by the dotted lines, while the observed limits inferred from the data are shown by the solid lines. In figure 6.4(d), for each mass the highest limit from all possible unmixed lepton flavour combinations and in figure 6.5(d) the same for all possible mixed lepton flavour combinations is shown. The comparison shows that the unmixed limit is higher then the highest mixed one. Therefore, the highest unmixed limit is given as the overall limit on the Yukawa coupling h_{ee}. So an upper limit on $h_{ee} < 0.071$ is inferred for $M(H^{\pm\pm}) < 160$ GeV at the 95 % confidence level, which is valid for all possible lepton flavour combinations in the decays. The limit is determined by the pure $\tau\tau$ case except for masses in excess of 170 GeV. For the case of pure ee decays the limit is $h_{ee} < 0.042$, and for $\mu\mu$ decays $h_{ee} < 0.049$, both for $M(H^{\pm\pm}) < 160$ GeV. For the mixed flavour decay modes eμ, eτ, and $\mu\tau$ the limits are located between those for the unmixed flavour decays. For the case of eμ decays the limit is $h_{ee} < 0.047$, for eτ decays $h_{ee} < 0.059$, and for $\mu\tau$ decays $h_{ee} < 0.063$ all for $M(H^{\pm\pm}) < 160$ GeV.

Figure 6.6 shows the limit on the Yukawa coupling h_{ee} assuming a 100% branching fraction of the $H^{\pm\pm} \to ee$, which is calculated with this direct search and also the indirect limit on h_{ee} obtained from Bhabha scattering described in [33]. For low masses up to 160 GeV the limit of this direct search is about a factor of 5 more sensitive.

In figure 6.7 [57] all known limits at 95% confidence level on the Yukawa coupling h_{ee} are shown. In the single production searches a 100% branching fraction of $H^{\pm\pm} \to ee$ is assumed. The predicted limit using HERA II data is indicated, additionally. In comparison to the other limits, it can be stated, that the limits from this search are the most strict ones in its accessible mass range. The analysis has been submitted for publication [33].

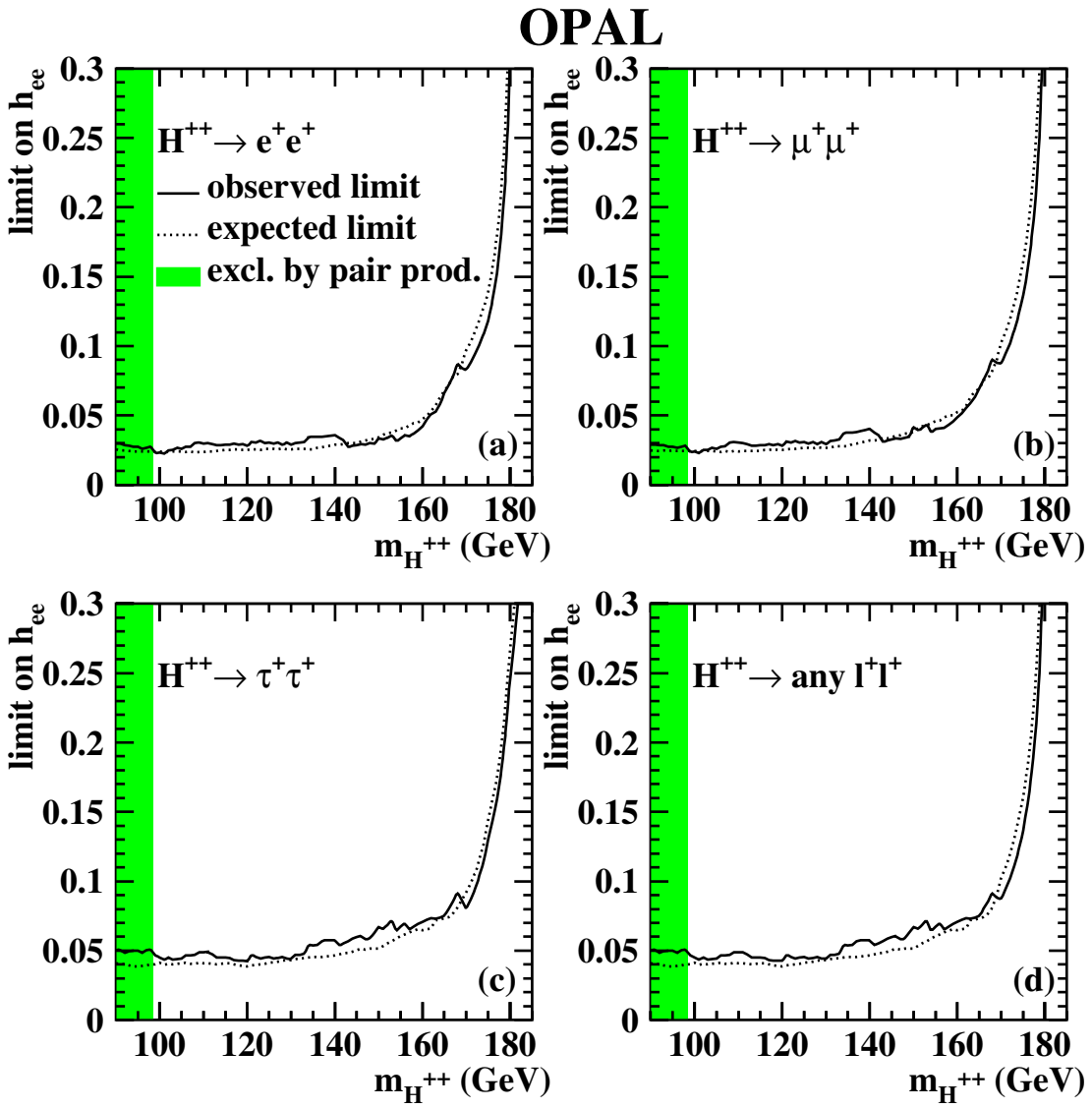

Figure 6.4: *Limits at the 95% confidence level on the Yukawa coupling* h_{ee} *assuming a 100% branching fraction of the* $H^{\pm\pm}$ *to (a) ee, (b)* $\mu\mu$ *and (c)* $\tau\tau$*. The limits are calculated with the combined results of the two-lepton and three-lepton analysis. In (b) and (c), the limits should be regarded as valid in the large branching fraction limit, since non-zero* h_{ee} *implies a non-zero electron branching fraction (see text). Since the ee and* $\mu\mu$ *efficiencies and mass resolutions are very similar, figures (a) and (b) are almost identical. The median expected limits assuming only Standard Model processes are shown by the dotted lines, while the actual limits inferred from the data are shown by the solid lines. In figure (d) the limit for arbitrary lepton flavour combinations (ee,* $e\mu$*,* $e\tau$*,* $\mu\mu$*,* $\mu\tau$ *and* $\tau\tau$*) is shown. It is determined by the pure* $\tau\tau$ *case except for masses in excess of 170 GeV. The shaded regions for masses below 98.5 GeV are excluded in Left-Right symmetric models by the OPAL pair production search [24].*

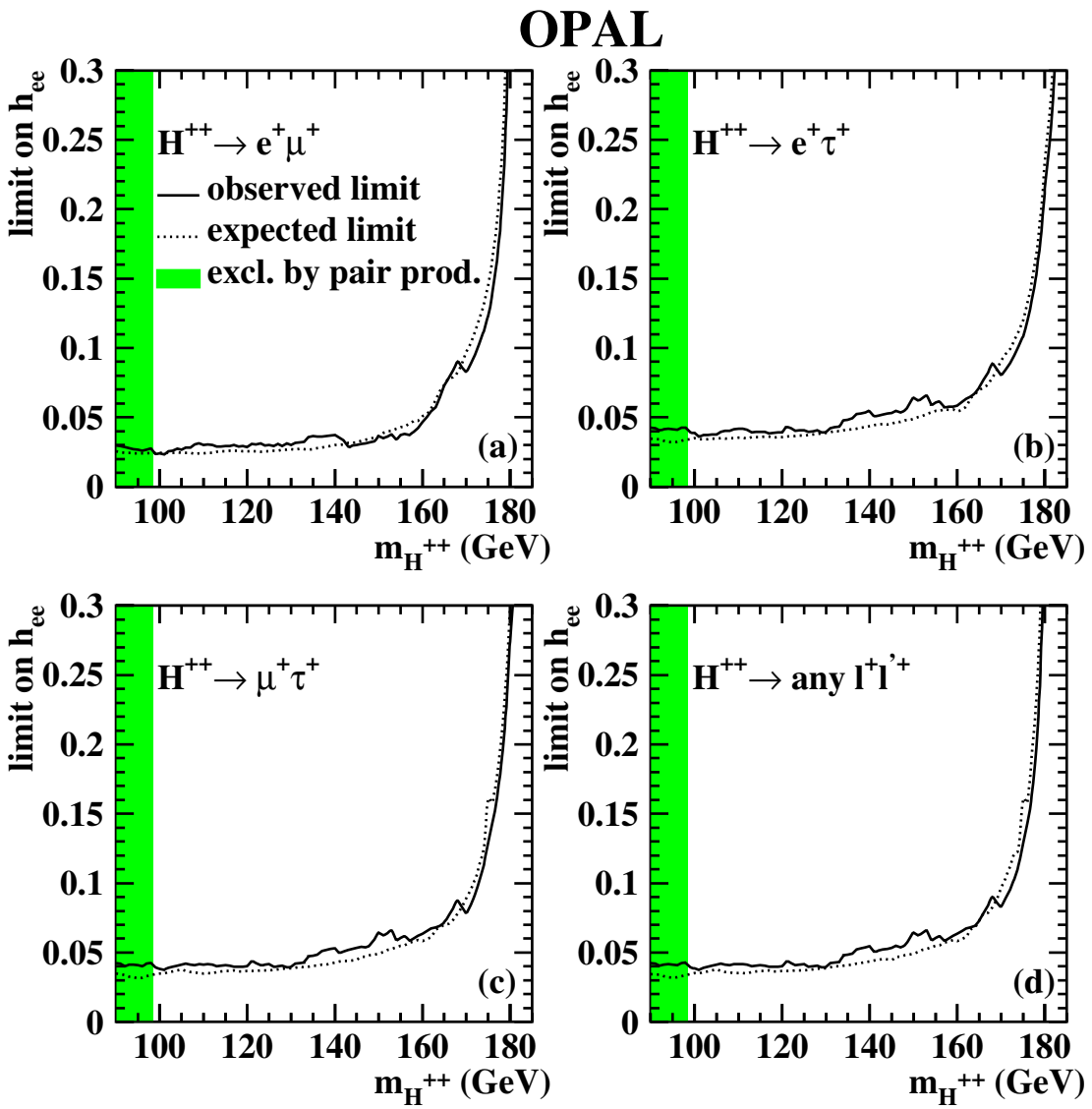

Figure 6.5: *Limits at the 95% confidence level on the Yukawa coupling* h_{ee} *assuming a 100% branching fraction of the* $H^{\pm\pm}$ *to (a)* $e\mu$*, (b)* $e\mu$ *and (c)* $\mu\tau$*. The limits are calculated with the combined results of the two-lepton and three-lepton analysis. In (b) and (c), the limits should be regarded as valid in the large branching fraction limit, since non-zero* h_{ee} *implies a non-zero electron branching fraction (see text). The median expected limits assuming only Standard Model processes are shown by the dotted lines, while the actual limits inferred from the data are shown by the solid lines. In figure (d) the limit for arbitrary mixed lepton flavour combinations (*$e\mu$*,* $e\tau$*, and* $\mu\tau$*) is shown. It is determined by the* $\mu\tau$ *case except for masses in excess of 170 GeV. The shaded regions for masses below 98.5 GeV are excluded in Left-Right symmetric models by the OPAL pair production search [24].*

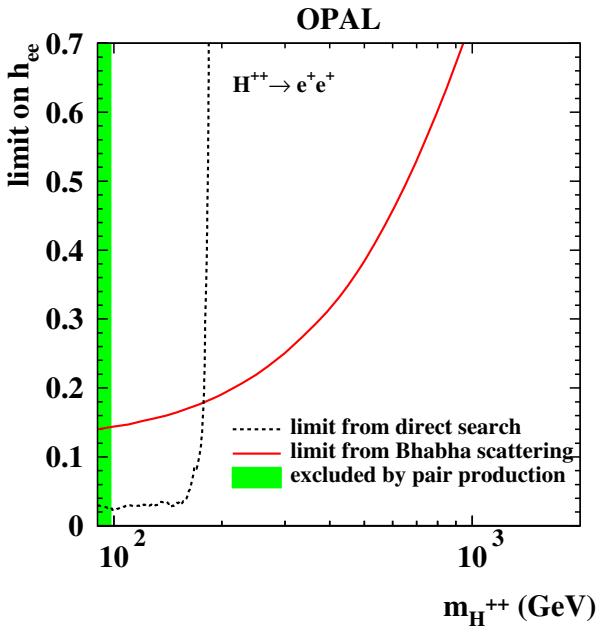

Figure 6.6: *Limits at the 95% confidence level on the Yukawa coupling* h_{ee} *assuming a 100% branching fraction of the* $H^{\pm\pm} \rightarrow ee$*. The direct limit is calculated with the combined results of the two-lepton and three-lepton analyses. The indirect limit on* h_{ee} *obtained from Bhabha scattering described in [33] is also shown. The shaded regions for masses below 98.5 GeV are excluded in Left-Right Symmetric models by the OPAL pair production search [24].*

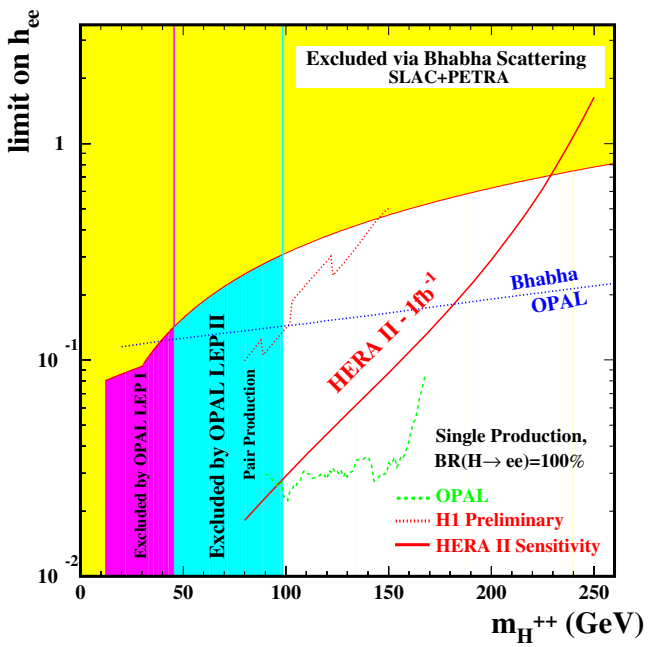

Figure 6.7: *All known limits at the 95% confidence level on the Yukawa coupling* h_{ee} *assuming in the single production searches a 100% branching fraction of the* $H^{\pm\pm} \rightarrow ee$ *[57].*

Chapter 7

Summary

The discovery of a doubly-charged Higgs boson $H^{\pm\pm}$ would be a definite signal of physics beyond the Standard Model. Doubly-charged Higgs bosons arise in many extensions of the SM. Two examples, the Left-handed Higgs Triplet model and the Left-Right Symmetric model, were presented. The characteristics of the doubly-charged Higgs boson including its production in e^+e^- collisions and possible decays are described. This analysis uses the decay into lepton pairs, in which all flavour combinations are possible. A direct search for the single production of doubly-charged Higgs bosons has been performed using 600.7 pb^{-1} of e^+e^- collision data collected by the OPAL experiment at centre-of-mass energies between 189 GeV and 209 GeV. No evidence for the existence of $H^{\pm\pm}$ is observed. Upper limits are determined on the Higgs Yukawa coupling to like-signed electron pairs, h_{ee}. A 95% confidence level upper limit of $h_{ee} < 0.071$ is inferred for $M(H^{\pm\pm}) < 160$ GeV assuming that the sum of the branching fractions of the $H^{\pm\pm}$ to all lepton flavour combinations is 100%.

To extend the accessible mass range of the doubly-charged Higgs boson, it is necessary to have experiments with larger centre-of-mass energy. The next experiment, which will provide physics with new data, will be the LHC (Large Hadron Collider) [58] at CERN in the year 2007. It is planned to reach energies of about 14 TeV. The production of doubly-charged Higgs boson in proton-proton collisions at LHC energies is investigated in [30]. At best $H^{\pm\pm}$ mass up to 2.4 TeV are achievable within one year run. At LHC also the main experimental signal of produced $H^{\pm\pm}$ would be a like-signed lepton pair.

Another planned experiment is a high energy e^+e^- linear collider like TESLA [59]. The discovery potential for doubly-charged Higgs bosons $H^{\pm\pm}$ is investigated in [28]. In this case the kinematic limit is $\approx \sqrt{s}$ for a single production search. The proposed centre-of-mass energy lies between 500 GeV and 1500 GeV. For $\sqrt{s} > M(H^{\pm\pm})$ doubly-charged Higgs boson could be discovered for even relatively small values of the Yukawa couplings, $h_{ee} > 0.01$. For values of $M(H^{\pm\pm})$ greater than $\sqrt{s}$, discovery is still possible, because of the distinctive, background free final state, which can be proceed via virtual contributions from intermediate $H^{\pm\pm}$. Therefore, even an e^+e^- linear collider with modest energy has the potential to extend $H^{\pm\pm}$ search limits significantly higher than can be achieved at the LHC.

Appendix A

Angular and Energy Distribution Comparison between PYTHIA and COMPHEP

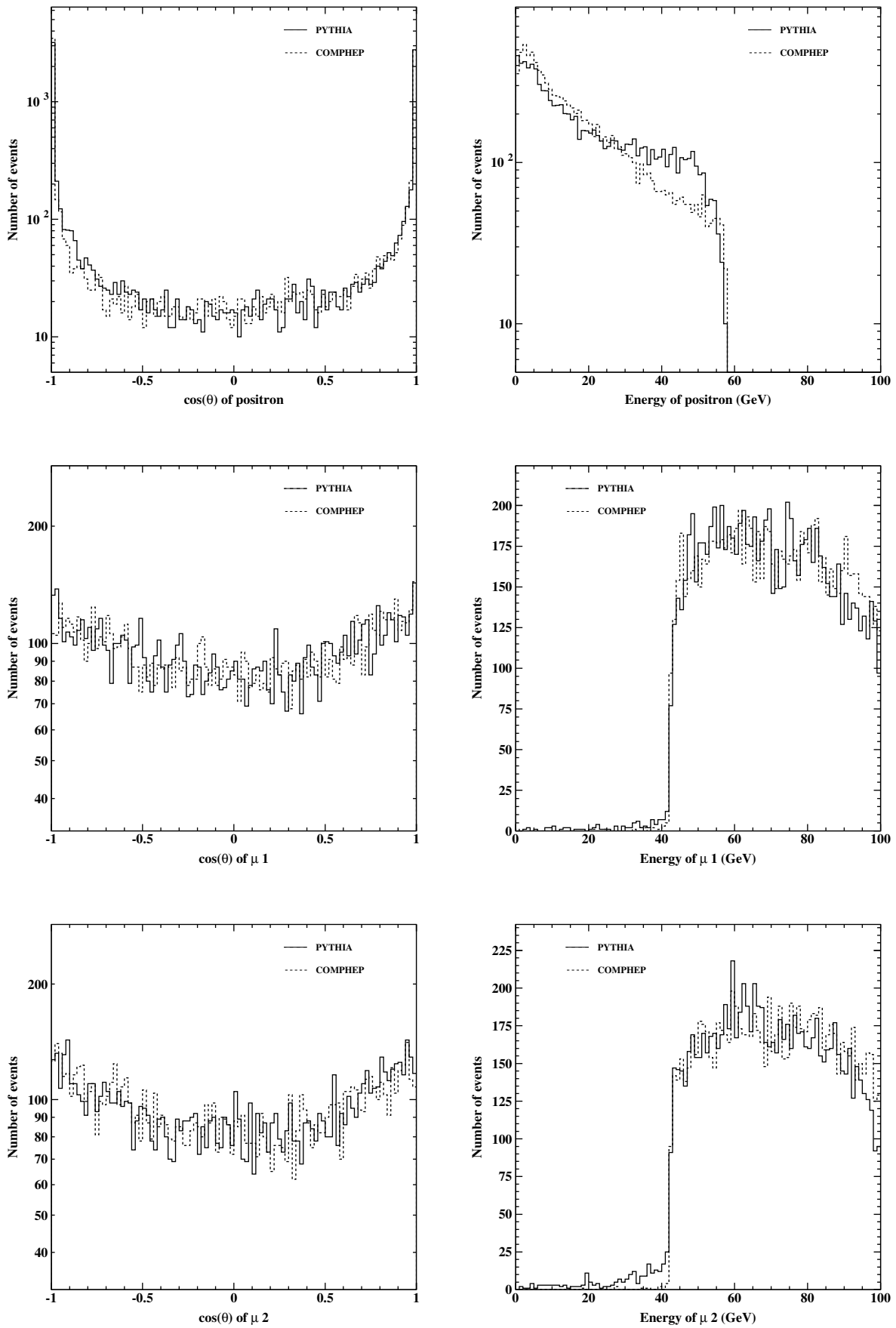

Figure A.1: *Angular and energy distribution of the final state particles.*

Appendix B

PYTHIA Comparison between Reconstruction with and without FSR

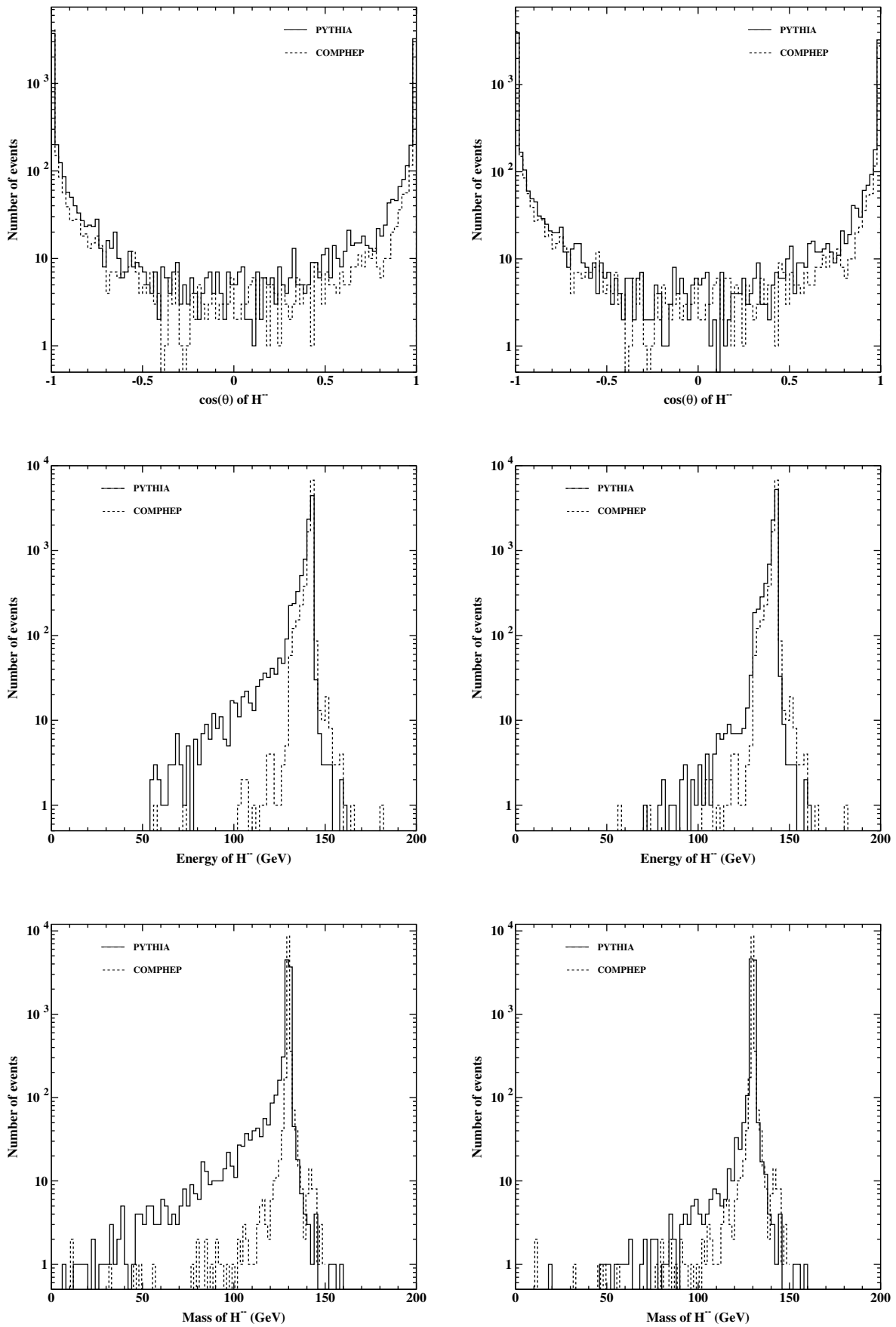

Figure B.1: *Angular, energy and mass distribution of the H^{--} without and with FSR contribution.*

Bibliography

[1] S. L. Glashow, Nucl. Phys. **22** (1961) 579;
S. Weinberg, Phys. Rev. Lett. **19** (1967) 1264;
A. Salam, *Elementary Particle Theory*, ed. N. Svartholm (Almquist and Wikselss, Stockholm, 1968), 367.

[2] G.B. Gelmini and M. Roncadelli, Phys. Lett. **B99** (1981) 411.

[3] J.C. Pati and A. Salam, Phys. Rev. **D10** (1974) 275;
R.N. Mohapatra and J.C. Pati, Phys. Rev. **D11** (1975) 566, 2558;
G. Senjanovic and R.N. Mohapatra, Phys. Rev. **D12** (1975) 1502;
R.N. Mohapatra and R.E. Marshak, Phys. Lett. **B91** (1980) 222;
R.N. Mohapatra and D. Sidhu, Phys. Rev. Lett. **38** (1977) 667.

[4] C. S. Aulakh, A. Melfo and G. Senjanovic, Phys. Rev. **D57** (1998) 4174;
Z. Chacko and R. N. Mohapatra, Phys. Rev. **D58** (1998) 15003;
B. Dutta and R. N. Mohapatra, Phys. Rev. **D59** (1999) 15018.

[5] G. L. Fogli, E. Lisi, A. Marrone, D. Montanino and A. Palazzo, Phys. Rev. D **66** (2002) 053010.

[6] H1 Collab., *"Search for Doubly-Charged Higgs Production at HERA"*, EPS03, Aachen (2003).

[7] E. Majorana, Nuovo Cim. **14** (1937) 171.

[8] K. Hagiwara et al, Phys. Rev. D 66, 010001 (2002).

[9] H. Georgi and M. Machacek, Nucl. Phys. B **262** (1985) 463.

[10] S. Chanowitz and M. Golden, Phys. Lett. B **165** (1985) 105.

[11] R. Godbole, B. Mukhopadhyaya and M. Nowakowski, Phys. Lett. B **352** (1995) 388.

[12] D. K. Ghosh, R. M. Godbole and B. Mukhopadhyaya, Phys. Rev. D **55** (1997) 3150.

[13] R. N. Mohapatra and G. Senjanovic, Phys. Rev. Lett. **44** (1980) 912.

[14] N. G. Deshpande, J. F. Gunion, B. Kayser and F. I. Olness, Phys. Rev. D **44** (1991) 837.

[15] J. F. Gunion, J. Grifols, A. Mendez, B. Kayser and F. I. Olness, Phys. Rev. D **40** (1989) 1546.

[16] M. Gell-Mann, P. Ramond and R. Slansky, in *Supergravity, eds. P. van Niewenhuizen and D. Z. Freedman (North Holland 1979); T. Yanagida, in Proceedings of Workshop on Unified Theory and Baryon Number in the Universe,* eds. O. Sawada and A. Sugamoto (KEK 1979).

[17] D0 Collab., S. Abachi *et al.*, FERMILAB-CONF-95-210-E.

[18] CDF Collab., F. Abe *et al.*, Phys. Rev. Lett. **68** (1992) 1463.

[19] T. G. Rizzo, Phys. Rev. D **50** (1994) 325.

[20] G. Barenboim, K. Huitu, J. Maalampi and M. Raidal, Phys. Lett. **B394** (1997) 132.

[21] J. F. Gunion, Int. J. Mod. Phys. A **11** (1996) 1551.

[22] E. Accomando and S. Petrarca, Phys. Lett. B **323** (1994) 212.

[23] S. Godfrey, P. Kalyniak and N. Romanenko, Phys. Lett. **B545** (2002) 361.

[24] OPAL Collab., G. Abbiendi *et al.* Phys. Lett. **B526** (2002) 221.

[25] T. G. Rizzo, Phys. Rev. D **25** (1982) 1355, Addendum-ibid. D **27** (1983) 657;
M. Lusignoli and S. Petrarca, Phys. Lett. B **226** (1989) 397.

[26] T. G. Rizzo, Phys. Rev. D **45** (1992) 42;
N. Lepore, B. Thorndyke, H. Nadeau and D. London, Phys. Rev. D **50** (1994) 2031.

[27] C. F. von Weizsäcker, Phys.Z· 88 (1934) 612;
E. J. Williams, Phys. Rev. 45 (1934) 729.

[28] S. Godfrey, P. Kalyniak and N. Romanenko, Phys. Rev. D **65** (2002) 033009

[29] E. Fermi, Nuovo Cim. (1925) 2,143.

[30] K. Huitu, J. Maalampi, A. Pietila and M. Raidal, Nucl. Phys. B **487** (1997) 27.

[31] M.L. Swartz, Phys. Rev. **D40** (1989) 1521.

[32] DELPHI Collab., J. Abdallah *et al.*, Phys. Lett. B **552** (2003) 127

[33] OPAL Collab., G. Abbiendi *et al.*, *"Search for the Single Production of Doubly-Charged Higgs Bosons and Constraints on their Couplings from Bhabha Scattering"*, paper submitted to Phys. Lett. B.

[34] OPAL Collab., K. Ahmet *et al.*, Nucl. Instr. Meth. **A305** (1991) 275;
S. Anderson *et al.*, Nucl. Instr. Meth. **A403** (1998) 326;
B.E. Anderson *et al.*, IEEE Trans. on Nucl. Science **41** (1994) 845;
G. Aguillion *et al.*, Nucl. Instr. Meth. **A417** (1998) 266.

[35] C. Hawkes, D. Lellouch, M. Redmond, O. Schaile and M. Schröder, *ROPE Users' Guide,* OPAL-Offline Note 16/OFFL-0487.

[36] T. Sjöstrand, Comp. Phys. Comm. **39** (1986) 347;
T. Sjöstrand, PYTHIA 5.7 and JETSET 7.4 Manual, CERN-TH 7112/93;
T. Sjöstrand *et al.*, Computer Phys. Commun. **135** (2001) 238.

[37] A. Pukhov *et al.*, arXiv:hep-ph/9908288.

[38] R. Nisius, Phys. Rept. **332** (2000) 165.

[39] R. Engel and J. Ranft, Phys. Rev. D **54** (1996) 4244.

[40] G. Marchesini *et al.*, Comp. Phys. Comm. **67** (1992) 465.

[41] J.A.M. Vermaseren, Nucl. Phys. **B229** (1983) 347.

[42] F.A. Berends, P.H. Daverveldt and R. Kleiss, Nucl. Phys. **B253** (1985) 421; Comp. Phys. Comm. **40** (1986) 271, 285, 309.

[43] F.A. Berends and R. Kleiss, Nucl.Phys. **B186** (1981) 22.

[44] M. Skrzypek *et al.*, Comp. Phys. Comm. **94** (1996) 216;
M. Skrzypek *et al.*, Phys. Lett. **B372** (1996) 286.

[45] J. Fujimoto *et al.*, Comp. Phys. Comm. **100** (1997) 128.

[46] S. Jadach, B.F.L. Ward and Z. Was, Phys. Lett. **B449** (1999) 97.

[47] G. Montagna, M. Moretti, O. Nicrosini and F. Piccinini, Nucl. Phys. **B541** (1999) 31.

[48] S. Jadach, W. Płaczek and B.F.L. Ward, Phys. Lett. **B390** (1997) 298.

[49] D. Karlen, Nucl. Phys. **B289** (1987) 23.

[50] J. Allison *et al.*, Nucl. Instr. Meth. **A317** (1992) 47.

[51] R. Brun, R. Hagelberg, M. Hansroul and J. C. Lassalle, CERN-DD-78-2-REV.

[52] OPAL Collab., G. Alexander *et al.* Z.Phys. **C52** (1991) 175.

[53] OPAL Collab., K. Ackerstaff *et al.*, Eur. Phys. J. **C2** (1998) 213.

[54] OPAL Collab., R. Akers *et al.* Z.Phys.**C63** (1994) 197.

[55] T. Junk, Nucl.Instrum.Meth. **A434** (1999) 435.

[56] N. Gollub, DESY-THESIS-2001-063 (2003).

[57] E. Perez, B. Olivier, *"Searches for new phenomena at current colliders: status and prospects"*, Lepton-Photon 03, Fermilab (2003).

[58] LHC Study Group Collab., CERN-AC-95-05-LHC.

[59] F. Richard, J. R. Schneider, D. Trines and A. Wagner, arXiv:hep-ph/0106314;
ECFA/DESY LC Physics Working Group Collab., J. A. Aguilar-Saavedra *et al.* arXiv:hep-ph/0106315.

Danksagung

Diese Stelle möchte ich nutzen, um allen Menschen, die mich während dieser Arbeit direkt und indirekt unterstützt haben, zu danken.

Mein besonderer Dank gilt Prof. Rolf-Dieter Heuer, für die Möglichkeit, in seiner Forschungsgruppe arbeiten zu dürfen. Die Aufenthalte am CERN und in Aachen waren sehr motivierend und wurden erst durch ihn ermöglicht. Außerdem möchte ich Prof. Beate Naroska für die Zweitkorrektur danken.

Dr. Klaus Desch hat einen großen Anteil an der Fertigstellung dieser Arbeit. Ohne seine Erklärungen und Unterstützung wäre das Gelingen nicht möglich gewesen.

Für die hilfreichen Diskussionen und Erklärungen innerhalb der gesamten Gruppe bin ich sehr dankbar. Mein besonderer Dank gilt in diesem Zusammenhang Niels Meyer, der mir immer mit Rat und Tat zur Seite stand. Außerdem möchte ich Markus Hamann, Carsten Hensel und Wolfgang Menges danken, die mich neben der Arbeit auch privat integriert und ertragen haben.

Ein wichtiger Teil meines Lebens besteht aus meiner Familie und meinen Freunden. Ich möchte mich bei meinen Freunden, für ihr beständiges Erfragen des Status dieser Arbeit, obwohl meine Antworten nicht immer freundlich waren, bedanken. Besonders engagierte Fragesteller waren: Imina, Julian, Meik, Michael und Ulrich. Ohne die ständige Unterstützung meiner Familie, im besonderen der Hilfe meiner Eltern und meines Bruders, wäre mein gesamtes Studium nicht möglich gewesen. Meine Eltern haben immer an mich geglaubt und ich konnte und kann immer auf sie zählen. Ihnen gilt mein größter Dank.

"Achtung! Jetzt gibt es nur zwei Möglichkeiten:
Entweder es funktioniert oder es funktioniert nicht."

Lukas in "Jim Knopf und Lukas, der Lokomotivführer"

Hiermit versichere ich, diese Arbeit selbstständig unter Verwendung der angegebenen Quellen und Hilfsmittel angefertigt zu haben.

Hamburg, den 11. September 2003

(Marius Groll)